ELSEVIER

Contents lists available at ScienceDirect

Progress in Energy and Combustion Science

journal homepage: www.elsevier.com/locate/pecs



The current status of high temperature electrochemistry-based CO₂ transport membranes and reactors for direct CO₂ capture and conversion



Peng Zhang^a, Jingjing Tong^b, Kevin Huang^{c,*}, Xuefeng Zhu^{a,d,*}, Weishen Yang^a

- ^a State Key Laboratory of Catalysis, Dalian Institute of Chemical Physics, Chinese Academy of Sciences, 457 Zhongshan Road, Dalian 116023, China
- ^b College of Transportation Engineering, Dalian Maritime University, 1 Linghai Road, Dalian 116026, China
- ^c Department of Mechanical Engineering, University of South Carolina, 541 Main Street, Columbia, South Carolina 29201, United States
- ^d Dalian National Laboratory for Clean Energy, Chinese Academy of Sciences, Dalian 116023, China

ARTICLE INFO

Article history: Received 23 May 2020 Accepted 27 October 2020 Available online 7 November 2020

Keywords: Carbon capture Membrane Electrochemical Catalytic Reactor

ABSTRACT

The concept of direct CO₂ capture and conversion has attracted significant interest from industries and academia in recent decades due to its potential to address the current grand challenge of global warming/climate change, rapid depletion of fossil fuels and realization of a future carbon neutral ecosystem. The incumbent benchmark technology for CO₂ capture is the post-combustion flue-gas "amine washing", which is energy intensive and costly for large-scale commercial implementation. The CO₂ conversion technologies, on the other hand, are still at their infancy with many technical challenges to overcome, but primarily being explored in laboratory-scale, low-temperature, solution-based and high-temperature, solid-oxide-based electrochemical cells with renewable electricity perceived as the energy input. In this article, we provide a comprehensive overview on an emergent class of high-temperature electrochemical CO₂ transport membranes that can capture and convert CO₂ into valuable chemicals in single catalytic reactor fashion. The review starts with the chemistry and transport theory of three basic types of membranes purposely designed for different CO₂ feedstocks and downstream conversions. A range of key functional materials used in these membranes and their microstructural/electrochemical properties important to the CO2 transport are then thoroughly discussed in conjunction with the effects of surface modifications and operating conditions. Several types of combined CO2 capture and conversion catalytic reactors based on these membranes are also assessed with a focus on their working principles, system configurations and performance demonstrations. Finally, challenges and prospective of these electrochemical CO2 transport membranes and their associated conversion reactors are candidly discussed for future development.

© 2020 Elsevier Ltd. All rights reserved.

E-mail addresses: huang46@cec.sc.edu (K. Huang), zhuxf@dicp.ac.cn (X. Zhu).

Abbreviation: ALD, atomic layer deposition; BCFZ, $BaCo_xFe_yZr_{1-x-y}O_{3-\delta}$; BYS, $Bi_{1.5}Y_{0.3}Sm_{0.2}O_3$; CO_2TM , CO_2 transport membrane; CP-PSFC, $Ce_{0.9}Pr_{0.1}O_{2-\delta}$ -Pr_{0.6}Sr_{0.4}Fe_{0.5}Co_{0.5}O_{3-\delta} (40-60 wt%); CSSO, $Ce_{0.80}Sm_{0.15}Sr_{0.05}O_{2-\delta}$; CVD, chemical vapor deposition; DMR, dry methane reforming; DOMR, dry-oxy methane reforming; GDC, gadolinium doped ceria; GPU, gas permeation unit; HF, hollow fiber; HTM, H_2 transport membrane; LCGFA, $La_{0.85}Ce_{0.1}Ga_{0.3}Fe_{0.65}Al_{0.05}O_{3-\delta}$; LNF, $LaNi_{0.6}Fe_{0.4}O_{3-\delta}$; LNC, $Li_{0.4}Ni_{1.6}O_2$; LSCF, $La_{0.6}Sr_{0.4}Co_{0.8}Fe_{0.2}O_{3-\delta}$; LSFCu, $La_{0.5}Sr_{0.5}Fe_{0.8}Cu_{0.2}O_{3-\delta}$; MC, molten carbonate; MCFCs, molten carbonate fuel cells; MECC, mixed electronic and carbonate-ion conductor; MHF, multichannel hollow fiber; MOCC, mixed oxide-ion and carbonate-ion conductor; NMP, Ni-MgO-1 wt% Pt; OCM, oxidative coupling of methane; ODHE, oxidative dehydrogenation of ethane; OTM, oxygen transport membrane; PBs, phase boundaries; RB, reverse Bouduoard; RWGS, reverse water gas shift; SC, steam cracking; SDC, samarium doped ceria; SFN, SrFe_{0.8}Nb_{0.2}O_{3-\delta}; SMR, steam methane reforming; SS, stainless-steel; SSAF, $Sm_{0.6}Sr_{0.4}Al_{0.3}Fe_{0.7}O_3$; TDHE, thermal dehydrogenation of ethane; TPB, triple phase boundaries; WF, wet feed gas; WGS, water gas shift; WGSR, water gas shift reaction; WS, wet sweep gas; XRD, X-ray diffraction; YSZ, yttria stabilized zirconia.

^{*} Corresponding authors.

Contents

1.		ductionduction						
2.	. The Chemistry and Phenomenological Description of the CO ₂ Transport							
	2.1. The CO ₂ permeation chemistry							
	2.2.	Phenomenological description of the CO ₂ transport						
		2.2.1. Bulk-diffusion controlled CO ₂ transport	5					
		2.2.2. Surface-reaction and bulk-diffusion co-controlled transport						
	2.3.	Terminology used for CO ₂ transport in CO ₂ TMs	ϵ					
3.	CO_2T	TM Materials and Performance Limiting Factors	7					
	3.1.	Materials	7					
		3.1.1. Molten carbonates						
		3.1.2. Oxide-ion conductors	7					
		3.1.3. Electronic conductors						
		3.1.4. Mixed ionic-electronic conductors	8					
	3.2.	Microstructure of solid matrix						
	3.3.	Membrane thickness effect						
	3.4.	Feed gas concentration effect	15					
		3.4.1. CO ₂ partial pressure						
		3.4.2. H ₂ partial pressure						
		3.4.3. H ₂ O partial pressure						
		3.4.4. Other impurities						
	3.5. Surface modifications							
4.	_	FM-Based Catalytic Membrane Reactors						
	4.1.	Coupling with methane reforming						
	4.2. Coupling with ethane dehydrogenation							
	4.3.	Coupling with H ₂ enrichment process						
5.		lenges and Potential Solutions						
5.1. Key challenges								
	5.2.	Membrane materials						
	5.3.	Microstructure/surface treatment						
	5.4.	CO ₂ capture and conversion						
	5.5.	Flux equation for triple-conducting membranes						
	5.6.	Physics-based modeling and system analysis						
6. Conclusions								
Declaration of Competing Interest								
		edgements						
Ref	erence	28	27					

1. Introduction

The CO₂ emission from burning of fossil fuels has significantly increased the CO2 concentration in our atmosphere since the industrial revolution. A dire consequence of the increased atmospheric CO₂ level is global warming and climate change, which have been observed to increasingly interrupt our daily life and economy in recent decades [1-4]. So far, three strategic methods have been proposed to curb CO2 concentration in the atmosphere: (1) increasing the use of environment-friendly energy resources (e.g., solar, wind, nuclear, etc.); (2) improving the efficiency of current energy utilization (e.g., fuel cells and advanced turbines); (3) capturing CO_2 at major emitting sources [5,6]. In these strategies, method-1 is attractive and growing rapidly in recent decades; however, the slow development of energy storage technology is limiting the large-scale deployment [7-10]. Method-2 takes a longer time to mature due to the nature of new technology development [11-15]. Even for the highly efficient hydrogen fuel cells, for example, hydrogen is mainly produced from steam methane reforming (SMR), a process that also emits large quantities of CO₂ [16,17]. Therefore, direct CO₂ capture (Method-3) from the existing power plants, such as flue gas, a major CO2 emitter, is currently regarded as the most practical solution to reduce the accumulation of the atmospheric CO_2 [4,18].

There are three major CO₂ capture technologies that have been developed and demonstrated for the existing and future fossil fu-

eled power plants: pre-combustion capture, post-combustion capture and oxy-fuel combustion capture [19-21]. The state-of-the-art CO_2 capture technology at commercial scale is represented by the post-combustion flue gas "amine washing" process based on reversible chemical absorption principle [2,22,23]. Physical adsorption based solid sorbents such as activated carbon [21], molecular sieves [24], and metal-organic framework [25,26] are also being developed to capture CO_2 towards commercial demonstrations. Thermochemical CO_2 capture based on calcium oxide looping is also widely studied in recent years, which is suited to separate CO_2 from such as post-combustion capture process [27]. With the captured CO_2 , the concentrated solar energy was also suggested to use as an energy input to produce hydrocarbon fuels through H_2O/CO_2 splitting in isothermal membrane reactors [28,29].

One major hurdle for these technologies to become commercial is the high energy consumption associated with CO_2 capture, which ultimately lowers the plant efficiency and increases the cost of electricity [30,31]. Membrane technology is a promising gas separation process due to its continuous operation and ability to treat gases at high flow rates. Compared to adsorption/absorption-based technologies, it presents the following advantages: lower energy consumption, good weight and space adsorption, no regeneration process, simple modular system, low capital and operation costs and environment-friendliness. There are many kinds of membranes for CO_2 capture, such as polymeric membranes and porous inorganic membranes. Polymeric membranes operated

List of symbols

 α_{ij} membrane selectivity Δ flux density of the species i J_i self-diffusivity of species i D_i C_i concentration of species i conductivity of species i σ_i σ_t total conductivity charge of species i z_i electrochemical potential of species i η_i chemical potential of species i μ_i porosity ε tortuosity τ tortuosity of the pore phase $\tau_{\rm p}$ tortuosity of the solid phase τ_{s} static potential φ positive integer n surface tension γ θ contact angle between solid matrix and MC ∇ symbol for gradient ideal gas constant (8.314 $| K^{-1} mol^{-1})$ R Faraday Constant (96485 C mol⁻¹) F T temperature (K) partial pressure of species i p_i p_i' partial pressure of species i at the feed side (high) partial pressure of species i at the sweep side (low) p_i CO₂ partial pressure at 1 atm p_0 permeability, m³(STP)m⁻¹s⁻¹Pa⁻¹ P_i $P_{M} \\$ permeance, GPU ko the total conductance at oxygen pressure of 1 atm m constant depending on temperature L membrane thickness σ^{o} constant permeation resistance through feed-side surface r' r^b permeation resistance through bulk region r" permeation resistance through sweep-side surface r_0' permeation resistance constant of the feed-side at CO₂ partial pressure of 1 atm $r_0^{\prime\prime}$ permeation resistance constant of the sweep-side at CO₂ partial pressure of 1 atm pore radius of solid matrix r sweep gas flow rate, mL min-1 Q

on the dissolution-diffusion principle are currently being developed at pilot scales [32-37], among which polybenzimidazole (PBI) membranes show special advantages in mechanical strength, thermal and chemical stability. The supported ionic-liquid membranes have been considered for pre-combustion CO2 capture process, but environmental concern on noxious ionic liquids as well as high cost limit its scale-up applications. The porous inorganic membranes, such as zeolite membranes and metal organic framework (MOF) membranes offer advantages of higher permeability. However, the stability of membrane materials under realistic operation conditions is still poor, especially at high temperatures. However, all these membrane technologies requiring pressurized operation to enhance the permeability and suffering permeability-selectivity tradeoff, are susceptible to water attack and incompatible with high temperatures. Readers can find more details on the above membrane-based CO₂ capture technologies in other reviews [38, 391.

effective membrane area, cm²

S

An alternative solution to overcome these barriers is to capture and convert the captured hot CO_2 directly into valuable products

(e.g. syngas, methanol, olefins and aromatics etc.). Such a capture-and-conversion combined system promises lower cost and higher efficiency since the thermal energy in the hot flue gas can be efficiently utilized, and separate reactant-purification (for O_2 , CO_2 and H_2), compression and transportation steps can be subsequently avoided.

The high-temperature CO₂ transport membranes (CO₂TMs) being reviewed in this article are perfectly positioned to enable such high-temperature CO₂ capture-and-conversion combined systems [40-42]. An immediate example is high-temperature CO₂TM reactor coupled with dry methane reforming (DMR) to produce syngas; the reaction requires 600-800 °C to overcome the thermodynamic constraint [43-45]. As a typical chemical-potential-gradient driven membrane reactor, CO₂TMs-based conversion reactors are modular, scalable, continuous, electricity-free, and more importantly, incrementally adding or removing CO₂ (or CO₂/O₂) along the length of a tubular plug-flow membrane, thus mitigating over-oxidation, shifting thermodynamic equilibrium and ultimately enhancing reactants conversion and product selectivity. Compared to the lowtemperature CO₂ conversion counterpart (e.g. electroreduction of CO₂ in aqueous electrolytes), CO₂TMs reactors are expected to be more efficient, selective, and easy to separate products due to favored thermodynamics/kinetics and gas-solid reactions. Compared to the conventional high temperature CaO-based cyclic CO₂ capture [46,47], on the other hand, the CO₂TM approach is also advantageous in process continuity, efficiency, and ability to achieve capture and conversion in single reactor.

Due to the relatively short history of the CO₂TM development, only one review article of the same topic published by Mutch et al. in early 2019 was noted [48], in which materials selection/properties and their interfacial compatibility on long-term stability are the primary focus. The difference of the present review, however, rests at its deeper and broader account of fundamental mechanisms, materials advancements, performance limiting factors, novel membrane reactor designs and important advances that have not been covered by Mutch et al. [48]. The review starts with the basic CO₂ capture chemistry and transport theory of three types of CO2TMs, followed by a detailed assessment of how constituent materials and their intrinsic properties, along with the surface modifications and operating conditions, affect CO2 flux density and stability of the membranes. Several membrane reactor concepts are then introduced to show how the captured CO2 is used as a soft oxidizer to convert feedstocks (e.g., methane and ethane) into valuable products (e.g. syngas and ethylene) via the oxidative route in single reactor designs. Finally, future development, challenges and prospective of CO₂TMs and the associated reactors are candidly discussed. Fig. 1 illustrates a summary of the main components covered by this review.

2. The Chemistry and Phenomenological Description of the CO_2 Transport

The CO₂TM reviewed here is electrochemical in nature and consisted of a porous solid phase scaffold infiltrated with a molten carbonate (MC) phase. The porous solid phase acts as an ionic and/or electronic conductor and placeholder for the MC phase, while the MC phase acts as the carbonate ionic conductor and gas sealant. Thus, the membrane is microstructurally dense. Based on the charge carriers of the solid material, CO₂TM can be grouped into three categories: (1) mixed oxide-ionic and carbonate-ionic conductor (MOCC) membrane, (2) mixed electronic and carbonate-ionic conductor (MECC) membrane, and (3) mixed electronic, oxide-ionic and carbonate-ionic conductor (MEOCC) membrane.

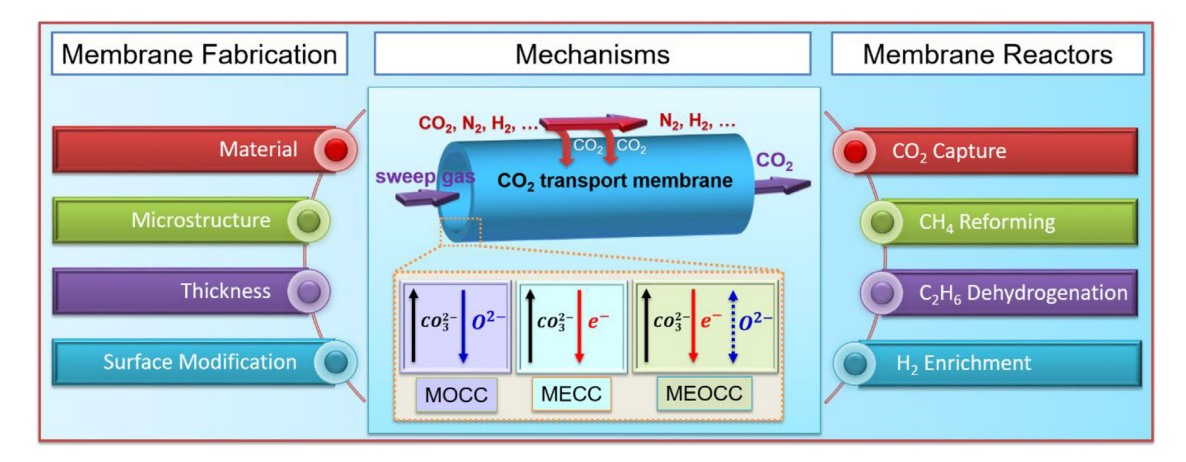


Fig. 1. A schematic summary of the main components in this review. MOCC: <u>mixed oxide-ionic and carbonate-ionic conductor</u>; MECC: <u>mixed electronic, oxide-ionic and carbonate-ionic conductor</u>.

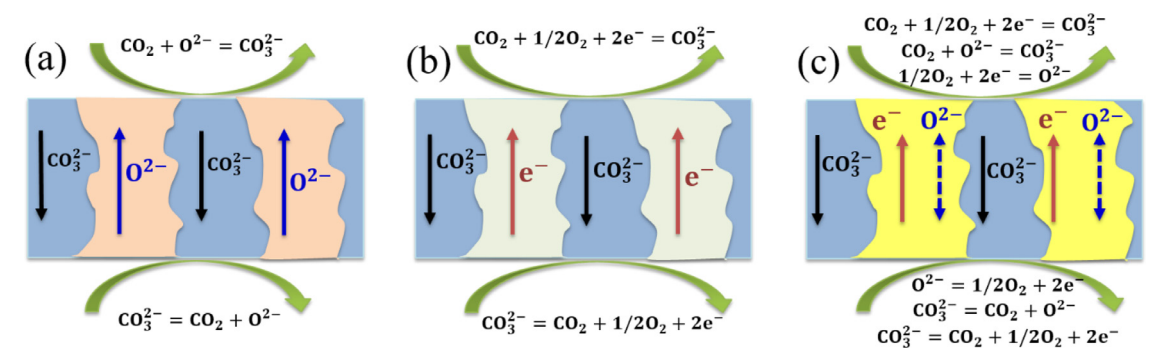


Fig. 2. Chemistry of different CO₂TMs: (a) MOCC, (b) MECC, (c) MEOCC.

2.1. The CO₂ permeation chemistry

The chemistry that enables MOCC, MECC and MEOCC membranes to permeate CO2 and O2 are illustrated in Fig. 2a, b and c, respectively. In common, the CO2 transport through these membranes is taken in the form of CO_3^{2-} . The difference among the three CO₂TMs lies in the charge-balancing counter ions. For the MOCC membrane, see Fig. 2a, CO₃²⁻ is formed by the reaction between CO₂ and O²⁻ (from the ceramic phase) on the feed side (the top) of the membrane. CO_3^{2-} is then transported under the chemical potential gradient of CO₂ to the sweep side (the bottom) of the membrane through the MC phase, while being chargecompensated by a concomitant opposite flow of O^{2-} in the oxideionic conductor phase. Therefore, the MOCC membrane is more suited for CO₂ separation from a CO₂-rich gas, such as a mixture of CO2 and H2 (product of water-gas-shift-reaction, WGSR) in the pre-combustion process [49]. Since CO₂ is transported in the form of CO₃²⁻, the theoretical membrane selectivity (the ratio between permeated CO_2 and the other permeated gases) of CO_2 is infinite.

Similarly, CO_3^{2-} transport can also be charge-compensated by electrons (e⁻), see Fig. 2b, in the MECC membrane. To transport CO_3^{2-} , O_2 is needed with CO_2 in the feed side to satisfy the enabling reaction: $CO_2 + 1/2O_2 + 2e^- = CO_3^{2-}$, and CO_2 with O_2 are collected at the sweep side through the reverse reaction: $CO_3^{2-} = CO_2 + 1/2O_2 + 2e^-$, after CO_3^{2-} is transported through the MC phase. Therefore, it is more adequate for CO_2 capture from an oxidizing stream, such as post combustion flue gas (a main CO_2 emitter, containing CO_2 , O_2 , O_2 , and O_2 , and O_2 flux ratio is 2:1, and activation energies for CO_2 and O_2 fluxes are very close [50-52]. While the permeated gas is not strictly CO_2 selec-

tive, it has been suggested to recycle back to combustion chamber of oxy combustion for controlling combustion temperature [43]. It has also been proposed to convert to CO_2 and H_2O by utilizing syngas $(CO+H_2)$ as the sweep gas via the following reactions: $CO_3^{2-} + H_2 = CO_2 + H_2O + 2e^- + \Delta$ (here Δ means heat) and $CO_3^{2-} + CO = 2CO_2 + 2e^- + \Delta$. The advantages of this capture process are the production of a pure stream CO_2 and H_2O for easy downstream CO_2 separation and large amount of waste heat to be utilized.

For MEOCC membranes shown in Fig. 2c, $\mathrm{CO_3}^{2-}$ charge compensation mechanisms depend on feed-gas composition. If no $\mathrm{O_2}$ species in the feed side, the MEOCC acts like a MOCC membrane [53]. If there is $\mathrm{O_2}$ in the feed side, however, $\mathrm{CO_3}^{2-}$ is mainly charge-compensated by $\mathrm{e^-}$, since electronic conductivity dominates in most mixed oxide-ionic and electronic conductors; $\mathrm{O^{2-}}$ may be transported from the feed side to the sweep side or vice versa, depending on the magnitude of oxygen partial pressure on the feed side. If $\mathrm{O^{2-}}$ is transported from the sweep side to the feed side, the ratio of $\mathrm{CO_2:O_2}$ permeated is higher than 2:1, which has been observed by Lan et al. [54], Zhang et al. [55] and Ovalle-Encinia et al. [56]. If $\mathrm{O^{2-}}$ is transported from the feed side to the sweep side (the same direction as $\mathrm{CO_3^{2-}}$), the $\mathrm{CO_2:O_2}$ flux ratio is lower than 2:1 due to the additional $\mathrm{O_2}$ permeation [57].

On the feed-side surface of a membrane, the ionization of CO_2 may take place along two-phase boundaries between feed gas and MC forming intermediate $C_2O_5^{2-}$ through the reactions of $CO_2 + CO_3^{2-} = C_2O_5^{2-}$ and $CO_2 + O^{2-} = CO_3^{2-}$ [58]. A schematic illustration of MOCC membranes is shown in Fig. 3a; once the $C_2O_5^{2-}$ (pyrocarbonate) intermediate is formed, it immediately reacts with O^{2-} at the SDC/MC (SDC: Sm_2O_3 doped CeO_2) interface to produce CO_3^{2-} via $C_2O_5^{2-} + O^{2-} = 2CO_3^{2-}$. Then, the pro-

Fig. 3. (a) A 3D-schematic illustrating electrochemical reactions occurring at 3PBs to 2PBs in MOCC membranes; SDC: Sm_2O_3 doped CeO_2 ; MC: molten carbonate; PB: phase boundaries. Adapted from ref. [59] with permission from the PCCP Owner Societies, Copyright 2013. (b) A 3D representation of CO_4^{2-} charge-transfer model for the silver-carbonate membrane as a representative of MECC. Adapted from ref. [60] with permission from Elsevier, Copyright 2014.

duced CO_3^{2-} migrates to the sweep side, where it releases CO_2 and O^{2-} through $CO_3^{2-} = CO_2 + O^{2-}$. The validity of $C_2O_5^{2-}$ species has been confirmed by *in-situ* Raman spectroscopy and DFT calculations [59].

If O_2 is present in the feed side of a MECC, it reacts with CO_3^{2-} to form CO_4^{2-} on the membrane surface through $1/2O_2 + CO_3^{2-} = CO_4^{2-}$, see Fig. 3b; the produced CO_4^{2-} then combines with e⁻ (from the electronic conductor phase) and CO_2 via sequential reactions to form CO_3^{2-} , i.e. $CO_4^{2-} + e^- = CO_3^{2-} + (O^-)$, $(O^-) + e^- = O^{2-}$, and $O^{2-} + CO_2 = CO_3^{2-}$ [60].

2.2. Phenomenological description of the CO₂ transport

Several phenomenological models have been built so far to describe the CO_2 transport process in $\mathrm{CO}_2\mathrm{TMs}$. With a good and reliable model, researchers can better understand the property-performance relationship and identify the key performance limiters, which could in turn provide guidance for future development of advanced membrane materials.

2.2.1. Bulk-diffusion controlled CO2 transport

The bulk diffusion was initially assumed as the rate-limiting step to the CO_2 transport process. Therefore, the classical Wagner transport equation is used to describe the permeation flux J_i of the active species i:

$$J_{i} = \frac{D_{i}C_{i}}{RT}\nabla\eta_{i} = -\frac{\sigma_{i}}{(z_{i}F)^{2}}\nabla\eta_{i} = -\frac{\sigma_{i}}{(z_{i}F)^{2}}(\nabla\mu_{i} + z_{i}F\nabla\phi)$$
 (1)

where D_i , C_i , σ_i and z_i are self-diffusivity, concentration, conductivity and charge of species i, respectively; η_i and μ_i are electrochemical and chemical potentials of species i, respectively; ϕ is the static potential; ∇ is a symbol of gradient; R, F, and T are ideal gas constant (8.314 J K⁻¹ mol⁻¹), Faraday constant (96485 C mol⁻¹), and temperature (K), respectively.

For MOCC membranes, assuming homogeneous distribution of MC within solid matrix and the local chemical equilibrium $CO_2 + O^{2-} = CO_3^{2-}$, a microstructure-corrected Wagner flux equation is derived to describe the relationship between CO_2 permeation flux (J_{CO_2}) and CO_2 partial pressure (p_{CO_2}) as follows [61]:

$$J_{\text{CO}_2} = -\frac{RT}{4F^2L} \int_{\text{p}''_{\text{CO}_2}}^{\text{p}'_{\text{CO}_2}} \frac{\left(\frac{\varepsilon}{\tau_p} \sigma_{\text{CO}_3^2-}\right) \left(\frac{1-\varepsilon}{\tau_s} \sigma_{\text{O}^2-}\right)}{\left(\frac{\varepsilon}{\tau_p} \sigma_{\text{CO}_3^2-}\right) + \left(\frac{1-\varepsilon}{\tau_s} \sigma_{\text{O}^2-}\right)} d \ln p_{\text{CO}_2}$$
 (2)

where ε is the porosity of the porous solid matrix; τ_p and τ_s are the tortuosity of pore (the ratio between pore length and membrane thickness) and solid phases, respectively; $\sigma_{CO_3^2}$ and σ_{O^2} are the ionic conductivities of CO_3^{2-} and O^2- , respectively; p'_{CO_2} and p''_{CO_2} are the CO_2 partial pressures at the feed side (high) and sweep side (low), respectively. Normally, $\sigma_{CO_3^2-}$ is at least one magnitude greater than σ_{O^2-} in a MOCC membrane, thus Eq. (2) can

be simplified into [59,61]

$$J_{CO_2} = \frac{RT}{4F^2L} \left(\frac{1-\varepsilon}{\tau_s} \sigma_{0^{2-}} \right) \ln \frac{p'_{CO_2}}{p''_{CO_2}}$$
 (3)

The linear relationship between J_{CO_2} and $\ln p_{CO_2}$ is confirmed by experiments [62-64]. However, straight lines do not pass the origin of J_{CO_2} vs. $\ln (p'_{CO_2}/p''_{CO_2})$ as predicted by Eq. (3). Therefore, a new lower-law flux equation was proposed to describe the CO_2 flux [65]:

$$J_{CO_2} = \frac{k^0 \emptyset^m RT}{4F^2 L n_0} \left(p'_{CO_2}^{n_0} - p''_{CO_2}^{n_0} \right)$$
 (4)

where k^0 is defined as the total conductance at 1 atm oxygen pressure ($k^0 \sim \frac{1-\varepsilon}{\tau_s} \sigma_{O^{2-}}$); m is a temperature-dependent constant; $n_0 = mq$; q is a constant (in the case that O_2 is considered as the impurity of CO_2 or N_2 , q=1.). In a SDC-MC membrane (MOCC), straight lines of J_{CO_2} vs. ($p_{CO_2}^{'n} - p_{CO_2}^{'n}$) pass through the origin of coordinate, with n=0.125 and 0.5 at 900 and 700 °C, respectively [64-67]. From Eqs. (3) and (4), it is evident that J_{CO_2} can be improved by increasing temperature (T), decreasing membrane thickness (L), optimizing porosity (ε) and tortuosity (τ), increasing oxide-ionic conductivity ($\sigma_{O^{2-}}$) and CO_2 partial pressure gradient $\left(\frac{p'_{CO_2}}{p''_{CO_2}}\right)$. In the next section, efforts in all these aspects to enhance

 J_{CO_2} of MOCC membranes will be discussed in detail. For MECC membranes, assuming homogenous phase distribution in the membrane and considering local chemical equilibrium $CO_2 + 1/2O_2 + 2e^- = CO_3^{2-}$, Eq. (1) can be applied to reach J_{CO_2} as [60]

$$J_{CO_{2}} = -\frac{3RT}{8F^{2}L} \frac{p'_{CO_{2}}, p'_{O_{2}}}{p''_{CO_{2}}, p''_{O_{2}}} \frac{\left(\frac{\mathcal{E}}{\tau_{p}} \sigma_{CO_{3}^{2-}}\right) \left(\frac{1-\mathcal{E}}{\tau_{s}} \sigma_{e^{-}}\right)}{\left(\frac{\mathcal{E}}{\tau_{p}} \sigma_{CO_{3}^{2-}}\right) + \left(\frac{1-\mathcal{E}}{\tau_{s}} \sigma_{e^{-}}\right)} d \left(lnp_{CO_{2}} + \frac{1}{2}lnp_{O_{2}}\right)$$
(5

Here σ_{e^-} is electronic conductivity of the solid matrix; p'_{O_2} and p''_{O_2} are oxygen partial pressures at the feed side and sweep side, respectively. Generally, σ_{e^-} (e.g. $\sim 10^4$ S cm $^{-1}$ of Stainless steel [68], $\sim 10^5$ S cm $^{-1}$ of Ag [50]) of the solid matrix is much higher than $\sigma_{CO_3^{--}}$ (0.5-2 S cm $^{-1}$) of the MC phase. Then Eq. (5) can be simplified into

$$J_{CO_2} = -\frac{3RT}{8F^2L} \frac{p'_{CO_2}, p'_{O_2}}{p''_{CO_2}, p''_{O_2}} \frac{\varepsilon}{\tau_p} \sigma_{CO_3^2} d \left(lnp_{CO_2} + \frac{1}{2} lnp_{O_2} \right)$$
 (6)

If $\sigma_{CO_3^{2-}}$ has the following relation with p_{CO_2} and p_{O_2} [69],

$$\sigma_{\text{CO}_3^{2-}} = \sigma^0(p_{\text{CO}_2} p_{\text{O}_2}^{1/2}) \tag{7}$$

Then substitution of Eq. (7) into Eq. (6) leads to

$$J_{CO_{2}} = \frac{3RT}{8F^{2}L} \frac{\varepsilon}{\tau_{p}} \sigma^{0} \left(p'_{CO_{2}} p'_{O_{2}}^{'1/2} - p''_{CO_{2}} p''_{O_{2}}^{1/2} \right)$$
 (8)

where σ^o is a constant. A nearly perfect linear relationship between J_{CO_2} and $(p_{CO_2}p_{O_2}^{1/2})$ is obtained [69], suggesting that Eq. (8) is a proper expression of J_{CO_2} for MECC membranes.

Like MOCC membranes, J_{CO_2} can be improved by increasing temperature, decreasing membrane thickness, optimizing porosity and tortuosity, increasing carbonate ionic conductivity, and increasing CO_2 and O_2 partial pressure gradients.

However, for MEOCC membranes, J_{CO_2} expression is more complicated; it depends on feed gas composition, electronic conductivity and oxide-ion conductivity because there are three kinds of electrical-charge species (oxide-ion, electron, and carbonate-ion) involved in the permeation process, see Fig. 2c. Rui et al. [70] studied the relationship between CO_2 flux density and operating conditions. For the case of no O_2 in the feed side, no electron is involved in the reaction and permeation process, then Eq. (2) or (3) can be used to calculate the CO_2 flux. For the case with O_2 in the feed side, the following equation is adequate to calculate J_{CO_2} [70].

$$J_{CO_{2}} = \frac{\varepsilon}{\tau_{p}} \frac{\sigma_{CO^{2-}} \left[(\sigma_{e^{-}} + \sigma_{O^{2-}}) RT ln \left(\frac{p'_{CO_{2}}}{p'_{CO_{2}}} \right) + \left(\frac{\sigma_{e^{-}}}{2} \right) RT ln \left(p'_{O_{2}} / p''_{O_{2}} \right) \right]}{4F^{2} L \left[(\sigma_{e^{-}} + \sigma_{O^{2-}}) - 2 \left(\frac{\varepsilon \tau_{s}}{(1 - \varepsilon) \tau_{p}} \right) \sigma_{CO^{2-}} \right]}$$
(9)

Eq. (9) suggests that J_{CO_2} can be enhanced by the presence of oxygen in feed side, increasing electronic conductivity of solid matrix, increasing oxide-ionic conductivity at a low electronic conductivity ($\leq 0.1~\rm S~cm^{-1}$); while J_{CO_2} decreases with increasing oxide-ionic conductivity at a high electronic conductivity ($> 1~\rm S~cm^{-1}$). An ordered pore structure of the solid matrix is also suggested to benefit both CO_2 and O_2 permeations [71].

2.2.2. Surface-reaction and bulk-diffusion co-controlled transport

In some cases, such as the membrane thickness is thin, surface reactions on two sides of a CO₂TM will control the CO₂ transport process. New flux equations are required to describe such a mixed surface-reaction and bulk-diffusion controlled permeation process. To the best of our knowledge, there are no related flux equations reported for CO2TMs. However, similar flux equations have been developed for oxygen transport membranes (OTMs) [72-74]. For example, a model was built to simulate the oxygen permeation through a mixed conducting membrane by coupling the bulk diffusion of oxide-ionic and electronic transport with two surface reactions [75-77]. Three assumptions are used to establish the flux equation: (i) transport characteristics of the electrons and oxideions in a given region are constant regardless of the location and chemical potential of oxygen; (ii) gas-phase oxygen diffusion is fast enough to ignore the concentration gradient on the surface; (iii) all the steps of the permeation are under isothermal conditions, and the law of mass action is applicable to gas exchange reactions on the gas-solid interfaces. For CO₂TMs, similar assumptions can be adopted to build the flux equation: (i) transport characteristics of carbonate ions, electrons and oxide-ions in a given region are constant regardless of the location and chemical potential of CO₂; (ii) gas-phase CO₂ diffusion is fast enough to neglect the concentration gradient; (iii) all the steps of the CO₂ permeation are under isothermal conditions, and the law of mass action is applicable to CO₂ exchange reactions on the gas-solid-liquid interfaces. Therefore, the following surface-bulk mixed controlled CO2 flux equations for CO₂TMs are developed:

$$J_{\text{CO}_2} = -\frac{1}{2^2 F^2} \frac{1}{r' + r^b + r''} \Delta \mu_{\text{CO}_2}^{\text{tot}} = -\frac{1}{2^2 F^2} \frac{1}{r^{\text{tot}}} \Delta \mu_{\text{CO}_2}^{\text{tot}} \tag{10}$$

$$\Delta\mu_{\text{CO}_2}^{\text{tot}} = \text{RTIn} \frac{p_{\text{CO}_2}^{"}}{p_{\text{CO}_2}^{"}} \tag{11}$$

$$\mathbf{r}^{\text{tot}} = \mathbf{r}' + \mathbf{r}^{\text{b}} + \mathbf{r}'' \tag{12}$$

where r, r^b , r^v are the permeation resistances through feed-side surface, bulk region and sweep-side surface, respectively; r^{tot} is the total permeation resistance across the membrane; F is the Faraday constant; $\Delta\mu_{02}^{tot}$ is the total CO_2 chemical potential gradient across the membrane. Normally, the specific resistance of the surface reaction is a function of CO_2 partial pressure. A simple power law can be used to describe the relationship between CO_2 partial pressure and surface reaction resistance by:

$$r' = r_0' \left(\frac{p_{\text{CO}_2}^{'}}{p_0}\right)^{-\frac{1}{n'}} \tag{13}$$

$$r'' = r_0'' \left(\frac{p_{CO_2}''}{p_0}\right)^{-\frac{1}{n''}} \tag{14}$$

where p_0 , r'_0 , and r''_0 are CO_2 partial pressure at 1 atm, permeation resistance constant of the feed-side and sweep-side at CO_2 partial pressure of 1 atm, respectively. n' and n'' are positive integers, reflecting the order of the reaction. Since r'_0 , r''_0 and r^b can be obtained by fitting Eqs. (10-12), r' and r'' at a given temperature and CO_2 partial pressure can be calculated by Eqs. (13) and (14). Finally, n' and n'' values, exchange coefficients and diffusion coefficient can be calculated from the obtained experimental data. Therefore, it is possible to distinguish how much the CO_2 transport is controlled by bulk diffusion and surface exchange reactions.

2.3. Terminology used for CO₂ transport in CO₂TMs

There are several terminologies in the literature describing CO $_2$ permeation performance through gas separation membranes. Knowing the meaning of each term will be useful to correctly compare the performance among different membranes. **Permeation flux** (J_i) is a commonly used term to describe the volume of gas (i) permeating through the membrane per unit area and unit time. The SI unit is $m^3\ m^{-2}\cdot s^{-1}$, although others such as $mL\ cm^{-2}\cdot min^{-1}$ are often used as well. For gas-phase transport, the volume is strongly dependent on pressure and temperature. As such, the permeation flux is often given in terms of a "standard condition or STP" defined as 273.15 K and 1 atmosphere (1.01325 bar), under which 1 mole of ideal gas is equivalent to 22400 mL. With the constant stirring tank (CST) model, J_i can be experimentally determined by

$$J_i \left(\text{mL min}^{-1} \text{ cm}^{-2} \right) = \frac{C_i}{C_{\text{sweep gas}}} \times \frac{Q}{S} \tag{15}$$

where, C_i and $C_{sweep\ gas}$ are the GC-measured and leak-corrected concentration of species i and that of sweep gas (such as Ar), respectively; Q (mLmin⁻¹) is the flow rate of the sweep gas, and S (cm²) is the effective surface area of the membrane.

However, the issue with reporting **permeation flux** (J_i) is that J_i is a function of both the intrinsic properties of the membrane and operating condition of the experiments (*e.g.* feed-gas concentration, pressure, temperature, membrane thickness, etc.). Therefore, using J_i to compare membrane's performance obtained under different operating conditions is not objective.

A fairer way to compare membrane's permeation performance is to use the term $Permeability\ (P_i)$ or $Permeation\ Coefficient\ defined\ by:$

(10)
$$\mathbf{P_i} = \frac{\mathbf{J_i} \times \mathbf{L}}{\mathbf{p'_i} - \mathbf{p''_i}}$$
 (16)

Table 1The carbonate ionic conductivity of different molten carbonates.

Molten Carbonates	$\sigma_{{\rm CO_3}^{2-}}$ @ 923 K (S cm $^{-1}$)	$\sigma_{{\rm CO_3}^{2-}}$ @ 1073 K (S cm $^{-1}$)	$\sigma_{{\rm CO_3}^{2-}}$ @ 1173 K (S cm $^{-1}$)	Ref.
(Li-Na-K) ₂ CO ₃	1.434	2.12	2.57	[85]
(Li-Na) ₂ CO ₃	2.06	2.65	3.53	[82]
(Li-K) ₂ CO ₃	1.31	1.77	2.46	[82, 86]
$(Na-K)_2CO_3$	-	-	2.25	[82]

Note: $(\text{Li-Na-K})_2\text{CO}_3$, Li_2CO_3 : Na_2CO_3 : Ka_2CO_3 =43.5:31.5:25 mol%; $(\text{Li-Na})_2\text{CO}_3$, Li_2CO_3 : Na_2CO_3 =52:48 mol%; $(\text{Li-K})_2\text{CO}_3$, Li_2CO_3 : K_2CO_3 =62:38 mol%; $(\text{Na-K})_2\text{CO}_3$, Na_2CO_3 : K_2CO_3 =60:40 mol%.

where $\mathbf{J_i}$ is normalized by the driving force (partial pressure differential $(p_i'-p_i'')$ of the active species i) and membrane thickness L, making $\mathbf{P_i}$ a better representative of the intrinsic properties of the membrane. **Permeability** has a SI unit of $\mathrm{m^3(STP)}~\mathrm{m^{-1}}~\mathrm{s^{-1}}~\mathrm{Pa^{-1}}$. Barrer (1 Barrer = 10^{-10} (cm³@STP cm)/(cm² s cm-Hg)) was early introduced as a practical unit for **permeability** for easy comparison of the suitability of a material to be used for membrane gas separation.

Derived from **Permeability**, **Permeance** (P_M) is defined as the ratio of the **Permeability** to the membrane thickness (L). It is analogous to a mass transfer coefficient for a given species permeating through the membrane at a given thickness.

$$\mathbf{P_M} = \frac{\mathbf{P_i}}{\mathbf{L}} = \frac{\mathbf{J_i}}{\mathbf{P_i'} - \mathbf{P_i''}} \tag{17}$$

 P_M is an important parameter when comparing the separation suitability of membranes for mixed gases. In addition to its SI unit, a practical unit often used is GPU (gas permeation unit);1GPU ==10^-6 cm^3(STP) cm^-2 s^-1 cm-Hg^{-1} ==7.6 \times 10^{-9} m^3(STP) m^{-2} s^{-1} kPa^{-1} = 3.35 \times 10^{-3} kmol \cdot m^2 s^{-1} kPa^{-1}.

In gas separation, the **membrane selectivity** (α_{ij}) (aka. permselectivity) is used to compare the separating efficiency of a membrane for 2 (or more) species. It is defined as the ratio of the permeability or permeance or flux of components i and j through the membrane:

$$\alpha_{ij} = \frac{P_i}{P_j} = \frac{P_{Mi}}{P_{Mj}} = \frac{J_i}{J_i} \tag{18}$$

For traditional size-exclusive membranes, α_{ij} is determined by the relative populations of various pore sizes, actual pore size, molecule deformability, and molecular adsorption ability. The permeation ability and selectivity of this class of membranes are subject to Robeson's upper bound rule. In contrast, CO_2 is the only species transportable through the CO_2TMS due to the electrochemical nature. Therefore, CO_2TM has an infinite theoretical selectivity to CO_2 . However, in reality, there is always a certain level of physical leakage through the imperfect sealing (pin holes, etc.) in presumably dense microstructure of the membrane. Therefore, α_{ij} for CO_2TMS is often determined by the ratio of CO_2 flux to that of other species (e.g. N_2) present in the capture gas.

3. CO₂TM Materials and Performance Limiting Factors

Following the fundamental insights from the above flux equations, in this section, we mainly focus on the effects of materials, microstructures, thickness, surface modification, and operating conditions on CO_2 flux and long-term stability.

3.1. Materials

 ${\rm CO_2TMs}$ are consisted of a (or two) porous solid matrix filled with a molten carbonate (MC) phase. The latter serves as a carbonate ionic conductor and a sealant to make the membrane gastight. The solid matrix materials are porous metals or oxide-ionic conducting ceramics, providing the needed electronic and/or oxide-ionic conduction and charge-compensation for the MC phase.

Therefore, solid matrix materials must satisfy the following requirements: 1) oxide-ionic, or electronic, or mixed oxide-ionic and electronic conductor; 2) good wettability with MC; 3) chemically stable at high temperatures in CO₂-containing gases; 4) chemically compatible with MC phase; 5) high mechanical strength.

3.1.1. Molten carbonates

From the flux equations Eqs. 2, 6 and (9), the CO₂ flux depends strongly on MC's ionic conductivity. A commonly used MC is the ternary eutectic carbonate system containing (Li-Na-K)2CO3 with a molar ratio of 43.5:31.5:25 [53,64,68,78,79] and melting point of ~397 °C. Some binary eutectic carbonates, such as (Li-Na)₂CO₃ with a molar ratio of 52:48 and melting point of 495 °C, and (Li-K)₂CO₃ with a molar ratio of 62:38 and melting point of 498 °C, and (Na-K)2CO3 with a molar ratio of 41:59 and melting point of 710 °C, have also been tried in CO₂TMs [49,50,52,80,81]. It was reported that the conductivity of binary MCs Li₂CO₃-X₂CO₃ (X= Na, K, Rb, and Cs) or Na₂CO₃-Z₂CO₃ (Z= K, Rb, and Cs) decreases with ionic radius of X or Z [82]. In addition, the order of ionic conductivity of the single carbonate is $Li_2CO_3 > Na_2CO_3 > K_2CO_3$ [83,84]. Therefore, (Li-Na)₂CO₃ binary carbonate shows the highest ionic conductivity among the reported four MC systems, see Table 1. Note that the difference in ionic conductivity among these MCs is noticeable but insignificant.

For MOCC membranes, since the conductivity of MC is much higher than that of the ceramic oxide-ionic conducting phase [87,88], the oxide-ion transport controls the bulk diffusion process in the CO₂ permeation process, while MC phase has a little effect on the CO₂ flux according to Eqs. (2-4). For example, Wade et al. studied the effect of (Na-K)2CO3 binary carbonate and (Li-Na-K)₂CO₃ ternary carbonate in YSZ-MC membranes; similar CO₂ fluxes were observed at 750 °C [89]. If the membrane is operated in the temperature range of 400-500 °C, (Li-Na-K)₂CO₃ ternary carbonate is a better choice due to its low melting point. Otherwise, (Li-Na)2CO3 binary carbonate is a better choice due to its higher ionic conductivity. The other physical and chemical properties of these MCs, such as viscosity, density, surface tension, and gas solubility are similar. Therefore, MCs show less effect on CO2 permeation performance than the oxide-ion phase for MOCC membranes. As such, the main research interests on CO₂TMs are focused on solid matrix materials, including oxide-ion conductors, electron conductors, and mixed electron and oxide-ion conductors.

3.1.2. Oxide-ion conductors

MOCC membranes transport solely CO_2 because CO_2 is directly ionized by O^{2-} from the oxide-ion conductor through the surface reaction $CO_2 + O^{2-} = CO_3^{2-}$. Therefore, the higher the oxide-ion conductivity, the higher the CO_2 flux. Oxide-ion conductors, such as yttria stabilized zirconia (YSZ) [90], samarium doped ceria (SDC) [49,61,91], gadolinium doped ceria (GDC) [92,93], and $Bi_{1.5}Y_{0.3}Sm_{0.2}O_3$ (BYS) [63] have been experimented in MOCC membranes. Wade et al. [89] compared CO_2 flux of YSZ-MC membrane with non-oxide-ionic conductor CO_2 flux of YSZ-MC membrane with non-oxide-ionic conductor CO_2 flux of YSZ-MC membrane never exceeded CO_2 flux of CO_2 membrane never exceeded CO_2 flux of CO_2 membrane never exceeded CO_2 flux of CO_2 flux of

Table 2The ionic conductivity of different solid matrix phases.

0 11 1	$\sigma_{0^{2-}}$ (S cm $^{-1}$)						D 6
Solid phase	773 K	873 K	923 K	973 K	1073 K	1173 K	– Ref.
YSZ	0.001	0.005	0.01	0.015	0.043	0.106	[78, 89]
GDC	0.006	0.017	0.029	0.04	0.086	0.167	[94]
SDCa	0.002	0.007	0.012	0.021	1	1	[49]
SDCb	1	1	1	0.017	0.046	0.107	[65]
BYS	0.011	0.068	0.137	0.197	1	1	[66, 93]

YSZ: $Y_{0.16}Zr_{0.84}O_{2-\delta}$; GDC: $Ce_{0.9}Gd_{0.1}O_{1.95}$; SDC: $Ce_{0.8}Sm_{0.2}O_{1.9}$ (a: prepared by co-precipitated method)

cm $^{-2}$ in flux) at 750 °C. This result proves that non-oxide-ion conducting Al $_2$ O $_3$ supported MOCC membrane cannot transport CO $_2$ with meaningful permeability. YSZ-MC membrane shows a CO $_2$ permeability of 5-6 × 10 $^{-12}$ mol m $^{-1}$ s $^{-1}$ Pa $^{-1}$ ($^{\sim}$ 0.133 mL min $^{-1}$ cm $^{-2}$ in flux) at 750 °C. However, YSZ has a low oxide-ionic conductivity, see Table 2, and reacts irreversibly with lithium carbonate, forming lithium zirconate at a low CO $_2$ partial pressure [89]. Therefore, YSZ is not a good matrix material for MOCC membranes either.

The fluorite structured BYS is known to have a higher oxideionic conductivity than YSZ. As expected, a higher CO2 flux of 0.083 mL min $^{-1}$ cm $^{-2}$ ($\sim 1.1 \times 10^{-8}$ mol m $^{-2}$ s $^{-1}$ Pa $^{-1}$ in permeance) was observed with BYS-MC ((Li-Na-K)2CO3) membrane at 650 °C [63], comparing to $\sim 0.01 \text{ mL min}^{-1} \text{ cm}^{-2} (0.12 \times 10^{-8} \text{ mol})$ m^{-2} s⁻¹ Pa⁻¹ in permeance) of YSZ-MC membrane [89]. In addition, CO₂ flux was increased by 2.5 times with the phase of BYS changing from rhombohedral to cubic structure due to the higher oxide-ionic conductivity of the latter. However, the reported CO2 flux of BYS-MC membrane is lower than that of SDC (or GDC)-MC membrane [65,66], see Table 3, even though BYS has a higher oxide-ion conductivity than SDC (or GDC). This is because the poor wettability between BYS and MC, causing the pores in the BYS matrix not being fully filled by MC to form continuous MC network. Pore surfaces modification by Al₂O₃ layer is required to overcome the poor wettability and achieve dense microstructure because Al₂O₃ can fully wet MC [63]. However, Al₂O₃ coating partly blocks the reaction $C_2O_5^{2-} + O_5^{2-} = 2CO_3^{2-}$ at BYS/MC boundaries, see Fig. 3a, resulting in a lower CO2 flux. Therefore, in addition to oxide-ion conductivity, chemical compatibility and wettability with MC are important properties for solid porous matrix materials.

Up to now, doped CeO₂ are the best MOCC membrane matrix materials, largely due to their high oxide-ion conductivity, good chemical stability, chemical compatibility and wettability with MC at high temperatures. Thus, MOCC membranes based on doped CeO₂ matrix are widely adopted to evaluate flux stability [96] and effects of membrane thickness [97], matrix geometry (plate or tubular) [66], carbonate composition and membrane microstructure [49,91], system pressure [65], impurities (e.g. H_2S [98,99], SO₂ [100]) and operating conditions (e.g. syngas [65,101,102], H₂O [103], CH₄ [91,92]). For example, good chemical stability of both Gd- and Sm-doped CeO2 has been reported for different atmospheres: 15% H₂, 34% CO, and 51% H₂O; 21%H₂, 48% CO, and 31% H₂O and 98% H₂ and 2% CO₂ [96]; the results are shown in Fig. 4a and 4b. By systematically studying the effect of MC volume ratio in SDC-MC membranes, Zhang et al. [49] reported the highest CO2 flux density at an SDC:MC ratio of 50:50 vol%. In addition, the CO2 flux calculated by Eq. (3) agrees well with those independently measured values for a 1.2-mm-thick membrane, see Fig. 4c, which proves that CO₂ permeation is indeed controlled by the bulk oxide-ion transport. It was also found that disk-shaped SDC-MC membrane shows a higher CO₂ flux than tube-shaped one, see Fig. 4d, due to a higher particle packing density of green bodies (before sintering) in disk samples than tubular counterparts [66]; the former leads to a better particle connections and thus higher ionic conductivity after sintering. Furthermore, Norton et al. [65] reported that SDC-MC membrane can withstand a transmembrane pressure difference up to 5 atm in either CO₂-N₂ or simulated syngas mixture for 35 days, paving the way for pressurized CO₂ capture and conversions.

3.1.3. Electronic conductors

The first MECC membrane was reported by Lin et al. with a stainless-steel (SS) as the porous matrix and electronic conductor [68]. A CO_2 flux of 0.13 mL min⁻¹ cm⁻² was achieved at 650 °C with (Li-Na-K)₂ CO_3 as the MC phase. However, CO_2 flux decreases with operation temperature above 650 °C, which was suspected to result from the reaction between SS and MC phase in oxidizing atmosphere at high temperatures. LiFeO₂ phase with low conductivity was found on the surface of SS after test hindering the surface reaction, $CO_2 + 1/2O_2 + 2e^- \rightarrow CO_3^{2-}$, thus decreasing the CO_2 flux.

To avoid the chemical compatibility problem between SS and MC, silver (Ag), which shows not only a higher electronic conductivity, but also better stability with MC, has been studied as a porous matrix material by Huang group [50]. A 6-fold higher CO₂ flux than SS-MC membrane, i.e. 0.82 mL min⁻¹ cm⁻², was reached by the Ag-MC membrane at 650 °C with 41.67% CO₂, 41.67% O₂, and 16.66% N₂ as the feed gas and He as the sweep gas. However, as shown in Fig. 5a, CO₂ flux also decays at high temperatures. The cause for the degradation was attributed to the sintering of porous silver matrix as indicated in Fig. 5b and c [51]. Surface modification and microstructural optimization were considered to improve the stability of the Ag-MC membranes, which will be described in detail in later sections.

The silver's coarsening issue is difficult to fix by just surface modification, and the high cost of silver is another concern for practical applications. To solve this cost and sintering issues, Zhang et al. reported NiO as a new matrix material [106]. The long-term $\rm CO_2$ flux and stability of NiO-MC shown in Fig. 5d indicates a "preactivation" period and a high flux >1.0 mL min⁻¹ cm⁻² at 850 °C. The "pre-activation" period was explained by the *in situ* formation of an interfacial phase of $\rm Li_{0.4}Ni_{1.6}O_2$ (LNO) between the NiO matrix and MC phase, as schematically shown in Fig. 5e. LNO has a high electronic conductivity (\sim 200 S cm⁻¹) and can serve as an electron conductor [106].

So far, only few materials have been studied as the matrix material for MECC membranes, due to the stringent requirements such as high electronic conductivity in oxidizing atmosphere, good chemical compatibility and thermal stability with MC at high temperatures. The CO₂ fluxes of the reported MECC membranes are summarized in Table 4, in which the NiO-MC membrane shows the most promising prospects owing to its low cost, good thermal stability and high CO₂ flux.

3.1.4. Mixed ionic-electronic conductors

Perovskite-structured oxides with high mixed electron and oxide-ion conductivity have been successfully

b: prepared by citrate method); BYS: Bi_{1.5}Y_{0.3}Sm_{0.2}O₃.

 $\begin{tabular}{ll} \textbf{Table 3} \\ \textbf{Microstructure and } \textbf{CO}_2 \ permeation \ performance \ of \ different \ MOCC \ membranes. \end{tabular}$

	Matrix pore size/ thickness	Flux (mL min ⁻¹ cm ⁻²)/temperature				
O ²⁻ /CO ₃ ²⁻	(μm)	(°C)	Feed gas/ sweep gas	Stability	Ea (kJ mol ⁻¹)	Ref.
/SZ/ .i-Na-K	0.2-3/250	0.133/750	CO ₂ :He=1:1/ Ar:CO ₂ =99:1	66 h at 750 °C, Stable	84±14	[89]
rsz/	0.05/~10	0.524/650	$CO_2:N_2=1:3/$	20 h at 650 °C, Stable	106	[78]
.i-Na-K /SZ/	0.076/	~0.01/650	He CO ₂ :N ₂ =1:1/	/		[90]
i-K	1 4/	0.033/550	He	1	F0 FC	[10/
/SZ/ .i-Na-K	1-4/ 300 ^(HF)	0.022/550 0.061/650 0.22/950	CO ₂ :N ₂ =1:1/ He	I	50.56	[104
BYS/ .i-Na-K	0.29/~50	0.083/650	CO ₂ :Ar=1:1/ He	70 h at 650 °C, Stable	113.4	[63]
BYS/	1	0.066/650	$CO_2:Ar=1:1/$	/	113.4	[105
.i-Na-K	1	0.000/030	He	1	115.1	[10.
SDCª/ Li-Na-K	3-5/150	1.56/900 0.85/800	CO ₂ :N ₂ =1:1/ He	1	60.3	[97]
CeO ₂ /	/1000	0.0073/650	CO ₂ :He:N ₂ =1:1:3/	80 h at 550 °CWF,	95	[103
Li-K	11000	0.0091/650 ^{WF} 0.021/650 ^{WS}	Ar	Stable	82 ^{WF} <80 ^{WS}	[103
SDC ^a /	/150	0.55/650	CO ₂ :N ₂ =1:1/	160 h at 700°C, Stable		[66]
.i-Na-K SDCª/	0.4/1500	0.88/700 0.69/900	He CO ₂ :N ₂ =1:1/	330 h at 900 °C,	63	[65]
Li-Na-K	0.4/1300	0.43/700(5atm)	He	Stable	03	[05]
SDC ^a /	0.4/1500	0.79/900	CO ₂ :CO:H ₂ :	840 h at 700 °C,	54	[65]
Li-Na-K	0, 1, 1000	0,7 5,75 5 5	N ₂ =7:10:2:1/ He or Ar	Stable	5.	[00]
SDC/	0.55/1200	1.84/700		1	74.3	[49]
.i-Na	, , , , , ,	, , , ,	CO ₂ :H ₂ :N ₂ =10:1:10/He	,		
SDC/	1-2/1180	0.11/700	$CO_2:CH_4:N_2=$	100 h at 650 °C,	48.86	[91]
Li-Na		0.133/650	3:14:2/Ar CO ₂ :CH ₄ :N ₂ = 9:11:4/Ar	Decreased slightly		
SDC/	1-2/1210	0.13/650	3.11.1/111	100 h at 650 °C,	34.72	[61]
Li-Na	,	,	CO ₂ :O ₂ :N ₂ =3:2:15/He	Stable		
SDC/	$1-3/1500^{T}$	0.36/900	WGS/He	120 h at 900 °C ^W ,	90.8	[10
Li-Na-K		~0.50/900	CO:N ₂ =1:1/He	Stable	83.3	
SDC/	0.4/800	0.18/550	$CO_2:H_2:N_2=9:2:9/Ar$	30 h at 750 °C,	65	[99]
Li-Na		0.87/750	200ppm H ₂ S feed	Decreased	1	
		0.50/750				
SDC/	0.4/1000	0.67/750	$CO_2:N_2=1:1/$	12 h at 750 °C,	73.1	[10
Li-Na		0.40/750	Ar	Decreased		
SDC/CS82	0.4/1000	0.62/750	200ppm SO_2 feed $CO_2:N_2=1:1/$	1	74.0	[10
SDC/CS55	0.4/1000	0.43/750	Ar	I	98.0	[100
SDC/CS28		0.12/750	711		105	
SDC/CS20	0.606/120	2.05/900	$CO_2:N_2=1:1/$	22 h at 700 °C,	62.5	[67]
Li-Na-K	/1000	0.6/900	He	Stable in syngas	82.4	[07]
	/1500	0.5/900	Syngas/He	ojguo	80.7	
	/120	1.63/900	J 0 1		61.5	
SDC/	0.4/800	0.86/750	CO ₂ :H ₂ :N ₂ =9:2:9/He	140 h at 750 °C,	64.7	[98]
Li-Na	/650	1.01/750		Decreased in	60.2	
	/100	1.29/750		100 ppm H ₂ S	54.9	
GDC ^a /	0.2-2/300	0.15/850	CO ₂ :He=1:1/	66 h at 750 °C,	77±6	[89]
Li-Na-K			Ar:CO ₂ =99:1	Stable		
GDC ^a /	/920	0.24/650	$CO_2:N_2=1:1/$	1	79	[101
Li-Na		0.5/800 0.61/850	Ar		48	
GDC ^a /	/580	0.133/650	$CO_2:N_2=1:1/$	120 h at 700 °C,	61.9	[103
Li-Na	•	0.301/700	He	Stable		-
GDC ^b /	1-3/830	0.16/650	$CO_2:N_2=1:1/$	1	59.56	[92]
Li-Na		0.62/850	Ar			

Note: YSZ: $Y_{0.16}Zr_{0.84}O_{2-\delta}$; BYS: $Bi_{1.5}Y_{0.3}Sm_{0.2}O_{3-\delta}$ with a pore surface modification film by γ -Al₂O₃; GDC^a: $Ce_{0.9}Gd_{0.1}O_{1.95}$; GDC^b: $Ce_{0.8}Gd_{0.2}O_{1.9}$; SDC: $Ce_{0.8}Sm_{0.2}O_{1.9}$; HF: hollow fiber; T: tube; WF: wet feed gas (\sim 2.5% H_2O); WS: wet sweep gas (\sim 2.5% H_2O) W : syngas-N₂-H₂O; syngas: 49.5% CO, 36% CO₂, 4.5% N₂, 10% H_2 ; Li-Na-K= Li₂CO₃:Na₂CO₃:Ka₂CO₃ with ratio of 42.5:32.5:25 mol%; Li-K= Li₂CO₃:K₂CO₃ with ratio of 62:38 mol%; Li-Na= Li₂CO₃:Na₂CO₃ with ratio of 52:48 mol%; CS82=Li-Na:Na₂SO₄ with ratio of 80:20 mol%; CS55=Li-Na:Na₂SO₄ with ratio of 50:50 mol%; CS28=Li-Na:Na₂SO₄ with ratio of 20:80 mol%;

employed as oxygen transport membranes (OTMs) [110-113]. Thus, some of these mixed ionic-electronic conductors (MIECs), e.g. La $_{0.6}$ Sr $_{0.4}$ Co $_{0.8}$ Fe $_{0.2}$ O $_{3-\delta}$ (LSCF) [53,62], La $_{0.5}$ Sr $_{0.5}$ Fe $_{0.8}$ Cu $_{0.2}$ O $_{3-\delta}$ (LSFCu) [54], SrFe $_{0.8}$ Nb $_{0.2}$ O $_{3-\delta}$ (SFN) [79], and La $_{0.85}$ Ce $_{0.1}$ Ga $_{0.3}$ Fe $_{0.65}$ Al $_{0.05}$ O $_{3-\delta}$ (LCGFA) [64] and so on, have

been used as porous matrices for CO_2TMs . LSCF with a high electronic and ionic conductivity was first reported as a MIEC matrix for CO_2TM [53]. As described in the mechanisms section, see Fig. 2c, MEOCC membranes could be used under two different conditions: with and without O_2 feed. In the case of no O_2 feed,

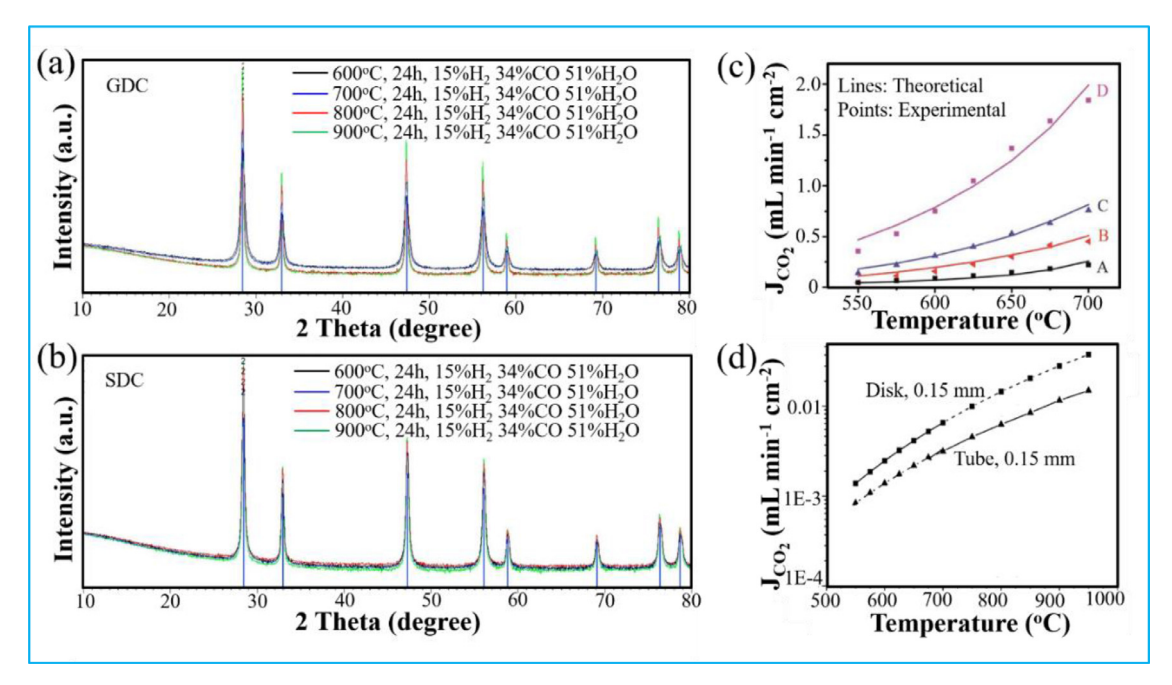


Fig. 4. XRD patterns of GDC (a) and SDC (b), respectively, after exposure in syngas composed of 15% H_2 , 34% CO and 51% H_2 O at 600-900 °C for 24 h. Adapted from ref. [96] with permission from Elsevier, 2019. (c) Comparison of the measured CO_2 flux with theoretical calculations using the existing flux transport model. MOCC-A: 70 vol% SDC-30 vol% MC; B: 65 vol% SDC-35 vol% MC; C: 60 vol% SDC-40 vol% MC; D: 50 vol% SDC-50 vol% MC. MC: Li_2CO_3 :Na $_2CO_3$ = 53:48 mol%. Reproduced from ref. [49] with permission from Royal Society of Chemistry, 2012. (d) Comparison of CO_2 permeation fluxes for tube and disk SDC-MC membranes as a function of temperature. Data in solid lines are reported or measured values, while points in dashed lines are estimated from reported activation energies. Adapted from ref. [66] with permission from American Chemical Society, 2014.

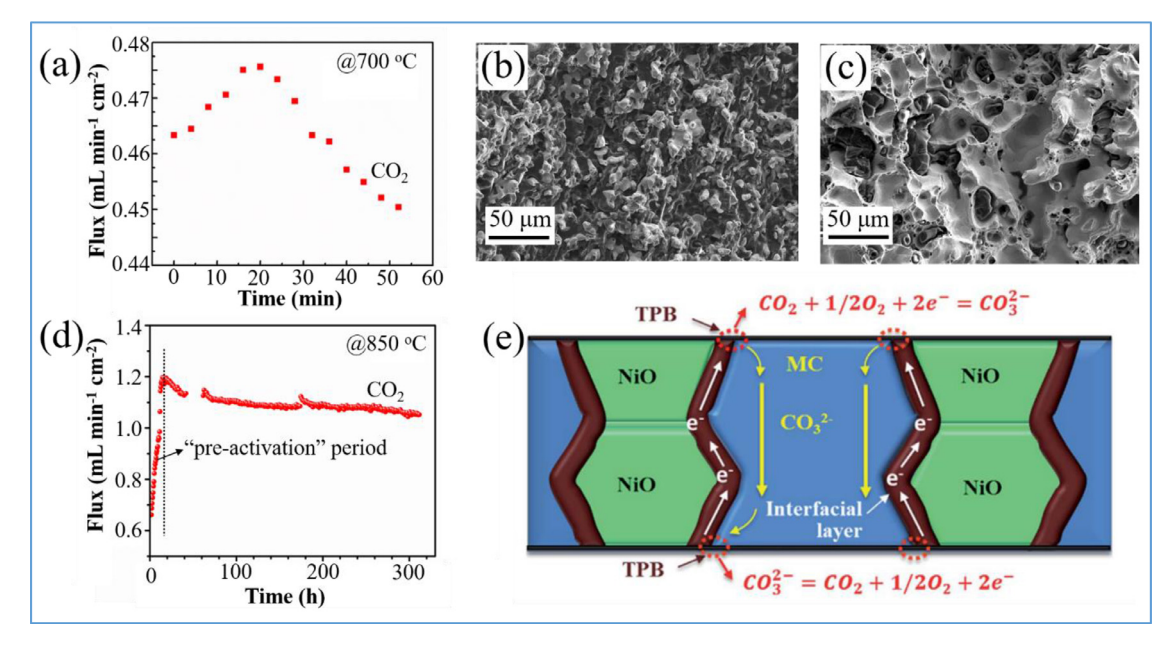


Fig. 5. (a) CO₂ flux stability of the Ag-MC membrane at 700 °C; (b) and (c) microstructures of Ag-MC membranes before and after the stability test, respectively. Reproduced from ref. [51] with permission from Royal Society of Chemistry, 2016. (d) The CO₂ flux of the NiO-MC membrane measured at 850 °C; (e) a schematic illustration of the self-forming MECC membrane. Adapted from ref. [106] with permission from Royal Society of Chemistry, 2017.

the maximum CO_2 flux of 0.3 mL min⁻¹ cm⁻² was obtained at 900 °C for a 375- μ m-thick membrane, in which a CO_2 -Ar mixture gas (50:50 mol%) was used as the feed gas and He as the sweep gas [53]. However, the stability of LSCF-MC membrane is poor, showing a fast decay in CO_2 flux in an O_2 -free atmosphere, see Fig. 6a. The degradation was attributed to the reaction between LSCF and CO_2 on the membrane surface, resulting in the formation of a strontium carbonate layer which inhibits the surface reaction, see Fig. 6b [62]. One way to circumvent this problem is to co-feed

 O_2 with CO_2 , because in the presence of O_2 , $SrCO_3$ decomposed into SrO at temperature higher than 800 °C [114], which will lead to the preservation of the perovskite structure, as observed in LSCF as OTM [115]. A maximum CO_2 flux of 3.0 mL min⁻¹ cm⁻² was achieved at 900 °C with $CO_2-O_2-N_2$ as the feed gas. The significant increase in CO_2 flux is attributed to the change of CO_2 transport mechanism, *i.e.* CO_3^{2-} bulk diffusion becomes the limiting step since the CO_3^{2-} conductivity (\sim 3.5 S cm⁻¹) of the MC phase is much lower than LSCF electronic conductivity (\sim 1000 S cm⁻¹ at

Table 4Comparison of CO₂ flux and stability of different MECC membranes.

e-/CO ₃ 2-	Matrix pore size/ thickness (μ m)	Flux (mL min ⁻¹ cm ⁻²)/ temperature (°C)	Feed gas/ sweep gas	Stability	Ea (kJ mol ⁻¹)	Ref.
SS/Li-Na-K	5-10/1570	0.13/650	CO ₂ :O ₂ =2:1/ vacuum	1	31.3	[68]
Ag/Li-K	~10/1670	0.82/650	CO ₂ :O ₂ :N ₂ =5:5:2/He	80 h at 650 °C, Decreased slightly	65.6	[49]
Aga/Li-K	~8/630	0.61/600	CO ₂ :O ₂ :N ₂ =5:5:2/He	326 h at 600 °C, Decreased	1	[69]
	/840	0.61/600		after 150 h		
	/1140	0.32/600				
	/1210	0.28/600				
	/1450	0.23/600				
Aga/Li-K	15-20/1230	0.39/650	CO ₂ :O ₂ :N ₂ =5:5:2/He	130 h at 650 °C, Stable	81.0	[107]
Agb/Li-Na	~10/800	0.25/650	CO ₂ :O ₂ :N ₂ =3:2:15/He	100 h at 650 °C, Stable	35	[108]
Agc/Li-Na	~10/800	0.71/650	CO ₂ :O ₂ :N ₂ =21:21:8/He	100 h at 650 °C, Decreased	68	[80]
Ag ^d /Li-Na	5-10/	0.43/650 0.9/850	CO ₂ :O ₂ :N ₂ =3:2:15/Ar	\sim 40 h at 800 °C, Decreased	60.1	[51]
Ag/Li-Na	~1/960	1.02/650	CO ₂ :O ₂ :N ₂ =3:2:15/ 9.41%H ₂ -Ar	900 h at 600 °C, Decreased after 700 h	44.6	[109]
Ag/Li-Na	0.2-1/910	0.89/650	CO ₂ :O ₂ :N ₂ =3:2:15/ 9.41%H ₂ -Ar	${\sim}500~h$ at 600 °C, Stable	48.57	[52]
NiO/Li-Na	/1200	1.0/850	CO ₂ :O ₂ :N ₂ =3:2:15/Ar	320 h at 850 °C, Stable	73.3	[106]

Note: SS: Stainless-steel; Ag^a : Ag pore surface coated with 5 wt% Al_2O_3 colloidal solution; Ag^b : Ag pore surface coated with Al_2O_3 by CVD (chemical vapor deposition); Ag^c : Ag pore surface coated with Al_2O_3 by ALD (atomic layer deposition); Ag^d : Ag pore surface coated with ZrO_2 by ALD (atomic layer deposition).

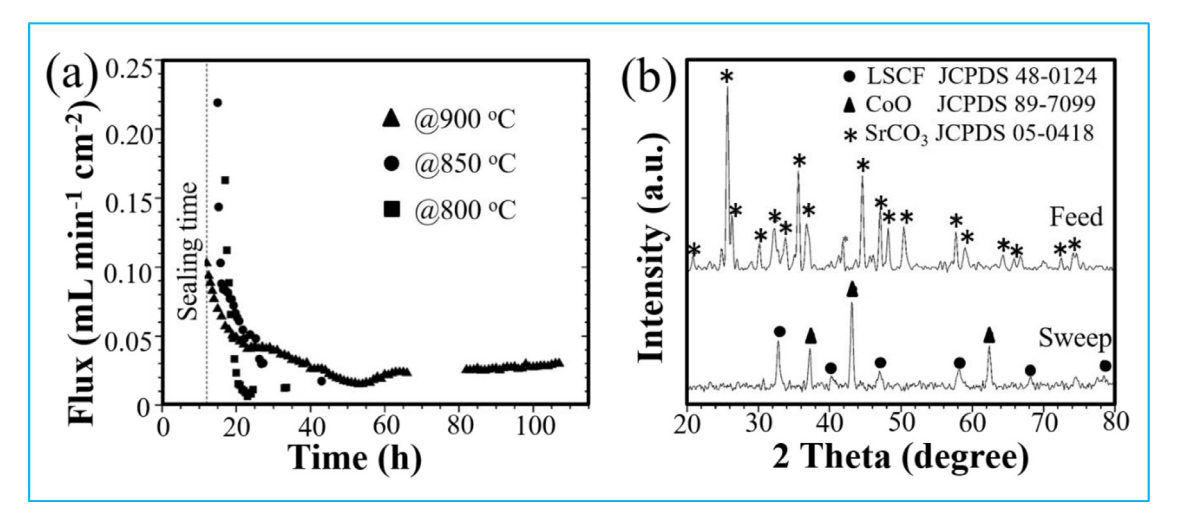


Fig. 6. (a) Time-dependent CO_2 fluxes of LSCF-MC membrane measured at different temperatures (thickness = 1.0 mm, 1 atm, feed gas is equimolar CO_2/N_2 , sweep gas is pure Ar, feed and sweep flow rate = 100 mL min⁻¹); (b) XRD patterns of LSCF-MC samples exposed to a mixture of CO_2 and N_2 in a temperatures range of 850 to 950 °C for 110 h. Reproduced from ref. [62] with permission from American Chemical Society, 2014.

900 °C). However, low oxide-ion conductivity (\sim 0.1 S cm $^{-1}$) of LSCF is the performance limiting factor when there is no O $_2$ -fed. The two different CO $_2$ permeation mechanisms are supported by different activation energies of CO $_2$ permeation under the two different feed-gas conditions. No significant degradation was observed during the 600-h stability test on LSCF-MC membrane at 850-950 °C with CO $_2$ -O $_2$ -N $_2$ as the feed gas and Ar as the sweep gas [62].

An LSFCu perovskite was tried as a solid matrix for MEOCC membranes. A CO_2 flux of 0.15 mL min $^{-1}$ cm $^{-2}$ was obtained at 650 °C at a membrane thickness of 1.5 mm and with CO_2 - N_2 (50–50 mol%) feed gas and He sweep gas [54]. However, a slight running away of MC from the MEOCC membrane was observed due to the poor wettability of MC to LSFCu matrix. In addition, ceramic materials containing alkaline-earth elements are prone to react with CO_2 at high temperatures, forming carbonates [116,117].

A-site alkaline-earth free perovskite oxides were previously suggested to show a better resistance to CO_2 attack. An alkaline-earth metal free and A-site deficient perovskite ceramic material with a composition of $La_{0.85}Ce_{0.1}Ga_{0.3}Fe_{0.65}Al_{0.05}O_{3-\delta}$ (LCGFA) was, there-

fore, investigated as a matrix for MEOCC membranes [64]. This study showed that LCGFA exposed to various atmospheres (e.g. CO_2 , N_2 , syngas, etc.) is chemically compatible with MC and CO_2 under operating conditions. A 275-h stability test using $50\%CO_2$ - N_2 feed gas at 900 °C and a 1.5-mm-thick membrane indicates that CO_2 flux increases slightly with time from 0.021 to 0.025 mL cm⁻² min⁻¹. However, CEO_2 peaks in the post-tested sample became more pronounced compared to the fresh one, suggesting the decomposition of LCGFA. In addition, the CO_2 flux is much lower than the reported LSCF-MC membrane, largely due to the lower oxide-ion conductivity of LCGFA (0.03 S cm⁻¹ at 900 °C) than LSCF (0.1 S cm⁻¹ at 900 °C).

 $\rm SrFe_{0.8}Nb_{0.2}O_{3-\delta}$ (SFN) was reported to show a better chemical compatibility in $\rm CO_2$ atmosphere and with MC phase under operating conditions [79]. A multichannel SFN-MC hollow fiber membrane was fabricated and evaluated for $\rm CO_2$ permeation, a schematic of which is shown in Fig. 7a. A 200-h stability test showed a stable $\rm CO_2$ flux of 0.31 mL min⁻¹ cm⁻² at 700 °C with $\rm CO_2$ -N₂ feed gas and He sweep gas. In addition, it was shown that the SFN-MC membrane exhibits a good thermal cycling stability

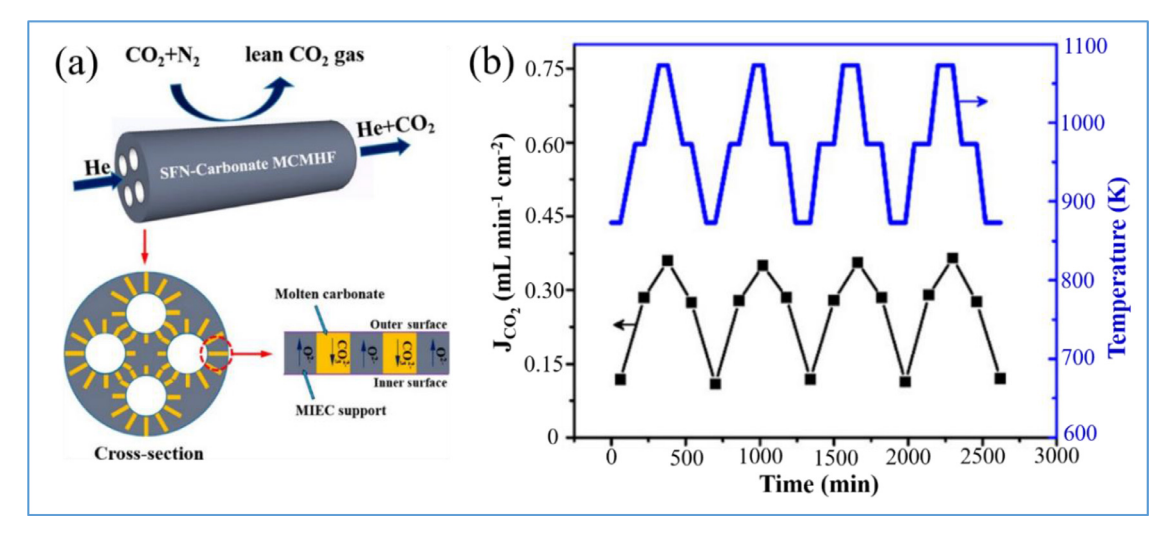


Fig. 7. (a) Schematic configuration of an asymmetric SFN-carbonate MCMHF (MCMHF: mixed-conducting multichannel hollow fiber) membrane and ionic transport and CO_2 permeation through the membrane; (b) thermal cycling stability of the SFN-MC membrane between 600 and 800 °C (feed side: CO_2 flow rate of 50 mL min⁻¹ and N_2 flow rate of 50 mL min⁻¹; sweep side: He flow rate of 100 mL min⁻¹). Reproduced from ref. [79] with permission from American Chemical Society, 2016.

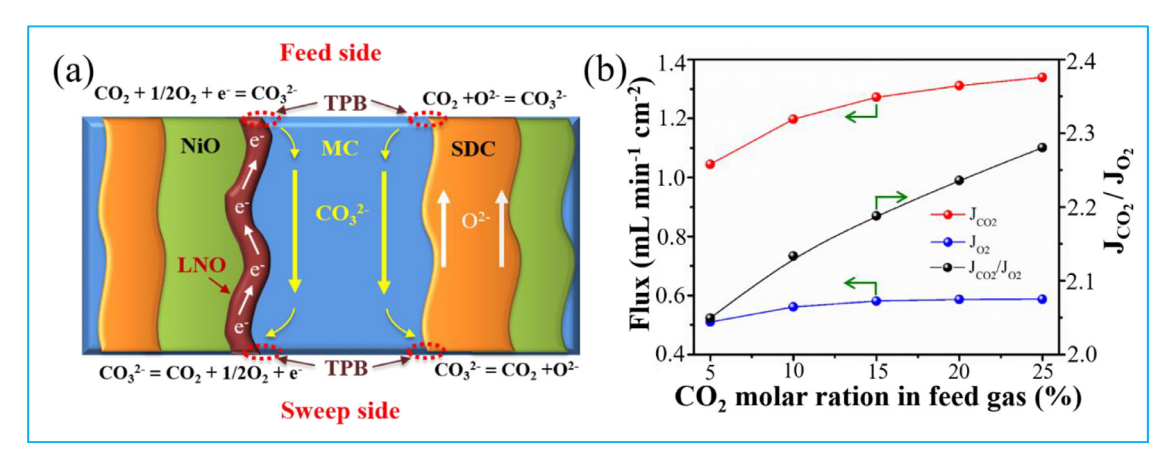


Fig. 8. (a) A schematic illustration of CO_2 and O_2 transport mechanisms of the NiO-SDC-MC membrane; (b) CO_2 and O_2 fluxes of a NiO-SDC-MC membrane vs CO_2 concentration in the feed gas at 850 °C. CO_2 concentration is kept at 10%, and CO_2 is used as the balance gas. Reproduced from ref. [55] with permission from American Chemical Society, 2018.

between 600 and 800 $^{\circ}$ C, see Fig. 7b. No compositional change in the post-test samples was observed, suggesting a good stability of the membrane.

In addition to the single-phase mixed conductor matrix materials, dual-phase porous matrices have also been developed for MEOCC membranes. $Ce_{0.85}Sm_{0.15}O_{2-\delta}-Sm_{0.6}Sr_{0.4}Al_{0.3}Fe_{0.7}O_{3-\delta}$ (SDC-SSAF) was previously used as an OTM material, exhibiting high oxygen permeation flux and good stability under a CO2 containing atmosphere [118]. Thus, it was used as a matrix material for MEOCC membranes. A similar phenomenon of CO2 flux enhancement by the presence of O_2 in the feed-gas was observed [56]. NiO-SDC is another sample of composite porous matrix for MEOCC membranes [55]. The highly electronic conducting phase, LNO, is formed in situ between MC and NiO during high temperature operation and serves as the electron conducting phase, see Fig. 8a, while SDC serves as the O2- conducting phase, making the membrane simultaneously transport e^- , O^{2-} , and $CO_3{}^{2-}$. Such a triple conduction mechanism is supported by the permeated CO_2 to O_2 flux ratio, see Fig. 8b. The CO2 flux increases from 1.04 to 1.34 mL min⁻¹ cm⁻² as CO₂ concentration increases from 5 to 25%, while the O2 flux was enhanced slightly from 0.51 to 0.56 mL min⁻¹ cm⁻² by increasing CO₂ concentration from 5% to 10%, then followed by a plateau. The maximum CO2 flux reaches 1.17 mL $\mathrm{min^{-1}~cm^{-2}}$ at 850 °C through a NiO-SDC-MC 1.2-mm-thick membrane. A 200-h flux stability test at 850 $^{\circ}\text{C}$ shows no sign of degradation.

CO₂ permeation performances through different MEOCC membranes are summarized in Table 5. Compared to Table 3 and 4, MEOCC membranes exhibit higher CO₂ fluxes than MOCC and MECC counterparts. However, O₂ in the feed-side is essential for achieving a high flux, yielding a mixture of O₂ and CO₂ in the sweep-side. Further O₂-separation process, such as using OTMs, is needed to obtain a pure stream of CO₂ for storage. But for combined CO₂ capture and conversion, the concomitant O₂ permeation is in fact beneficial to minimize coking in membrane reactor based dry-oxy methane reforming to produce syngas and oxidative dehydrogenation of ethane (ODHE) to produce ethylene [55,119,120].

3.2. Microstructure of solid matrix

The porous solid matrix in CO_2TMs serves for two purposes: conducting oxide-ion/electron and immobilizing MC phase. Therefore, its microstructural features such as porosity, tortuosity, triple-phase boundary density and pore size/distribution play a crucial role in flux performance and long-term stability. For MOCC membranes, CO_2 transport is governed by Eq. (2), in which permeation flux is a function of microstructural parameters (porosity ε , MC volume ratio φ , and tortuosity τ). On the other hand, the total

Table 5 CO₂ flux and stability of MEOCC membranes.

O ²⁻ +e ⁻ /CO ₃ ²⁻	Matrix pore size/ thickness (μm)/	Flux density (mL min ⁻¹ cm ⁻²)/ temperature (°C)	Feed gas/ sweep gas	Stability	Ea (kJ mol ⁻¹)	Ref.
LSCF/ Li-Na-K	0.18/375 /750 /1500 /3000	0.32/900 0.31/900 0.25/900 0.14/900	CO ₂ :Ar=1:1/ He	1	89.9 89.6 87.7 86.4	[53]
LSCF/ Li-Na-K	0.432/1200 0.587/1200 0.804/1200 0.778/1200	0.20/900 0.41/900 0.32/900 0.13/900	CO ₂ :N ₂ =1:1/ He	1	127-147	[121]
LSCFu/ Li-Na*	/1500	0.15/650 0.18/650# 0.35/750 0.55/750# 1.55/750#	CO ₂ :N ₂ =1:1/ He CO ₂ :O ₂ =1:4/He	1	46.3 74.3 [#]	[54]
LCGFA/Li-Na-K	/750 /1500	0.044/900 0.024/900	CO ₂ :N ₂ =1:1/ Ar	275 h at 900 °C, Stable	96	[64]
LSCF/Li-Na-K	/1000	0.02/700 0.051/900 2.0/850 3.0/900	CO ₂ :N ₂ =1:1/ Ar CO ₂ :O ₂ :N ₂ =2:1:1/Ar	110 h at 900 °C, Decreased 600 h at 850-950 °C, Stable	144 108	[62]
LSCFHF/Li-Na-K	/400	0.061/500 1.0/900	CO ₂ :N ₂ =1:1/ He	1	56.8	[71]
SFNMHF/Li-Na-K	1-5/220	0.31/700 0.64/850	CO ₂ :N ₂ =1:1/ He	200 h at 700 °C, Stable	44.8	[79]
NiO-SDC/Li-Na	1/~1200	0.18/650 1.17/850	$CO_2:O_2:N_2=3:2:15/Ar$	200 h at 850 °C, Stable	80.4	[55]
SDC-SSAF/Li-Na-K	-/1300	0.24/900 0.28/900	CO ₂ :He:N ₂ =3:3:14/N ₂ CO ₂ :O ₂ :He=15:6:15:64/N ₂	1	160.7 110.6	[56]
SDC-SSAF/Li-Na-K	0.1-1/900	0.24/900 0.12/900 ^{AP} 0.28/900 0.35/900 ^{AP}	CO ₂ :He:N ₂ =3:3:14/N ₂ CO ₂ :O ₂ :He=15:6:15:64/N ₂	1	110.2 110.6 ^{AP}	[122]
CP-PSFC/Li-Na-K	1	0.62/875	CO ₂ :O ₂ :N ₂ = 15:17:68/Ar	160 h at 850 °C, Stable	61.7	[57]

Note: Li-Na*: Li₂CO₃-Na₂CO₃=53-47 mol%; Li-Na: Li₂CO₃-Na₂CO₃=52-48 mol%; Li-Na-K: Li₂CO₃-Na₂CO₃-K₂CO₃=42.5-32.5-25 mol%; LSCF: La_{0.6}Sr_{0.4}Co_{0.8}Fe_{0.2}O_{3..\delta}; LSFCu: La_{0.5}Sr_{0.5}Fe_{0.8}Cu_{0.2}O_{3..\delta}

effective conductivity σ_t should be corrected by the microstructural parameters using the following equation to connect with the intrinsic conductivities $(\sigma_{CO_3^{2-}}, \sigma_{O^{2-}})$ of ceramic and carbonate phases

$$\sigma_{t} = \frac{\left(\frac{\varepsilon}{\tau}\sigma_{CO_{3}^{2-}}\right)\left(\frac{1-\varepsilon}{\tau}\sigma_{O^{2-}}\right)}{\left(\frac{\varepsilon}{\tau}\sigma_{CO_{3}^{2-}}\right) + \left(\frac{1-\varepsilon}{\tau}\sigma_{O^{2-}}\right)}$$
(19)

For most of MOCC membranes, oxide-ion conductivity of the ceramic phase is much lower than carbonate-ion conductivity of the carbonate phase. Thus, oxide-ion transport normally limits CO₂ permeation flux. However, to be exact, the relative values of effective conductivities for carbonate and ceramic phases, i.e. $(\frac{\varepsilon}{\tau})\sigma_{CO_c^{2-}}$ and $(\frac{1-\varepsilon}{\tau})\sigma_{0^{2-}}$, determine the final CO₂ flux. For example, an LSCF matrix sintered at 1050 °C with an ε/τ =0.0415 and 0.59 for carbonate and ceramic phases, respectively, was reported to yield a similar effective conductivity for MC (Li-Na-K2CO3) and LSCF phases [121]. The same study also shows that the CO₂ flux of LSCF-MC membrane is increased by 3 times by decreasing the LSCFmatrix sintering temperature from 1100 to 1000 °C, demonstrating the significant effect by the microstructure. In studying the microstructural effect on CO2 flux, Zhang et al. prepared a series of interconnected three-dimensional SDC matrix, see Fig. 9a and 9b, with a range of ε/τ and porosity [49]. The results show that the CO₂ flux at 700 °C is increased from 0.26 to 1.84 mL min⁻¹ cm⁻²

as the SDC porosity is increased from 30 to 50%, while ε/τ is increased from 0.0123 to 0.234.

For dual-phase membranes, the amount of each phase needs to be enough to form continuity in the bulk so that both phases exceed the percolation threshold for transport, i.e. ≥30% vol. for the minor phase [123]. Thus, the porosity ε (or solid fraction, 1- ε) shows insignificant difference in these porous solids, the tortuosity (τ) vary in a wide range. For example, the tortuosity of a porous SDC matrix is shown to decrease from 26.1 to 2.27 as the porosity increases from 30 to 50% [49], a trend that was also confirmed by the LSCF matrix [121], in which a decrease in tortuosity from 17.69 to 2.56 is observed as the porosity is increased by decreasing the sintering temperature from 1100 to 1000 °C. In addition, it was reported that the disk-type membrane shows a higher CO₂ flux than the tubular one even with the same thickness [67]. The authors attributed it to a better microstructure (the better connections of the particles in the disk than that in the tube) of the ceramic phase in disk-shaped membranes [67]. Therefore, how to optimize the tortuosity of the solid matrix is of criticality to maximizing CO2 flux of MOCC membranes.

Pore size is another important parameter to ensure high CO_2 flux and long-term stability for CO_2 TMs. On one hand, the capillary forces of a matrix to withhold MC phase is highly dependent on pore size according to the Laplace equation:

$$\Delta p = p' - p'' = \frac{2\gamma\cos\theta}{r} \tag{20}$$

^{#:} LSFCu/Li-Na/LiAlO₂=48/43/9 wt%; LCGFA: La_{0.85}Ce_{0.1}Ga_{0.3}Fe_{0.65}Al_{0.05}O_{3-δ}; SFN: SrFe_{0.8}Nb_{0.2}O_{3-δ}

 $^{^{\}rm HF}$: hollow fibre

MHF: multichannel hollow fiber

 $^{^{}AP}: feed \ side \ surface \ modification \ by \ Au-Pd \ (46/54 \ at\%); \ CP-PSFC: \ Ce_{0.9}Pr_{0.1}O_{2-\delta}-Pr_{0.6}Sr_{0.4}Fe_{0.5}Co_{0.5}O_{3-\delta} \ (40-60 \ wt\%).$

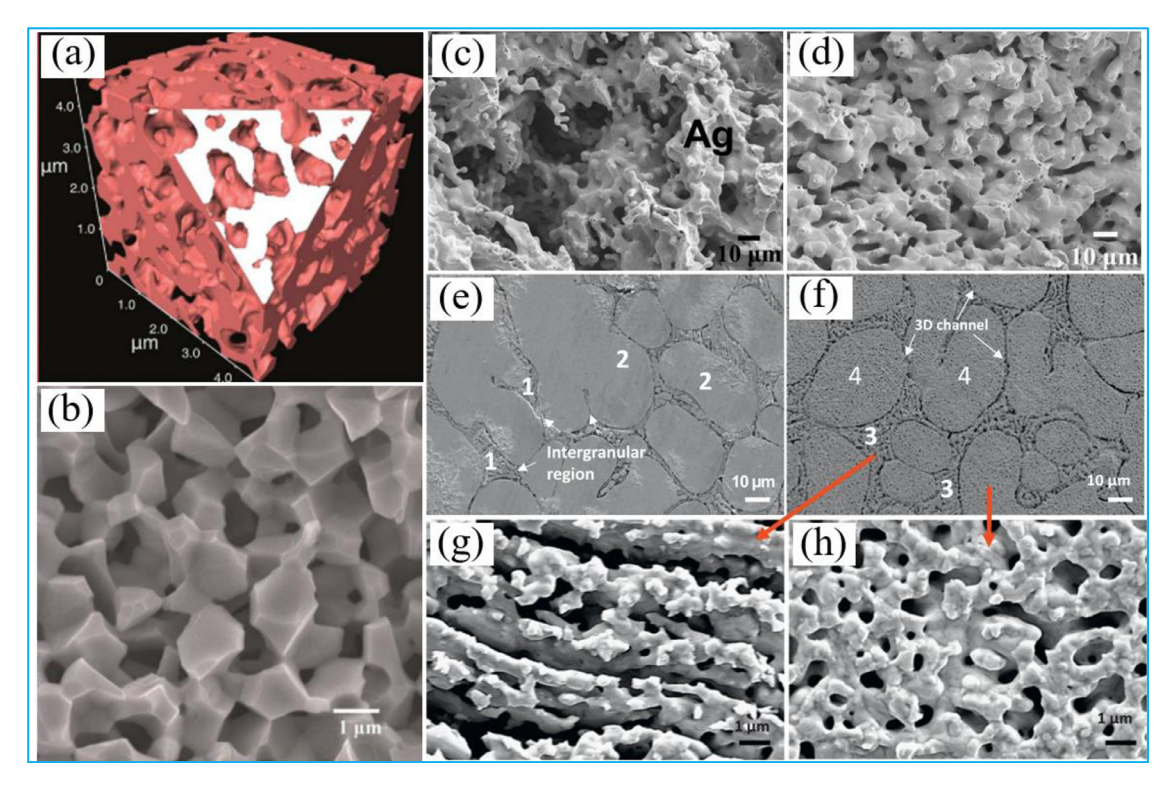


Fig. 9. (a-b) Microstructural features of an SDC matrix with 50% porosity: a) reconstructed 3D microstructure; b) SEM 2D microstructure. Reproduced from ref. [49] with permission from Royal Society of Chemistry, 2012. (c-h) SEM images of porous Ag matrix created by: c) microcrystalline methylcellulose; d) carbon black; chemical dealloying from: e) Ag50Al50 (leached in 3 M HCl at 90 °C for 3 min); f) for 48 h; g) high magnification of location 3; h) high magnification of location 4. Reproduced from refs. [69,107,109] with permission from Elsevier, 2014, 2016, 2017.

where γ , θ , and r are MC surface tension, contact angle between solid matrix and MC, and pore radius of solid matrix, respectively; p' and p'' are external and internal pressures across pore, respectively. Too large a pore would not generate enough capillary forces to withhold MC phase, thus leading to a loss of MC and degradation of flux. On the other hand, large pores in solid matrix also lead to a low density of triple phase boundaries (TPBs), resulting in low flux density. Thus, decreasing pore size of the solid matrix is needed to enhance both flux and long-term stability of CO_2TMs .

The effect of Ag-matrix pore size in Ag-MC membranes on permeation performance was studied by varying pore formers with different pore sizes, *e.g.* microcrystalline methylcellulose (15-20 μ m) vs. carbon black (10 μ m) [69,107]. The microstructures of these silver matrices are compared in Fig. 9c and 9d. The flux results show a roughly 1.5 times improvement in CO₂ flux at 500-650 °C, *e.g.* from 0.24 to 0.37 mL min⁻¹ cm⁻² at 600 °C, by switching pore formers from microcrystalline methylcellulose to carbon black. The chemical/electrochemical dealloying technology, a well-established method to produce nanoporous metal structures for various applications [124], was used to decrease the pore size and promote uniform pore distribution of Ag matrix. As shown in Fig. 9e-9h, the microstructures of such prepared Ag matrix (with an average pore size of 1-5 μ m) have led to a CO₂ flux as high as 0.52 mL min⁻¹ cm⁻² at 600 °C [52,109].

The pore size was also found to influence the stability of ${\rm CO_2TMs}$. For example, a very fast degradation of ${\rm CO_2}$ flux at 650 °C after 20 h on-stream was observed on an Ag-MC membrane comprising of an Ag matrix with 15-20 μ m pore size [107]. With the pore size decreasing to 10 μ m, the degradation started after 160 h on-stream at 600 °C [69] and after 30 h at 650 °C [50]. However, with pore size of 1-5 μ m, no obviously degradation was observed during a 220-h testing at 600 °C with Ar sweep gas [109] and a 500-h testing at 600 °C with 9.44% H₂-Ar sweep gas [52]. The main

mechanism for CO_2TMs degradation is the loss of MC during test, which is likely related to the sintering of Ag grains at high temperatures. As the loss of MC continues and accumulates, the gas tightness of membrane and continuity of MC phase will be compromised [69].

3.3. Membrane thickness effect

From a membrane transport perspective, the flux of an active species through a membrane is controlled by both surface reaction and bulk diffusion. Zhu et al. [75,76] modeled the two processes in series with a resistors equivalent circuit model, see Eqs. (10)-(14). The relevant importance of each process to the overall flux is determined by the "Critical Thickness", which is the ratio between bulk diffusivity (cm²/s) and surface exchange rate (cm/s) of the active species. A general rule is that the thinner the membrane, the more control of surface exchange, and the faster the surface exchange rate the thinner the membrane can be with bulk diffusion control. Therefore, a greater Critical Thickness may be expected for CO_2TMs than for proton and oxygen transport membranes due to the slower surface exchange rate of CO_2 .

A critical thickness of 0.84 mm was reported for an Ag-MC membrane [69], which means that a further decrease in thickness below 0.84 mm would not significantly improve CO₂ flux. Under this condition, one should improve the surface exchange rate by applying catalyst or changing operating conditions or optimizing microstructure to favor surface reaction. The surface control was also confirmed by Dong et al. [97], in which the CO₂ flux of SDC-Li/Na/K₂CO₃ membrane was compared in a thickness range of 0.15 and 1.5 mm. It was found that the 0.15-mm-thick membrane exhibited only 3 times higher CO₂ flux than the 1.5-mm-thick one, but not 10 times as expected from the bulk-control flux equation, due to the involvement of surface exchange reaction in the overall CO₂ permeation process [97].

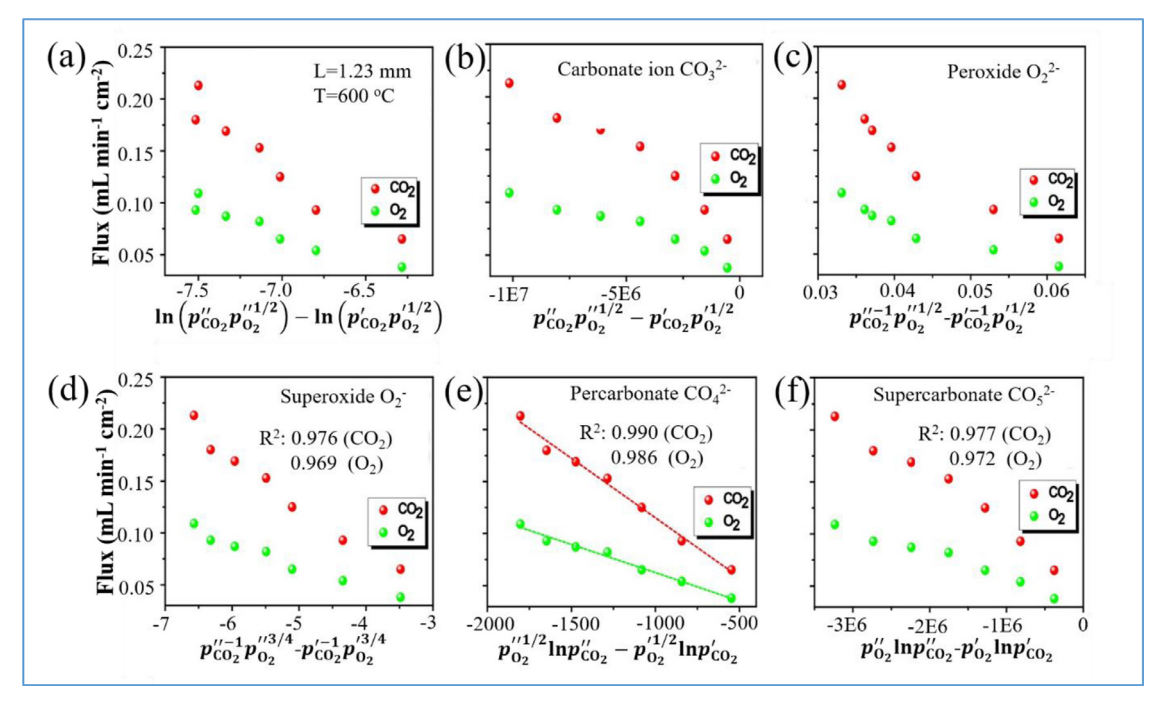


Fig. 10. CO_2/O_2 fluxes of Ag-MC membrane vs. (a) J_{CO2} vs $\ln(p_{CO_2}''p_{O_2}''^{1/2}) - \ln(p_{CO_2}'p_{O_2}'^{1/2})$; (b) J_{CO2} vs $p_{CO_2}''p_{O_2}'^{1/2} - p_{CO_2}'p_{O_2}'^{1/2}$; (c) J_{CO2} vs $p_{CO_2}''p_{O_2}'^{1/2} - p_{CO_2}'p_{O_2}'^{1/2}$; (d) J_{CO2} vs $p_{CO_2}''p_{O_2}''$

Despite the fact of surface CO₂ exchange control, there are still many efforts to develop thin-film membrane for enhanced performance. Lu et al. [78] prepared an asymmetrical MOCC membrane with a thin, small pore (40% porosity, $0.05\mu m$ in diameter), 10- μ m-thick YSZ layer on a thick, large pore (30-40% porosity, 0.2 μ m in diameter) MC-non-wettable BYS support. A CO₂ flux of 0.524 mL min⁻¹ cm⁻² was achieved at 650 °C, which is roughly 10 times higher than the 200-400 μm thick membrane. But the increase of CO2 flux is far less than the expected 20-40 times, suggesting the limitation from surface exchange. Another evidence of the surface exchange limitation is the activation energy of CO₂ permeation process through a thinner YSZ-MC membrane, 106 kJ mol⁻¹ vs. ~84 kJ mol-1 for a thicker counterpart. This trending is understandable because the overall CO2 permeation through a MOCC membrane is controlled by both surface reaction and bulk diffusion, and the activation energy for surface reaction is generally higher than that of bulk diffusion process [53,78]. For a thicker membrane, the CO2 permeation is mainly limited by the bulk diffusion process, thus exhibiting a lower activation energy than the thinner membrane where surface reaction dominates. The critical thickness of the YSZ-MC membrane was suggested to be $> 10 \mu m$, larger than YSZ-based oxygen permeation membranes ($< 10 \mu m$) [125]. The presence of MC and/or different surface morphologies may be the underlying causes.

3.4. Feed gas concentration effect

3.4.1. CO₂ partial pressure

From the CO_2 flux equation of Eqs. (2)-(9), CO_2 partial pressure gradient across CO_2TMs is the major driving force for the CO_2 transport. Thus, the higher the CO_2 partial pressure gradient, the higher the CO_2 flux, which has been confirmed by many studies [61,65,66,69,91]. Increasing CO_2 partial pressure under ambient as well as pressurized conditions increases CO_2 flux. For example, for a 1.5-mm-thick SDC-MC membrane operated at 900 °C, CO_2 flux increases from 0.39 to 0.79 mL min⁻¹ cm⁻² as the feed-side CO_2 partial pressure is increased from 0.1 to 0.9 atm. The flux is also

increased from 0.17 to 0.43 mL min $^{-1}$ cm $^{-2}$ as the total pressure at the feed side is increased from 1 to 5 atm (with a fixed 50 vol% CO $_2$ concentration) at 700 °C [65].

Varying CO_2 partial pressure across the membrane has also been used to understand the CO_2 permeation mechanisms. The relationship between CO_2 flux and CO_2 partial pressure gradient in Ag-MC membranes were studied by hypothesizing various active species, such as CO_3^{2-} , O_2^{-} , O_2^{2-} , CO_4^{2-} and CO_5^{2-} [60], see Fig. 10. The study reveals that the modeling results based on CO_4^{2-} active species agree the best with experimental data.

In the Ag-MC membrane, CO_4^{2-} is formed as an intermediate through the surface reaction $1/2O_2 + CO_3^{2-} = CO_4^{2-}$. The formed CO_4^{2-} then migrates through MC via a cooperative "cogwheel" mode, see Fig. 11(a), to the Ag surface, where it is reduced by electrons to CO_3^{2-} and (O^-) (a transient oxygen species) by $CO_4^{2-} + e^- = CO_3^{2-} + (O^-)$. The produced transient species (O^-) is further reduced by electrons at Ag/MC interface to form O^{2-} via $(O^-) + e^- = O^{2-}$, which readily reacts with CO_2 to form CO_3^{2-} via $O^{2-} + CO_2 = CO_3^{2-}$. The schematic of such a charge-transfer model for MECC membrane is shown in Fig. 3b. The stability of CO_4^{2-} in MC exposed to an oxidizing atmosphere has been experimentally confirmed by Raman spectroscopy [80, 126].

Using MOCC membranes, Tong et al. [91] experimented the feasibility of separating CO_2 from a mixture of CO_2 - CH_4 , intended for applications in purification of biogas or shale gas. The relationship between CO_2 flux and logarithm of CO_2 partial pressure is shown in Fig. 11(b). A linear relationship is observed, suggesting that the modified Eq. (3) previously established for bulk CO_2 transport could also be applied to CO_2 capture from CO_2 - CH_4 mixtures.

3.4.2. H₂ partial pressure

Another way to enhance CO_2 flux of membranes is to decrease the partial pressure of oxygen at the sweep or feed side. For MOCC membranes, it can be done by adding H_2 into the feed-side gas. Since O^{2-} is transported from the sweep side to feed side, the presence of H_2 at the feed-side creates a low oxygen partial pressure environment, thus promoting oxide-ion flux and subsequently

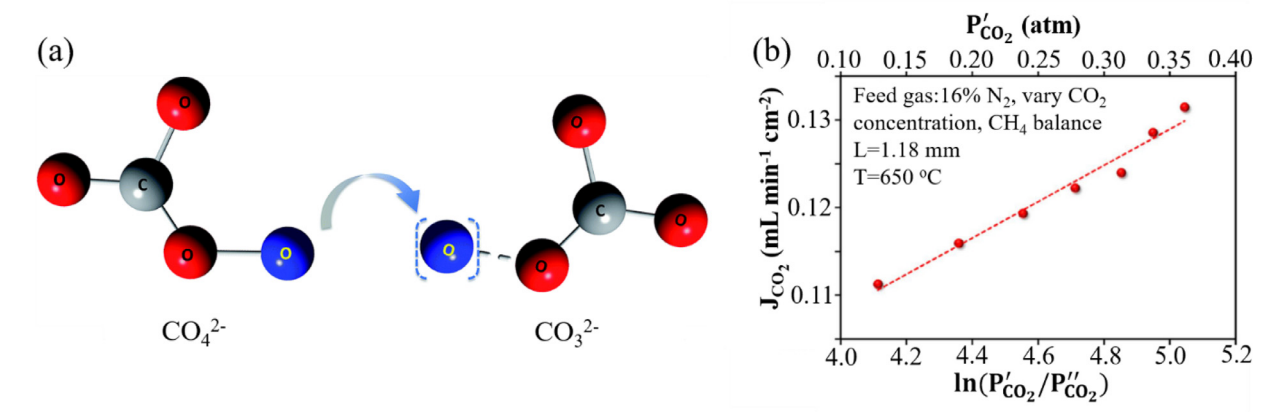


Fig. 11. (a) A schematic of the cooperative "cogwheel" model for CO_4^{2-} transport in an Ag-MC membrane. Reproduced from ref. [80] with permission from Royal Society of Chemistry, 2016. (b) CO_2 flux as function of logarithm of CO_2 partial pressure using a MOCC membrane. Reproduced from ref. [91] with permission from The Electrochemical Society. 2015.

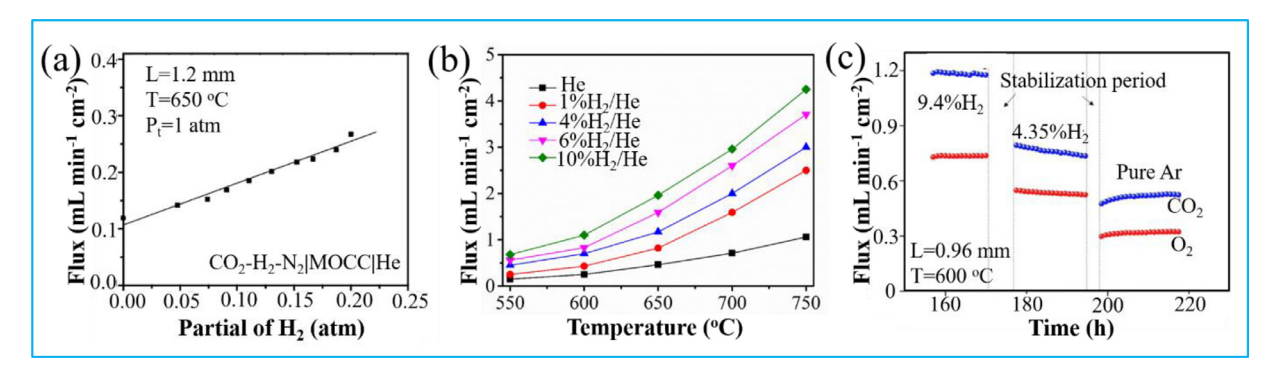


Fig. 12. (a) Dependence of CO₂ flux of an SDC-MC membrane on H₂ concentration at feed side. Reproduced from ref. [49] with permission from Royal Society of Chemistry, 2012; (b) CO₂ flux vs temperature of the LaNiO₃/SDC-MC membrane with LaNiO₃ catalyst using a H₂/He mixture gas as the sweep side. Adapted from ref. [128] with permission from Elsevier, 2020; (c) the effect of H₂ concentration in the sweep gas on CO₂ and O₂ fluxes of a MECC membrane. Reproduced from ref. [109] with permission from Elsevier, 2016.

increasing CO_2 flux in the opposite direction due to the charge neutrality requirement. From this point of view, MOCC membranes are more suited for capturing CO_2 from pre-combustion processes, where CO_2 is mixed with H_2 . The CO_2 flux of an SDC-MC membrane indeed increases with increasing partial pressure of H_2 at the feed side, see Fig. 12a [49]. A similar increase in the CO_2 flux with decreasing oxygen partial pressure at the feed side was observed by Chen et al. [127].

On the other hand, if H_2 is introduced to the sweep side of a MOCC membrane, CO_2 flux is observed to increase, see Fig. 12b [128]. The permeated CO_2 is assumed to react with H_2 via reverse water-gas shift reaction (RWGS) to produce CO and H_2O , thus increasing the CO_2 partial pressure gradient across the membrane. The CO_2 hydrogenation is considered to be an important reaction for CO_2 utilization to produce valuable chemicals, among which RWGS reaction is an interesting route due to the fact that the produced CO can be used as a feedstock for biological conversions [129-132]. Therefore, adding H_2 to the sweep side is one promising method to improve the CO_2 flux and produce useful products.

Like MOCC membranes, the CO_2 flux of MECC membranes also increases with adding H_2 to the sweep side, but with different mechanisms. Fang et al. [109] reported that CO_2 flux of an Ag-MC membrane with 9.41% H_2 -Ar as the sweep gas is 1.5 times higher than 4.35% H_2 -Ar and 2 times higher than pure Ar as the sweep gas, see Fig. 12c, confirming that lowering oxygen partial pressure at the sweep side can indeed significantly improve the CO_2 flux. The reason is simple: H_2 reacts with the co-permeated O_2 , shift-

ing the equilibrium ${\rm CO_3}^{2-}\!=\!{\rm CO_2}\!+\!1/2{\rm O_2}\!+\!2{\rm e}^-$ to the right-hand side, which increases the driving force for ${\rm CO_3}^{2-}$ transport [109]. The use of a fuel such as ${\rm H_2}$ and/or CO, as the sweep gas, to react with the permeated ${\rm O_2}$ can produce a stream containing only ${\rm CO_2}$, ${\rm H_2O}$ and heat; the latter chemicals can be either condensed out to obtain pure ${\rm CO_2}$ or fed into a high-temperature solid oxide electrolyzer to convert ${\rm CO_2}$ and ${\rm H_2O}$ into syngas or other valuable chemicals. Since the high cost of the ${\rm H_2}$ and/or syngas, a better way to improve the ${\rm CO_2}$ flux in practical applications is to use methane as the sweep gas, which will be discussed in section 4.1.

3.4.3. H_2O partial pressure

One of the intriguing findings for MOCC membranes is the promotional effect of $\rm H_2O$ on $\rm CO_2$ transport. The proposed mechanism is schematically shown in Fig. 13a for a pure MC, where $\rm H_2O$ reacts with MC phase, forming $\rm OH^-$ [133]; the latter involves in the $\rm CO_2$ transport as a charge-compensating ion transporting in the opposite direction. For a MOCC membrane under an opposing chemical potential of $\rm CO_2$ and $\rm H_2O$, $\rm O^{2-}$, $\rm CO_3^{2-}$ and $\rm OH^-$ are transported in the direction shown in Fig. 13b [103]. The experimental results showed asymmetrical $\rm CO_2$ flux enhancement by feeding steam (2.5%) into feed-side and sweep-side, *i.e.* 30% and 250-300%, respectively. It is understandable when both $\rm CO_2$ and $\rm H_2O$ are introduced into the feed-side, a positive gradient of $\rm CO_2$ promoting $\rm CO_3^{2-}$ transport and a negative gradient of $\rm H_2O$ hindering $\rm OH^-$ transport will be imposed on the membrane. The overall $\rm CO_2$ flux is mainly determined by the $\rm CO_2$ chemical gradient. In contrast,

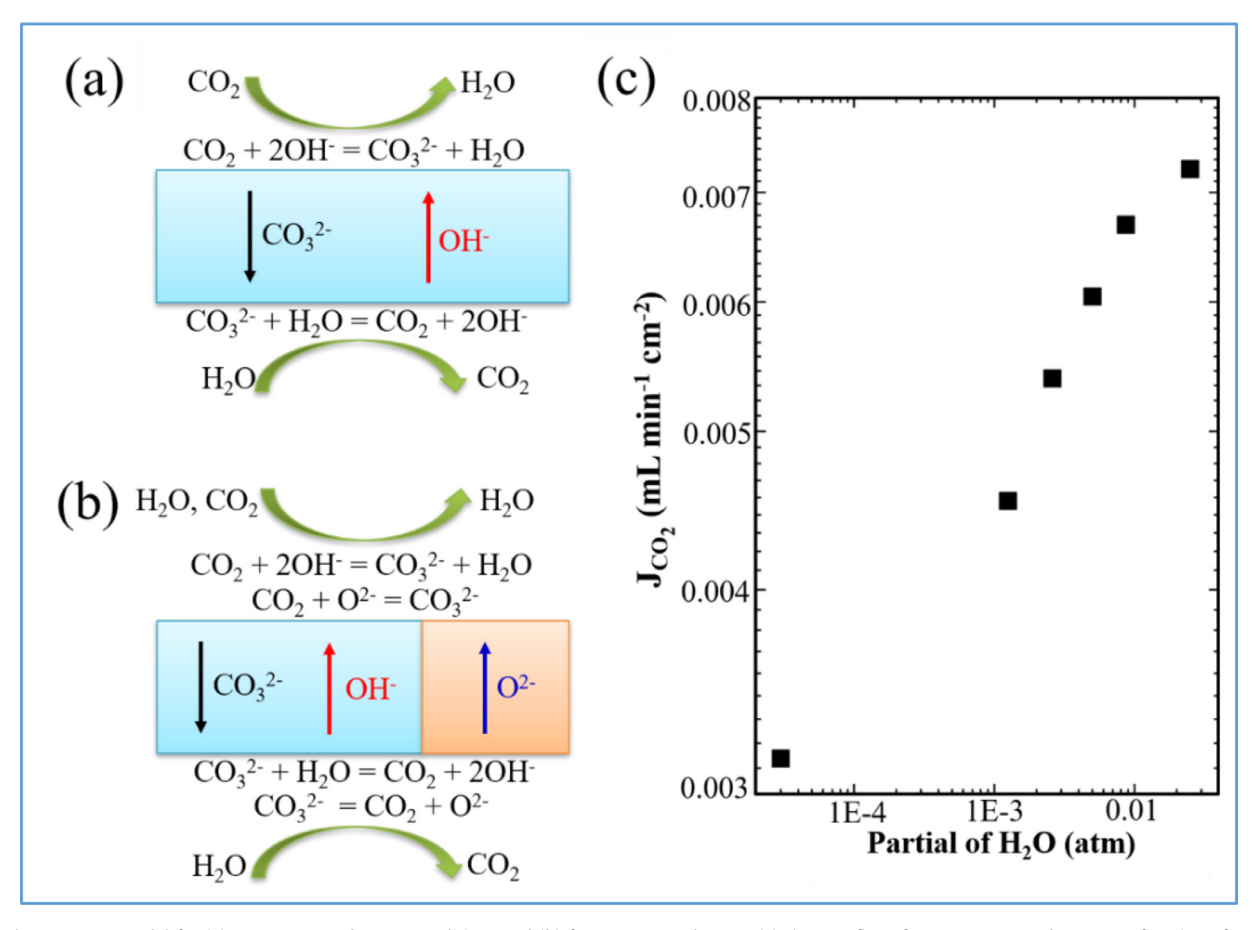


Fig. 13. The transport model for (a) a pure MC under wet conditions and (b) for MOCC membranes; (c) the CO_2 flux of a CeO_2 -MC membrane as a function of H_2O partial pressure in the sweep side at 550 °C. Feed gas: a dry mixture of 20% CO_2 , 20% He and 60% N_2 ; sweep gas: a moistened Ar. Adapted from ref. [103] with permission from Elsevier, 2015.

if H_2O is introduced into the sweep side, the counter transport of OH^- encourages CO_3^{2-} transport, resulting in a much-enhanced CO_2 flux. Under this circumstance, the higher the H_2O concentration the higher the CO_2 flux, as is clearly shown in Fig. 13c.

3.4.4. Other impurities

 SO_2 is a common species with concentration up to few thousands ppm in the flue gas produced from coal-fired power plants. Its effects on CO_2TMs determine the stability and thus lifetime of membranes to capture CO_2 directly from flue gas. Unfortunately, MC can spontaneously react with SO_2 even at a concentration as low as 20 ppm, forming sulfates. The formed sulfate decreases the conductivity of carbonate-ion in MC, leading to the degradation of CO_2 flux [100]. So far, there is no effective way to resolve this problem. Therefore, SO_2 must be removed from flue gas prior to its contact with CO_2TMs .

H₂S is another common impurity in the flue gas of coal-fired power plants. Like SO₂, H₂S has been observed with detrimental effects on catalytic performance of various catalysts [134-136]. However, an early study found that H₂S has a minimal effect on the MC phase. A study on the effect of H₂S on the flux stability of SDC-MC membrane showed that a Ce₂O₂S phase was formed on the SDC phase after exposure to a H₂S-containing gas, significantly decaying oxide-ion conductivity and thus CO₂ flux [99]. To solve this problem, two kinds of asymmetric membranes consisting of an additional SDC-BYS or SDC/BYS layer to adsorb H₂S, see Fig. 14a and 14b, respectively, were made [98]. A 10-12 times improvement in stability with such an asymmetric membrane over

the SDC-MC membrane was achieved, see Fig. 14c. In addition, the adsorbed layer of asymmetric membranes can be regenerated in an oxidizing stream, see Fig. 14d, allowing the membranes to be reused.

3.5. Surface modifications

Surface modification is a common method to enhance surface reactions/properties without changing the bulk properties. For CO₂TMs, it has been adopted to improve the wettability of solid matrix with MC phase so that MC phase can be effectively retained within the solid porous structure. The ideal material of choice for surface modification is LiAlO2, which is known to fully wet MC with zero contact angle and the benchmark electrolyte matrix material for molten carbonate fuel cells (MCFCs) [137-141]. During the development of CO₂TMs, it has also been used to coat the external surface of a solid porous matrix, such as in LSFCu-MC [54]. There are two functionalities deemed for the LiAlO₂ surface modification: 1) improving the wettability of the solid matrix with MC; 2) enhancing the surface adsorption of CO2. The CO2 flux was indeed observed to increase from 0.35 to 0.55 mL min $^{-1}$ cm $^{-2}$ at 750 °C through a 1.5-mm-thick LSFCu-MC membrane after the LiAlO₂ surface modification [54]. Since Al₂O₃ is known to form LiAlO₂ when it contacts with Li_2CO_3 at high temperatures [142], pure Al_2O_3 was used instead as a surface modification material. This work was first demonstrated on a porous Ag matrix by infiltrating an Al₂O₃ colloidal solution [107]. Fig. 15a shows that 5% Al₂O₃ concentration is the upper concentration limit, above which ${\rm CO_3}^{2-}$ transport would

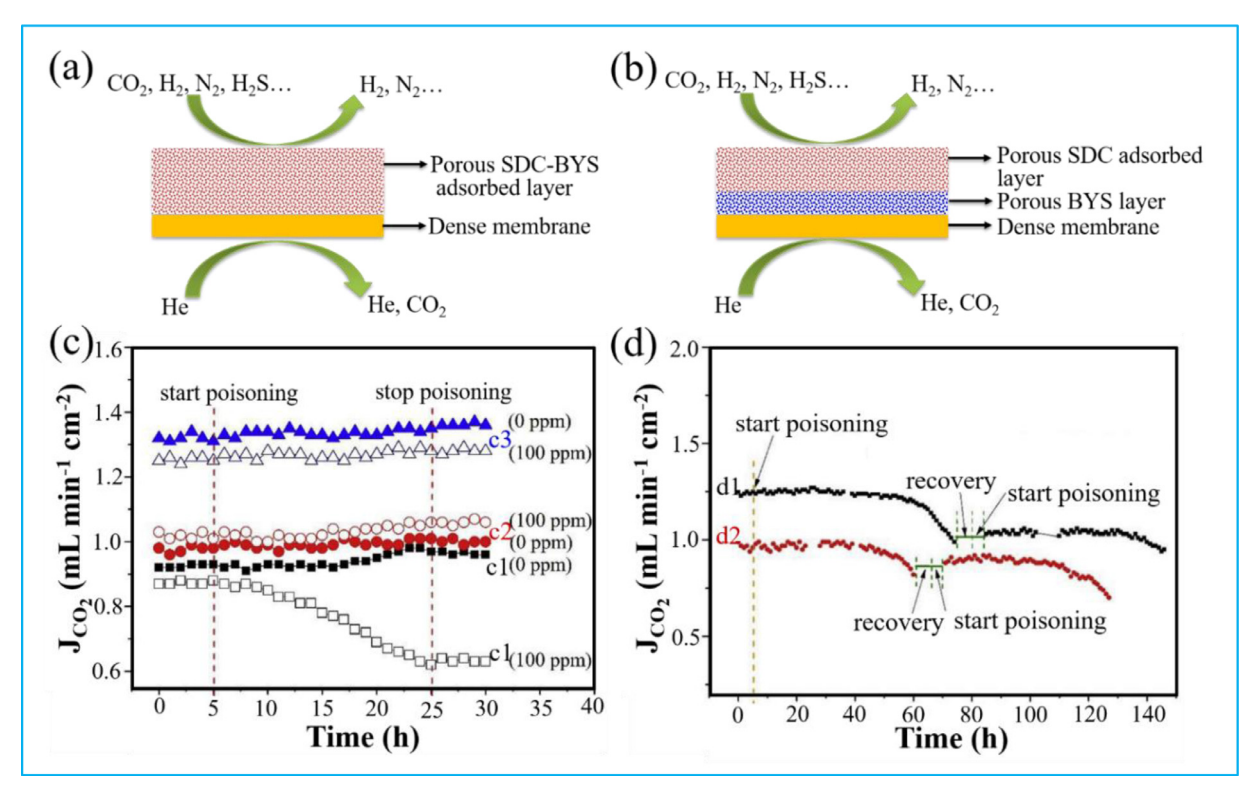


Fig. 14. (a) A two-layered asymmetric membrane, and (b) three-layered asymmetric membrane for CO_2 separation with a H_2S containing feed gas; (c) CO_2 flux stability of membranes with a $H_2/CO_2/N_2$ mixture feed gas containing 0 or 100 ppm H_2S at 750 °C: c1) single SDC-MC membrane; c2) three-layer membrane; c3) two-layer membrane; (d) sulfur resistance and regenerative power of the two-layered and three-layered membranes: d1) two-layered membrane, d2) three-layered membrane. Start poisoning means introducing 100 ppm H_2S in feed gas at 750 °C. Recovery in air stream at 850 °C for 6 h. Adapted from ref. [98] with permission from Elsevier, 2019.

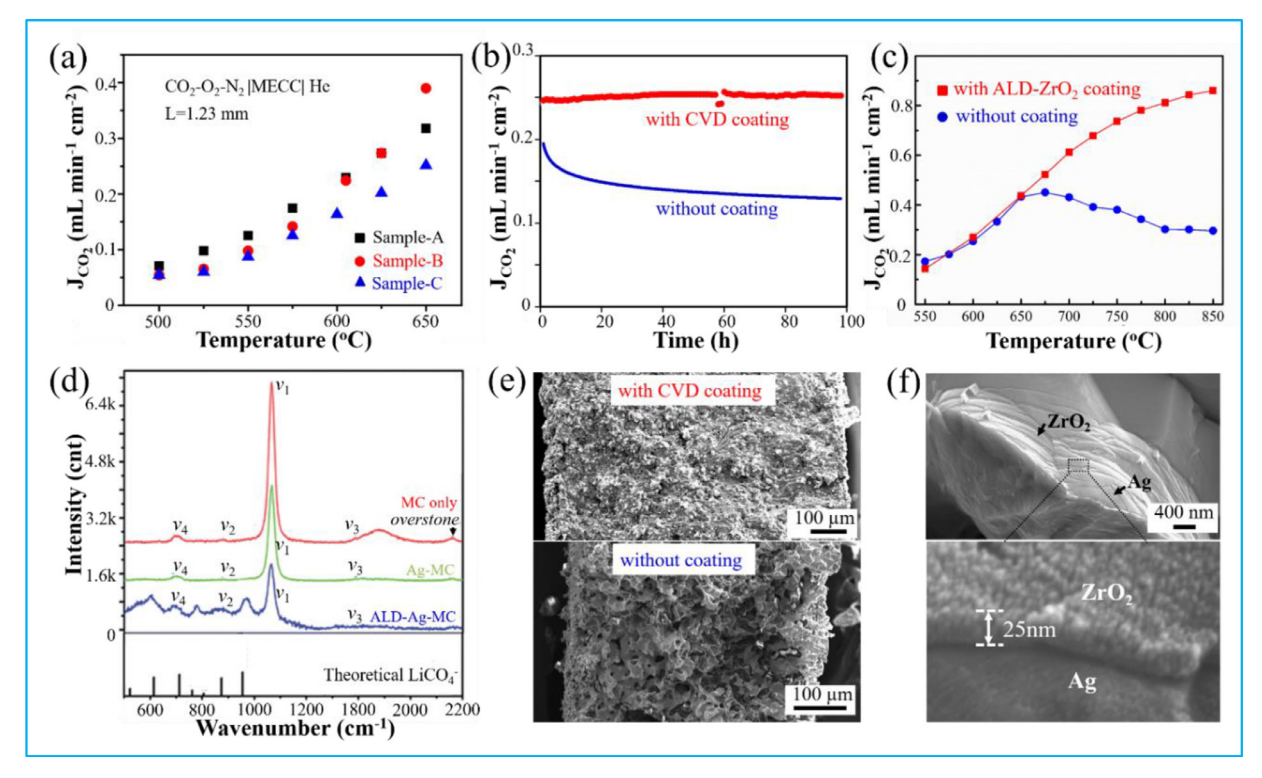


Fig. 15. (a) CO₂ fluxes vs temperature; Sample-A: without Al₂O₃ coating, Sample-B: coated with 5%Al₂O₃ colloidal, Sample-C: coated with 10% Al₂O₃ colloidal. Reproduced from ref. [107] with permission from Elsevier, 2014. (b) CO₂ fluxes vs time under a simulated flue gas composition at 650 °C. (c) CO₂ fluxes vs temperature of the Ag-MC membrane with and without the ALD-ZrO₂ coating. (d) The *in-situ* Raman spectra collected from pure MC, Ag-MC, and ALD-Al₂O₃-coated Ag-MC samples at 500 °C in a 15% CO₂, 10% O₂ and 75% N₂ environment. The bottom Raman shifts are calculated using DFT for the LiCO₄⁻ anion in a wavenumber range of 500-1100 cm⁻¹. MC: 52 mol% Li₂CO₃-48 mol% Na₂CO₃. (e) Cross section of an Ag-MC membrane after 100 h test. (f) Microstructure of a porous Ag matrix overcoated with ALD-ZrO₂; Adapted from refs. [51,80,108] with permission from Royal Society of Chemistry, 2015, 2016, 2016.

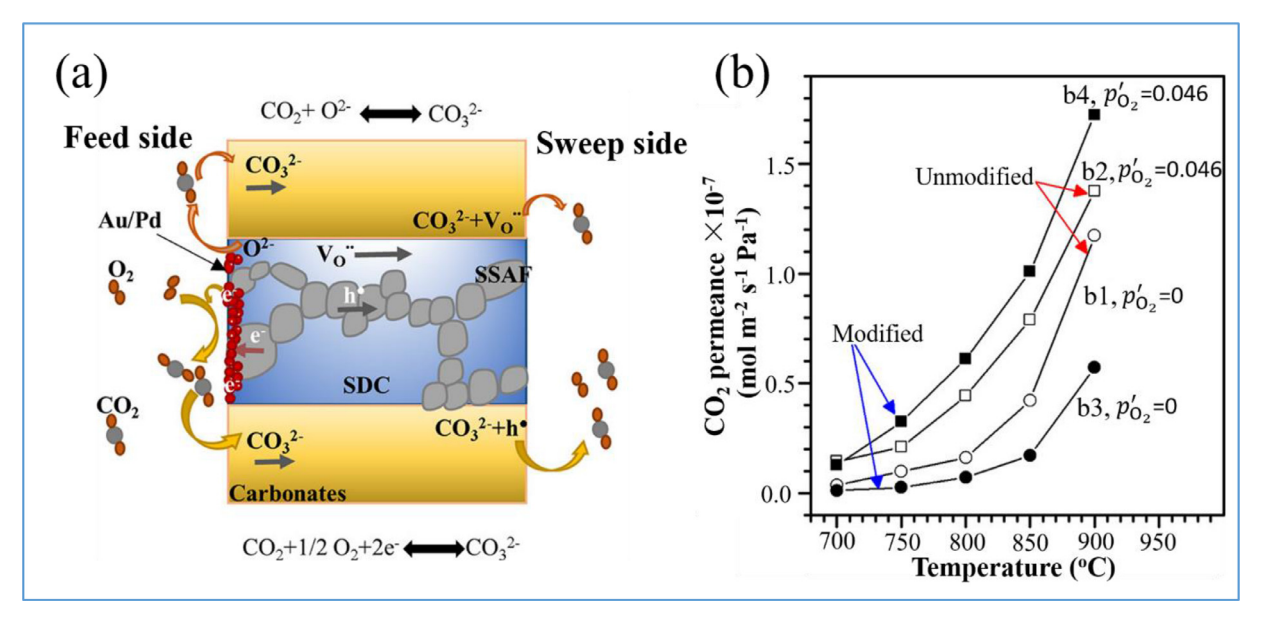


Fig. 16. (a) Schematic representation of CO₂ separation mechanism of SDC-SSAF-MC dense membrane modified superficially with Au-Pd particles. (b) CO₂ permeance dependence of temperature with the SDC-SSAF-MC membranes. All these experiments were performed using $P_{\text{CO}_2} = 0.115$ atm in feed gas. Adapted from ref. [122] with permission from American Chemical Society, 2018.

be blocked by the insulating Al_2O_3 and/or LiAlO₂. The long-term stability of an Al_2O_3 -coated Ag-MC membrane has been improved to 90% flux retention over 130 h, whereas it is only 15% for the pristine sample over 60 h.

Chemical vapor deposition (CVD) and atomic layer deposition (ALD) were further employed to coat high-quality conformal Al_2O_3 layers over the surfaces of a porous Ag matrix. A significantly improved CO_2 flux and long-term stability was reported by Tong et al. [80,108]. For the CVD- Al_2O_3 coated Ag-MC sample tested at 650 °C, no sign of degradation was observed for 100 h, see Fig. 15b, whereas the pristine sample lost nearly 50% of its original flux in the first 20 h. Large pores and Ag particles in the post-tested pristine sample are clearly visible in Fig. 15e (bottom) of SEM image, implying that serious sintering of Ag and loss of MC have occurred. In contrast, the coated sample in Fig. 15e (top) shows a relative dense microstructure after the long-term test, demonstrating alleviated Ag-particle sintering and enhanced MC retention by the Al_2O_3 coating.

An interesting phenomenon observed on the Ag-MC membrane with ALD-derived Al $_2$ O $_3$ coating was the abnormal CO $_2$ and O $_2$ flux ratio, *i.e.* CO $_2$:O $_2$ =2:3, apart from the expected CO $_2$:O $_2$ =2:1 [80]. The *in-situ* Raman spectroscopic study detected a new species CO $_4$ ²- on the surface of this ALD-Al $_2$ O $_3$ coated sample, see Fig. 15d, but not on the pristine sample. Therefore, the following enabling surface reaction was proposed to take place: CO $_2$ + 3/2O $_2$ + CO $_3$ ²- +2e $_3$ = 2CO $_4$ ²-, by which the CO $_2$:O $_2$ becomes 2:3 [80]. The migration of CO $_4$ ²- in MC has been previously proposed via "cogwheel" mechanism by Zhang et al., see Fig. 11 [60]. The underlying reason for the enhanced oxygen flux is that Al $_2$ O $_3$ increases the basicity of the MC, which improves oxygen dissolution at the TPBs to favor the CO $_4$ ²- formation.

To mitigate the sintering issue of porous Ag matrix, a nanoscaled refractory ZrO_2 layer was coated on the wall of Ag matrix by ALD method, see Fig. 15f, resulting in a much-stabilized Ag matrix against sintering [51]. Such an Ag-MC membrane can operate stably at higher temperatures (> 700 °C), see Fig. 15c, which makes CO_2 capture and conversion at high enough temperatures in a single reactor possible. In the following section, we will demonstrate a dry-oxy CH_4 reforming using such a MECC membrane.

Another example of using surface modification to improve wettability of the porous matrix with MC is the BYS-MC membrane. BYS is known to be the best oxide-ion conductor, but it is unfortunately non-wettable to MC. To improve the wettability of BYS with MC, a thin layer of Al_2O_3 was coated over BYS pore surfaces [63]. However, as shown in Table 3, a lower CO_2 flux than SDC-MC membrane was observed, even though BYS has a higher oxide-ion conductivity than SDC [49,95]. One possible reason for the lower CO_2 flux is low ε/τ ratio of the porous BYS matrix and lowered porosity (20-30%) by surface modification. Another possible reason is that the surface coating may hinder the reaction. Thus, there exist rooms to improve CO_2 flux by optimizing the microstructure of BYS

An interesting study of surface modification is to apply a catalyst layer on the membrane surface to promote surface reactions, which is particularly effective to surface controlled CO_2TMs . A higher CO_2 flux was achieved by coating Au-Pd (46:54 at.%) metallic particles on the feed surface of a dense MEOCC (SDC-SSAF-MC) membrane [122]. Fig. 16a shows the proposed CO_2 permeation mechanism. In the presence of O_2 at the feed side, the catalytic activity provided by Au-Pd particles promote the reduction of O_2 into O^2 , which further reacts with CO_2 to form CO_3^2 , leading to an increase in CO_2 flux (from 0.28 to 0.35 mL min⁻¹ cm⁻²) with O_2 in the feed side, see Fig. 16b. However, in the absence of O_2 at the feed side (MOCC model), CO_2 flux was decreased by the surface modification, due to the partially blocked surface-active sites by Au-Pd coating.

4. CO₂TM-Based Catalytic Membrane Reactors

Converting CO_2 into valuable products has attracted significant interest in recent decades from both academia and industries due to its implications to a sustainable and carbon neutral energy future. However, CO_2 is a very stable chemical with strong C=O bond. To break it, a large amount of energy is needed. Therefore, a majority of CO_2 conversion research has been conducted at high temperatures where thermal energy is available to activate the cleavage of the bond. The CO_2 TMs' ability to permeate CO_2 at high temperatures provides an excellent opportunity to couple CO_2 capture with conversion in a single membrane reactor, thus

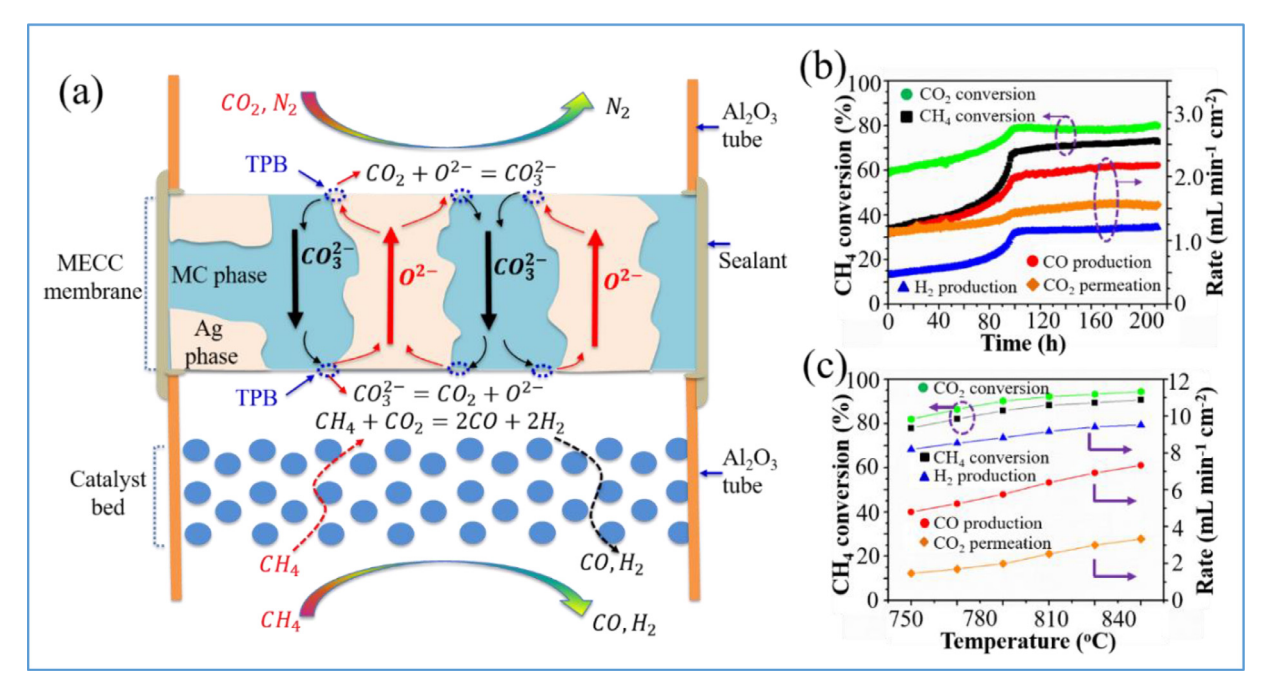


Fig. 17. (a) Schematic illustration of MOCC membrane reactor for CO_2 capture and DMR coupling; (b) stability of the DMR performance in the MOCC membrane reactor at 850 °C with the LNF catalyst, GHSV = 5800 h⁻¹; (c) performance of bi-reforming of methane vs temperature. Catalyst: NMP; CH₄ concentration in sweep gas: 4.7%; H₂O concentration: 3%. GHSV = 5800 h⁻¹. Reproduced from ref. [92] with permission from American Chemical Society, 2017.

simplifying system design and lowering cost. In this section, we review the development of CO_2TM reactors that combine CO_2 capture and conversion in a single step.

4.1. Coupling with methane reforming

 CH_4 reforming with CO_2 as an oxidizer to produce syngas (H_2 and CO) represents one of the most important chemical reactions to mitigate global warming effect because it utilizes two most powerful greenhouse gases. Commonly known as dry methane reforming (DMR), the reaction produces a syngas composition with $H_2:CO=1:1$ at the expense of high thermal energy [143-146]:

$$CO_2 + CH_4 = 2CO + 2H_2$$
, $\Delta H^o_{298K} = 247 \text{ kJ mol}^{-1}$ (21)

The H_2 :CO =1:1 syngas is ideal for the synthesis of valuable oxygenated chemicals and long-chain hydrocarbons [147]. Coking is a major issue for DMR to scale up to the commercial level. In addition, DMR reaction requires pure CO_2 , which is a commodity produced from rather expensive industrial processes such as "amine chemical washing", not to mention that compression and transportation of the CO_2 to a DMR site add extra costs. Use of CO_2 TMs for CO_2 capture and conversion offers a low-cost solution to DMR, *i.e.* the captured hot CO_2 at power plants can be directly converted on-site into valuable products such as syngas, avoiding compression and transportation and thus saving cost and energy.

The combined CO_2 capture and DMR process was first theoretically studied using an LSCF-MC tubular membrane reactor [148], in which a flue gas and CH_4 are fed into shell and tube sides, respectively, with catalyst packed on the CH_4 side. During operation, CO_2 permeates from the shell side to the tube side and reacts with CH_4 to produce syngas. The modeled results showed that CH_4 conversion and CO_2 flux can be as high as 48.06% and 1.52 mL min $^{-1}$ cm $^{-2}$ at 800 °C, respectively, for a 0.075-mm-thick membrane under the condition of CH_4 space velocity of 3265.31 h^{-1} and CO_2 partial pressure of 1 atm. The study also showed that adding O_2 into shell side will further improve reactor's performance.

The DMR performance was experimentally demonstrated in a LSCF-MC membrane reactor [149]. A CO₂ conversion as high as 88.5% was achieved with a packed Ni/γ -Al₂O₃ catalyst, and the CO₂ conversion increases in the order of: blank system (without catalyst) < LSCF combustion catalyst < Ni/γ -Al₂O₃ catalyst, due to the increased catalytic activity. However, the chemical interaction between LSCF and CO2 eventually led to stability issue. In contrast, with a GDC-MC membrane reactor loaded with a Ni-MgO-1 wt% Pt (NMP) catalyst and a LaNi $_{0.6}$ Fe $_{0.4}$ O $_{3-\delta}$ (LNF) catalyst, see Fig. 17a, Zhang et al. demonstrated a much improved DMR performance [92]. At 850 °C, over NMP and LNF catalysts, the two membrane reactors showed syngas production rates of 6.99 and 6.10 mL min⁻¹ cm⁻², and CH₄ conversions of 93.9% and 73%, respectively. By comparison, the LNF catalyst exhibited a stronger coking and coarsening resistances than NMP catalyst, and thus a better long-term stability. No sign of degradation within 200-h of operation was observed for the membrane reactor with LNF catalyst, see Fig. 17b. Ni nanoparticles exsolved from LNF lattice under reducing environments are the underlying reason for the observed pre-activation behavior and sustained catalytic activity because exsolution process takes time and the lattice Ni is free of coarsening. Compared to Ar sweep gas, the CO2 flux is further increased with CH₄ sweep gas owing to the in situ DMR reaction that consumes the permeated CO2 and shifts the equilibrium of the reaction. For example, at 850 °C and over NMP catalyst, the CO2 flux was increased from 0.67 to 2.25 mL min⁻¹ cm⁻² at a CO₂ conversion rate of 96% by switching the sweep gas from pure Ar to 3.57% CH₄-Ar mixture [92].

The H_2/CO ratio of the produced syngas by the above reactor was generally lower than 1, largely due to the concurrent reverse water gas shift (RWGS) reaction $H_2 + CO_2 = H_2O + CO$ [150-153]. The lower H_2/CO ratio is unfavorable to Fisher-Tropsch liquid fuels synthesis. To achieve a higher H_2/CO ratio, DMR with moistened CH_4 as the sweep gas was performed, by which steam methane reforming (SMR) producing a syngas with $H_2/CO = 3/1$ is expected to elevate the net H_2/CO ratio. A syngas with higher H_2/CO ratio as well as a higher syngas production rate were indeed observed

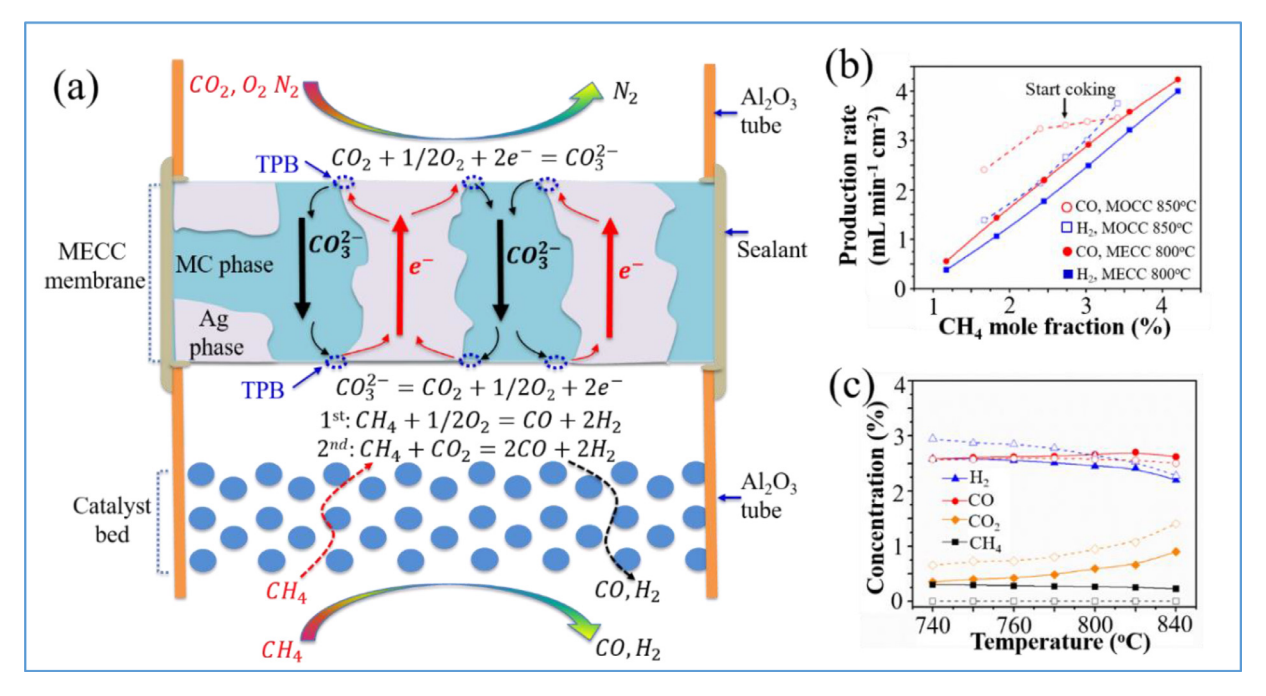


Fig. 18. (a) Schematic illustration of the MECC membrane reactor loaded with a catalyst bed for CO_2/O_2 co-capture and DOMR coupling; (b) performance comparison between MOCC-DMR and MECC-DOMR membrane reactors. Solid lines: MECC at 800 °C; dashed lines: MOCC at 850 °C; (c) comparison of experimental data and thermodynamic equilibrium results of the DOMR effluent vs temperature with a sweeping 1.8% CH₄-Ar. Reproduced from ref. [119] with permission from American Chemical Society, 2017.

by adding 3% H_2O into CH_4 . Fig. 17c shows that the syngas production rate and H_2/CO ratio are 16.3 mL min⁻¹ cm⁻² and 1.36, respectively, with a 3% moistened 4.8% CH_4 -Ar sweep gas at 850 °C over NMP catalyst [92].

MECC membranes have a fundamental advantage over MOCC for methane reforming because they can transport CO2 and O2, simultaneously. The presence of O2 not only mitigates coking, but also provides the heat resulted from partial oxidation reaction for DMR. Such a reaction is commonly known as dry-oxy methane reforming (denoted as DOMR), see Fig. 18a. Due to the hightemperature requirement, an Ag-MC MECC membrane overcoated with ALD-ZrO₂ was used in a reactor packed with the NMP catalyst [119]. During operation, the sweep gas (CH₄) reacts with both CO₂ and O2 permeated in the MECC membrane reactor, producing a syngas with a higher H₂/CO ratio. The performance of MOCC-DMR and MECC-DOMR membrane reactors are compared in Fig. 18b, in which the same catalyst NMP was used, but the reactor temperature was 800 °C for the MECC membrane reactor to ensure minimal silver sintering and 850 °C for the MOCC membrane reactor. Thermodynamically, coking is more favorable to form at 800 °C than 850 °C. The production rates of H₂ and CO linearly increases with methane concentration for the MECC membrane reactor as a sign of free coking, but this is not the case for the MOCC membrane reactor, implying that the MECC membrane reactor has a better coking resistance than the MOCC counterpart.

It was also found that CH_4 preferentially reacts with O_2 over CO_2 during DOMR [119]. The experimental data are, in general, in good agreement with theoretical predictions in trending and magnitude in a temperature range of 740 to 800 °C, see Fig. 18c, suggesting both thermodynamics and kinetics play active roles in the laboratory-scale DOMR reactor. However, one issue for Agbased MECC membrane reactors is the poor long-term stability caused by the Ag-sintering over the extended period, even with ALD-ZrO $_2$ surface modification. In addition, the high cost of Ag and ALD coating process are also the concerns for practical applications.

In searching for low-cost and stable MECC membranes, NiO-MC membrane was reported to exhibit a high CO_2/O_2 flux and good stability at 850 °C [106]; the latter matches well with DOMR reaction temperature. However, the reduction of NiO into Ni metal under a reducing atmosphere induces volume shrinkage and thus causes loss of MC and poor stability. To address this problem [55], a triple-phase NiO-SDC-MC membrane was developed in laboratory. A stable CO₂/O₂ flux and high DOMR performance over the NMP catalyst were achieved. During the initial period of operation, NiO first reacts with MC phase to form an electron-conducting phase LNO at high temperatures. Meanwhile, SDC and MC provide oxide-ion and carbonate-ion conductivities, respectively. At 850 °C, such a MEOCC membrane reactor was demonstrated with a syngas production rate of 7.4 mL min⁻¹ cm⁻² and CH₄ and CO₂ conversion rate of 84.1 and 62.9%, respectively. No degradation was observed on the reactor for 130 h [55]. Similarly, a good DMR performance using a $Ce_{0.9}Pr_{0.1}O_{2-\delta}-Pr_{0.6}Sr_{0.4}Fe_{0.5}Co_{0.5}O_{3-\delta}-MC$ membrane reactor over a 10 wt% Ni/γ - Al_2O_3 catalyst was obtained at 800-875 °C with CH₄-Ar (4.5-95.4 vol%) sweep gas [57]. The CH₄ conversion increases from 74 to 99% by increasing the temperature from 800 to 875 °C, with a produced H_2/CO ratio varying from 1.3 to 2.1.

4.2. Coupling with ethane dehydrogenation

Ethylene is one of the most important chemical commodities to our modern society. Commercial production of ethylene is high-temperature (> 900 °C) non-catalytic thermal dehydrogenation of either ethane or naphtha in the presence of steam, a process commonly known as Steam Cracking (SC) [154]. Technically, a commercial steam cracker operated above 900 °C can achieve a single pass ~70% conversion with ~ 50% yield with ethane as the feedstock [155]. However, the thermal dehydrogenation of ethane (TDHE) process is highly endothermic, consuming ~22 GJ of energy and emitting 1.5 ton of CO₂ per ton of ethylene produced [156]. In addition, SC reactors need frequent shutdowns to decoke, resulting in high costs in operation and maintenance. One way to

decrease ethylene production cost and carbon emissions is to boost TDHE kinetics by catalysts, so that the operation temperature can be lowered. However, due to the thermodynamic constraint at low temperatures, the equilibrium ethane conversion is rather low, e.g. 15% at 600 °C and 40% at 650-700 °C [157]. Therefore, development of advanced ethylene production technologies is still needed.

Oxidative dehydrogenation of ethane (ODHE) is a promising technology to convert ethane into ethylene with lower energy, higher ethane conversion rate and less coking [158]. Both O2 and CO₂ have been used as oxidants for ODHE. A nearly 100% ethane conversion can be achieved with pure O₂ as the oxidant. However, it is difficult to avoid deep oxidation of ethylene since ethylene is chemically more reactive than ethane. Other issues associated with O2-ODHE are thermal management with excessive heat, uncontrollable local combustion, and cost for pure O₂ [159-161]. In comparison, CO2 with a weaker oxidizing power has the ability to convert ethane to ethylene without over-oxidation. The co-fed ODHE reactors, however, often produce a stream with low concentration of ethylene and high concentration of CO2 due to the use of high inlet CO_2/C_2H_6 ratio (> 3/1) to avoid carbon deposition [162-164]. The low concentration of ethylene product increases the cost for downstream purification.

It is important to note that membrane reactors present an inherent advantage over conventional co-fed ODHE reactor systems. They operate under a continuous mode and add reactants and remove products incrementally along the length of a tubular plug flow membrane reactor, thus enhancing conversion and selectivity. This feature has a potential to simplify the downstream ethylene purification process, which is a significant cost item for commercial ethylene production. OTM reactors were the first membrane systems tried for O2-ODHE process to replace co-fed O2ethane systems [159,161,165], and a remarkable performance has been obtained at high temperatures (\geq 800 °C). For example, a $Bi_{1.5}Y_{0.3}Sm_{0.2}O_{3-\delta}$ tubular membrane reactor was reported for ODHE with an ethane conversion of 56% and ethylene selectivity of 80% at 875 °C [159]. On another case, a mixed conducting $BaCo_xFe_yZr_{1-x-y}O_{3-\delta}$ (BCFZ) hollow-fiber OTM membrane reactor was also reported for ODHE with similar performance at 800 °C [166]. However, a critical challenge for these OTM membrane reactors to be practical is their poor chemical stability in CO2containing atmospheres [166].

CO2TM reactors can capture CO2 and instantly use it as a soft oxidizer to convert ethane into ethylene in single catalytic membrane reactor. One advantage is the excellent chemical stability of CO₂TMs in CO₂-containing atmospheres. The working principle of the CO₂TM reactor for ethane conversion is illustrated in Fig. 19a, where the captured CO₂ has two functionalities: 1) continuous removal of H₂ through RWGS reaction, thus enhancing C₂H₆ conversion; 2) elimination of carbon deposition by the Reverse Bouduoard (RB) reaction ($C + CO_2 = 2CO$), thus improving the coking resistance. Such a combined CO₂ capture and instant ODHE was successfully demonstrated in laboratory by using a GDC-MC membrane reactor loaded with a 5 wt% $Cr_2O_3/ZSM-5$ catalyst [120]. The reactor achieved a ~75% C₂H₆ conversion, ~77% CO₂ conversion and ${\sim}82\%$ C_2H_4 selectivity at 800 °C with 4.0% $C_2H_6\text{-Ar}$ as the sweep gas. The results shown in Fig. 19b suggest that without CO₂ and/or catalyst the conversion is primarily dominated by TDHE reaction, suffering severe coking even though the initial C2H4 yield is higher. In the presence of CO2 and catalyst, the main ethylene production route is still TDHE reaction, but the permeated CO2 can effectively lift carbon through the RB reaction and remove H₂ through RWGS reaction. The major reaction pathways under each condition are proposed in Fig. 19c. Due to the concurrent RWGS shifting TDHE equilibrium and RB reaction lifting coke, a good long-term stability was achieved, see Fig. 19d. The SEM microstructure of the CO₂TM after the test, see Fig. 19e, shows no obvious structural degradation of the membrane compared to the original structure.

4.3. Coupling with H_2 enrichment process

Pre-combustion CO_2 capture from integrated gasification combined cycle (IGCC) coal-fired power plants has attracted considerable attention in recent decades because of its carbon-free combustion process. In a typical IGCC power cycle, coal is first steam-gasified at high temperatures (\sim 1500 °C) to produce high pressure (\sim 30 bars) syngas. The water gas shift (WGS) reaction is then used to convert CO/H_2O to CO_2/H_2 , resulting in a high-pressure CO_2 and CO_2 and CO_2 is then separated from CO_2 via a room temperature pressure swing process over solid sorbents and finally used for carbon-free combustion. Given the fact that the WGS reaction is exothermic, low temperature operation is thermodynamically favored but with a penalty in kinetics and loss of thermal energy in the gasified syngas.

High temperature Pd-based H_2 transport membrane (HTM) reactors were first studied as an approach to separating H_2 from CO_2 in WGS gas, aiming to shift WGS reaction ($H_2O + CO = CO_2 + H_2$) to the right-hand side in the reactor and producing a high-pressure CO_2 retentate stream [167]. In comparison, CO_2TM reactors can produce a high-pressure H_2 retentate by removing CO_2 from WGS gas, while shifting WGS equilibrium; the produced high-pressure H_2 is better suited for combustion. Another advantage of CO_2TM over HTM is its better stability. Pd-based HTMs are known to have high-temperature stability issue. Moreover, at high operating temperatures, no catalyst is needed for WGS because of sufficiently fast kinetics, thus further simplifying the reactor design. A schematic of catalyst-free, MOCC membrane reactor for syngas WGS is conceptually shown in Fig. 20a [101].

The initial performance at 900 °C of such MOCC-based syngas WGS tubular reactor is encouraging: $0.36~\text{mL}~\text{min}^{-1}~\text{cm}^{-2}$ of single-pass CO_2 recovery flux and 26.1% of CO conversion [101]. This level of performance is much better than the conventional fixed-bed reactors under identical conditions, see Fig. 20b. The study also suggests that increasing the pressure of reaction side is an effective way to enhance CO conversion and CO_2 recovery. In addition, SDC-MC membrane reactor exhibits excellent thermal and chemical stability under WGS reaction and CO_2 separation conditions, promising the durability of WGS reactors for combined CO_2 capture.

The H_2 enrichment from the WGS process is further expanded to steam reforming of methane (SRM) process; a schematic of the reactor is shown in Fig. 20c [168]. An asymmetric membrane with a thin and dense SDC-MC layer was used to improve the CO_2 flux. Comparing to the fixed-bed reactor, H_2 yield with CO_2 TM reactor is improved from 81% to 91% at 900 °C, see Fig. 20d, while CH_4 conversion remains almost unchanged between the two kinds of reactors.

The CO₂TM reactors have also been demonstrated to enrich H_2 from syngas (H_2+CO) by selective oxidation of CO and subsequent CO_2 removal. The concept was originally proposed by Ovalle-Encinia et al. [102] using a $Ce_{0.80}Sm_{0.15}Sr_{0.05}O_{2-\delta}Sm_{0.6}Sr_{0.4}Al_{0.3}Fe_{0.7}O_{3-\delta}$ (CSSO-SSAF) supported MEOCC membrane reactor. Fig. 21a and 21b show the temperature-dependent gas compositions on feed and sweep sides, respectively, where only CO_2 was observed to permeate through the membrane to the sweep side. The presence of CO_2 both in feed and sweep side confirmed that CO was indeed oxidized to CO_2 , while H_2 concentration is almost unaffected and thus enriched in the feed side. To explain this phenomenon, FTIR spectroscopy was applied to determine whether water was produced at the feed side by $H_2+O^2-=H_2O+2e^-$, see Fig. 21c. Based on a semiquantitative calibration, CO/H_2 oxidation selectivity of the MEOCC mem-

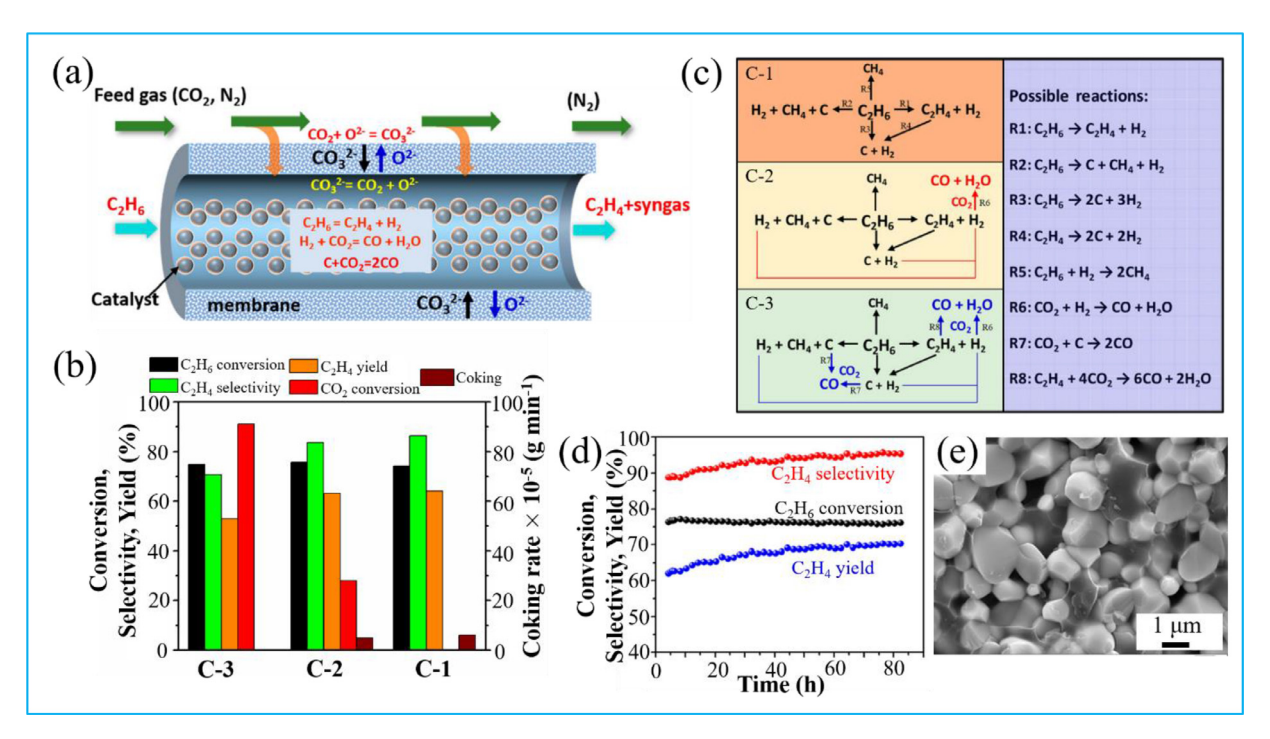


Fig. 19. (a) Working principle of the ethane conversion CO_2TM reactor; (b) comparison of CO_2TM performance at 800 °C under three conditions: C-1: no catalyst, no CO_2 feed; C-2: no catalyst with CO_2 feed; C-3: with 5 wt% Cr_2O_3/ZSM -5 catalyst and CO_2 feed; (c) the proposed CO_2 -ODHE mechanisms based on GDC-MC membrane reactor; (d) stability of the catalytic CO_2 -ethane conversion performance with CO_2TM reactor tested at 800 °C; (e) SEM image of the membrane after the performance stability test. Reproduced from ref. [120] with permission from American Chemical Society, 2019.

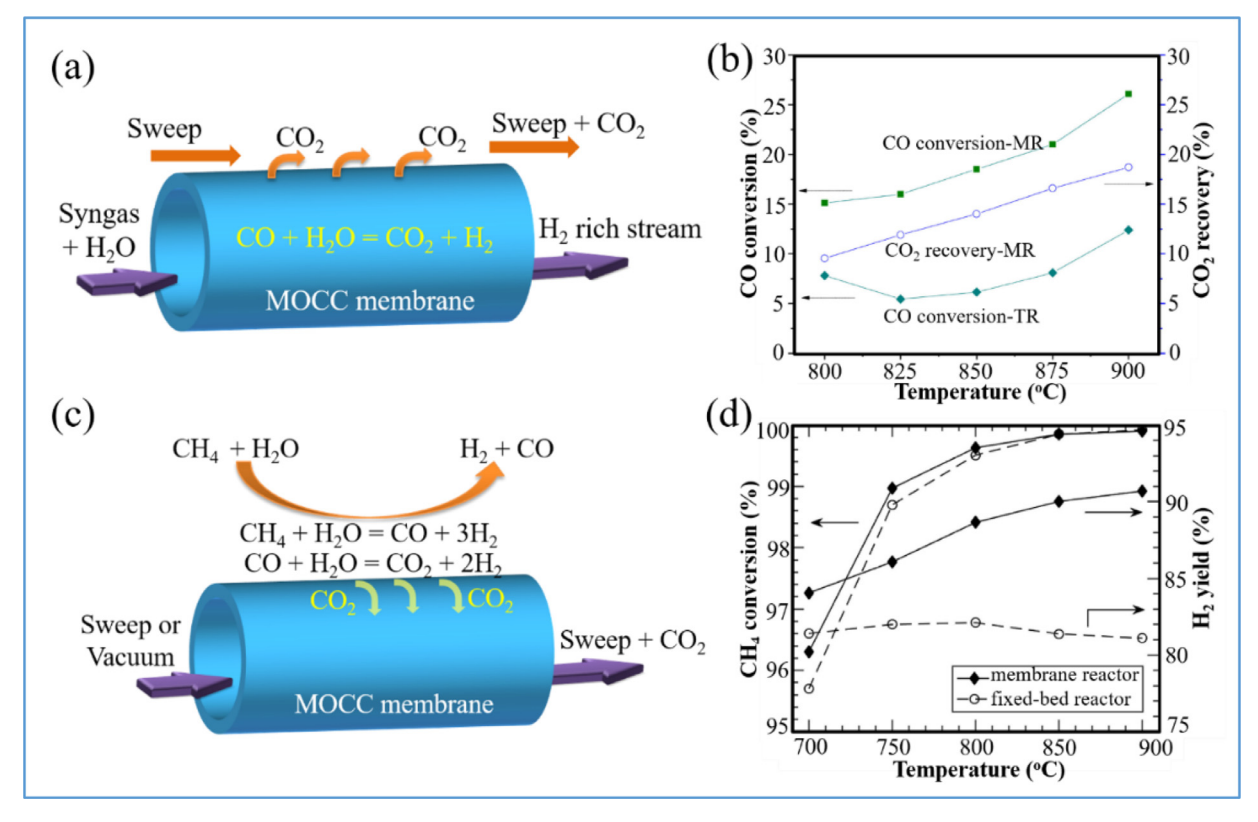


Fig. 20. (a) Schematic of catalyst-free, MOCC membrane reactor for syngas WGS reaction; (b) temperature-dependent performance of membrane reactor (MR) and traditional fixed-bed reactor (FBR) for high temperature syngas WGS reaction without catalyst. Adapted from ref. [101] with permission from Elsevier, 2016. (c) Schematic of MOCC membrane reactor for steam reforming of methane; (d) CH₄ conversion and H₂ yield of the membrane reactor and conventional FBR at 700-900 °C. Adapted from ref. [168] with permission from Elsevier, 2020.

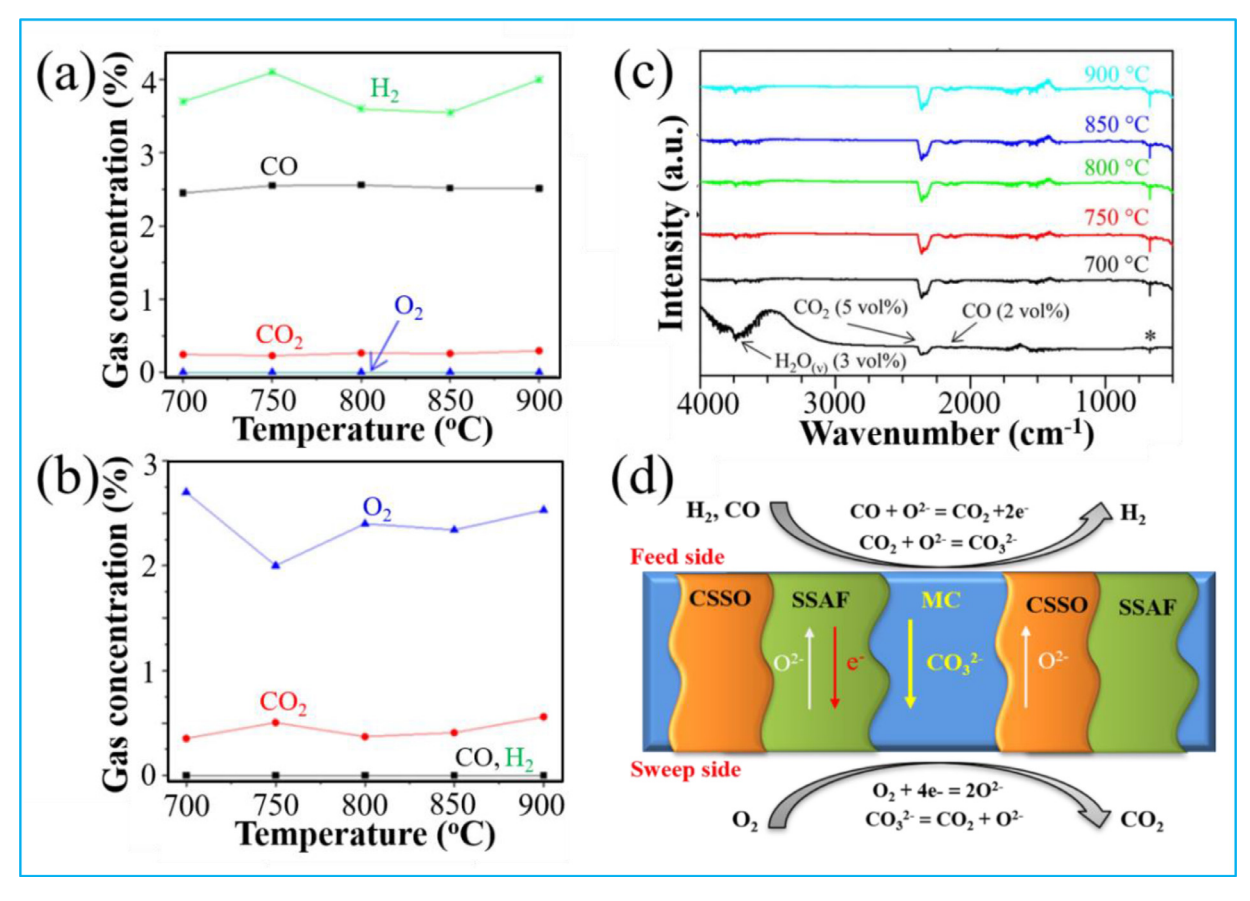


Fig. 21. Temperature-dependent gas compositions on feed (a) and sweep side (b), respectively. Feed gas: 3% CO, 4% H_2 , Ar balance. Sweep gas: 3% O_2 , Ar balance. (c) FTIR spectra of feed side, where it also includes a FTIR spectrum ($H_2O_{(v)}$, CO, and CO_2 gas mixture diluted in Ar, labeled as *) for determining semi-quantitatively the $H_2O_{(v)}$ concentration for comparison purposes. (d) Schematic representation of CO oxidation and CO_2 permeation in a CSSO-SSAF-MC membrane reactor. Adapted from ref. [102] with permission from America Chemical Society, 2020.

brane reactor was estimated to be \sim 39.1 and 19.4 at 700 and 900 °C, respectively. Therefore, CO oxidation was favored over steam formation. The possible mechanisms of CO oxidation and CO₂ permeation are schematically illustrated in Fig. 21d, in which O²⁻ is initially formed on the sweep side through the reaction $O_2 + 4e^- = 2O^{2-}$, then O^{2-} transports from the sweep side to the feed side through the oxide-ion phase, and reacts with CO on the feed side to produce CO_2 , e^- , and CO_3^{2-} through $CO + O^{2-} = CO_2 + 2e^-$ and $CO_2 + O^{2-} = CO_3^{2-}$. Finally, CO_3^{2-} and e^- are transported to the sweep side where CO_2 is released. On the other hand, the permeated O^{2-} can also react with H_2 to produce H_2O via $H_2 + O^{2-} = H_2O$ at the feed side; the latter reacts with CO via WGS reaction to yield H2 and CO2. The produced CO2 can further react with O²⁻ to form CO₃²⁻ and transport to the sweep side and be released. In the whole process, H2 is almost unaffected and thus enriched in the feed side.

5. Challenges and Potential Solutions

Despite the intrinsic advantages (*e.g.* in selectivity, permeability, modularity, scalability, continuity, simplicity, etc.) of electrochemical CO₂TMs and associated reactors over current benchmark sorption-based methods, and their potentials to be an energy-efficient and cost-effective technology for combined CO₂ capture and conversion, the current development of CO₂TMs and reactors is still limited at laboratory level. Demonstrations at bench-, pilot-scale and ultimately commercial scale require strong R&D activities to overcome the following key challenges.

5.1. Key challenges

The most critical challenge for the current CO₂TMs and reactors R&D is to achieve meaningful long-term stability at the highest CO₂ flux possible. From an application perspective, long-term flux stability is more important than the magnitude of flux. So far, the longest stability testing demonstrated at a laboratory scale is roughly 1000 hours. The reason for poor stability is multiple, but the loss of MC caused by the poor wettability between the solid matrix and MC, and solid matrix sintering is deemed the primary reason leading to discontinuity of MC phase and increase in the leakage, ultimately decay in CO2 flux. The secondary reason is the chemical reactions between gas sealants (Ag, ceramic bond, glass, etc.) and MC. The reliability of sealing materials needs to be carefully considered when designing large-cell stacks and reactors assembly for practical use. Lessons learned from the mature molten carbonate fuel cells technology about the cell/stack/reactor design should be leveraged.

To achieve the durability suitable for scale-up demonstrations, the following areas need to be further advanced.

5.2. Membrane materials

CO₂TMs are constructed with a solid porous matrix filled with a liquid MC phase. For solid porous matrix in MOCC membranes, doped ceria oxides (SDC, GDC etc.) are identified as the best materials due to their high oxide-ion conductivity and good wettability with MC. However, their chemical reaction with H₂S and SO₂ impurities in flue gas or WGS gas hinders their practical appli-

cations. Therefore, finding new solid matrix materials with good oxide-ion conductivity and chemical stability in sulfur-containing environments are highly desirable for MOCC membranes development

For MECC membranes, Ag-based matrix has been previously studied. The sintering issue of Ag at high temperatures hinders its large-scale applications. Surface modifications and microstructural optimization are still insufficient to improve its stability to the level of practical applications, not to mention the high cost of Ag. Therefore, more studies are needed to understand the composition-flux-stability relationship in new low-cost and highflux NiO-based MECC membrane materials. The drawback of the NiO-MC membrane is its poor stability in reducing atmospheres. While adding SDC into NiO-MC membranes can improve the stability and enable trip-conduction, the presence of SDC phase reduces NiO volume, thus resulting in lowered electronic conductivity. Optimization of phase volume among SDC, NiO and MC is needed for scale up demonstration. Alternatively, introducing electronic conduction in SDC phase while maintaining good chemical stability and wettability with MC will mitigate the requirement for more NiO volume to provide enough electronic conduction.

A fundamental problem associated with MC-based CO_2TMs is the thermal stability of molten carbonates at high temperatures. Thermodynamic calculations indicate that Li-Na-K carbonate system, regardless binary or ternary, would decompose into oxide by giving off CO_2 in CO_2 -lean environments. Therefore, the upper temperature limit at which molten carbonates can be stably used needs further experimental verifications.

5.3. Microstructure/surface treatment

Pore size, pore distribution, porosity and tortuosity of the solid matrix have a significant impact on the performance (flux and stability) of CO₂TMs. First, they determine the magnitude of capillary forces to withhold the MC phase. The finer and more uniform the pores the higher the capillary forces and the higher pressuredifferential under which the MC phase can withstand; the latter is vitally important to achieve long-term flux stability for pressurized operations such as CO2 removal from a pressurized WGS stream. On the other hand, since the ratio of porosity to tortuosity (ε/τ) is directly related to the effective conductivity of CO₂TMs, its magnitude also governs CO₂ flux in a bulk-diffusion controlled transport. New synthesis methods are still being sought to fabricate low-cost, homogenously porous solid matrix with tortuous, small, and uniformly distributed pores. On the other hand, modifying the surface of CO₂TMs that can improve CO₂ exchange kinetics as well as wettability between solid and MC phase remains an unexplored area.

5.4. CO₂ capture and conversion

One distinct feature of CO_2TMs from other CO_2 capture and conversion methods is the coupling of CO_2 capture with conversion in a single membrane reactor at high temperatures. Up to now, all CO_2TMs reactors, *i.e.* coupling with DMR, ODHE and WGS, are demonstrated at laboratory scale. Demonstrating flux and stability performance at bench-top and pilot scales are the vital tasks to advance electrochemical CO_2TM systems toward commercialization.

Another area worth further study is the application of catalysts directly to the membrane surface, instead of in a separate bed inside the reactor, to better promote CO_2 conversion. However, how to effectively load solid catalysts onto molten carbonate surface has not been explored yet. Supported thin-film membranes may offer a solution to this problem as the catalyst can be decorated to the surface of the thick solid porous support that is free of MC.

5.5. Flux equation for triple-conducting membranes

The flux of a mixed conducting transport in $\rm CO_2TMs$ is influenced by both surface reaction mechanisms and bulk properties/microstructures. The latter is particularly important for multiphase transport because the volumetric fraction of each phase and tortuosity could significantly affect the flux. While the mechanisms of surface $\rm CO_2$ ionization at gas-liquid and gas-solid interfaces in MOCCs and MECCs seem to be straightforward, the triple conduction ($\rm CO_3^{2-}/O^{2-}/e^{-}$) in multiphase membranes would require a new set of flux formalisms deriving from the generic Eq. (1) to describe the transport flux. Equally important is to model the coupling of capture and conversion of $\rm CO_2$ by combining the flux equation with the rate kinetics of catalytic reactions and boundary conditions in membrane reactors.

5.6. Physics-based modeling and system analysis

The early discussion in section 2.2 on CO₂ flux as well as the early work on CO2 transport modeling follows closely the traditional phenomenological transport theory, which is largely limited to one-dimension and ignores mechanistic details on bulk transport and surface reaction. With a physics-based approach, the bulk transport and surface reactions through CO₂TM can be modeled with rich physiochemical details in high dimensionality and better accuracy. Unfortunately, such physics-based multidimensional models have so far not been demonstrated in CO₂TMs and the associated catalytic reactors. Instead, several system-level models have been published to demonstrate the advantages of CO₂TM reactors in energy efficiency and cost over conventional technologies. For example, Fang et al. [169] performed a lifecycle techno-economic analysis of a CO₂TM reactor system consisting of a MECC membrane and solid oxide electrolysis cell (SOEC) for combined CO₂ capture and conversion to syngas and to liquid synthetic fuel, and compared its techno-economic performance with renewable-based syngas-to-liquid technologies. Fig. 22 shows the process flow diagram. The analysis shows a parasitic energy of 321 kJ/kg CO₂ is required in MECC plant for CO₂ capture, which is half of that consumed by a typical amine washing plant. It also shows that an increase in SOEC surface area results in a decreased parasitic energy while not significantly affecting the system efficiency. The analysis further shows that the price of synthetic fuels produced from MECC-SOEC system is competitive with that of biomass-to-liquid (BTL) fuel at an electricity price of \$ 0.096/kwh.

Sherman et al. simulated a post-combustion CO_2 capture process with a MECC membrane [40]. The flue gas is assumed to contain 13% CO_2 , 16% H_2O , 3% O_2 and 68% N_2 and delivered to the CO_2 capture system at 150 °C and 1 atm. A syngas is used as the sweep gas to consume the permeated O_2 and enhancing the driving force of CO_2 transport. The produced stream from the MECC membrane sweep side containing of CO_2 , steam and heat. The CO_2 is compressed for storage. The heat and steam are suggested to preheat unit feed streams and to make steam for electricity generation. Fig. 23 shows the process flow diagram.

The process is capable to capture at least 90% of the CO_2 generated by the power plant. With recovery of excess process heat for electricity production, the CO_2 capture process after add-on to an existing power plant has an energy penalty of about 12%, which is less than DOE's expectation (a parasitic energy load no greater than 20%). This energy penalty is better than other advanced post-combustion CO_2 capture processes, such as polymer membrane-based CO_2 capture (16% energy penalty) [170] and amine-based absorption systems (26-41% energy penalty) [171]. However, the cost of additional capture system exceeds the DOE's cost target (\$210/ton CO_2 capture vs. \$42/ton CO_2 capture).

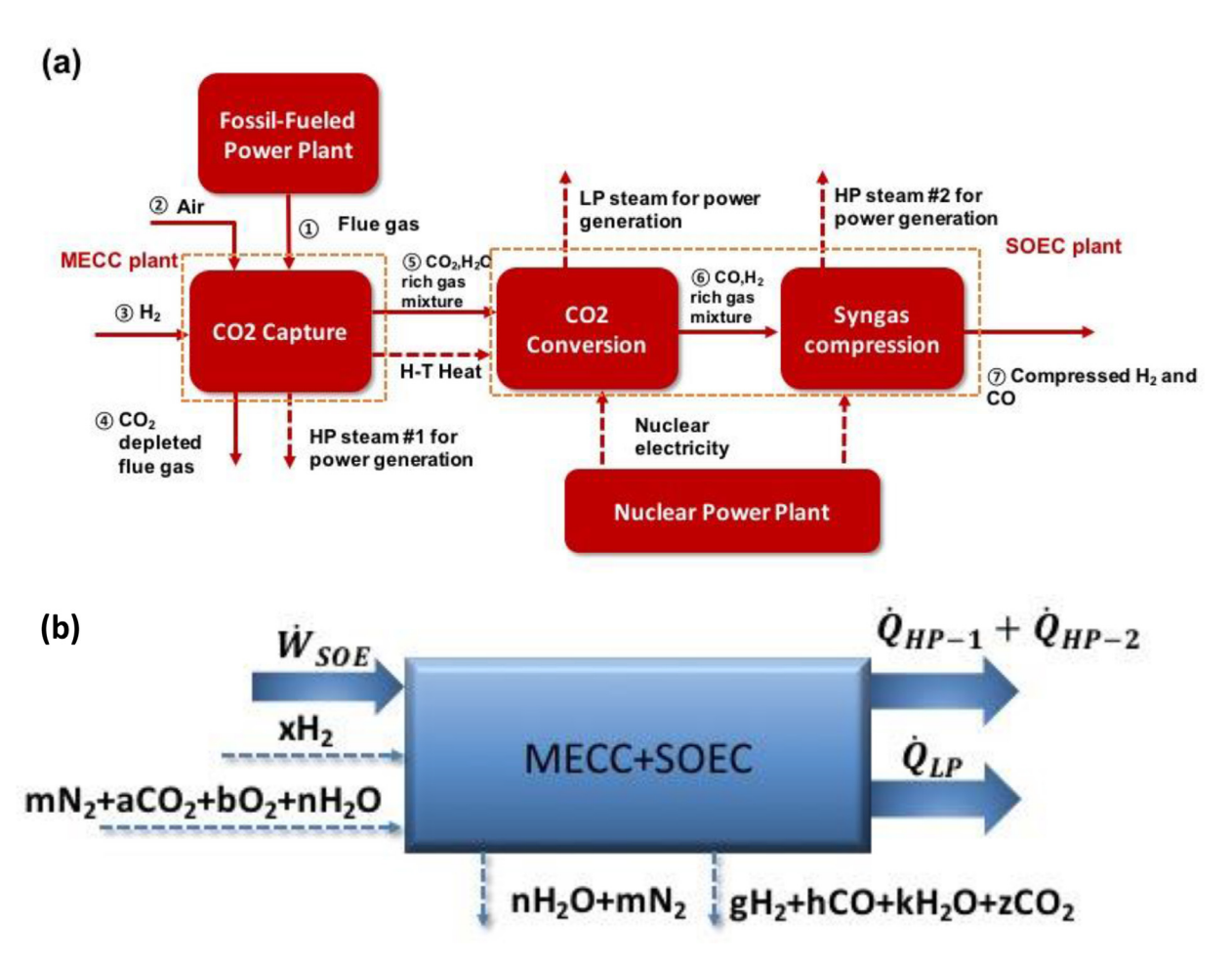


Fig. 22. (a) Process block diagram and (b) mass and energy flow diagram of a combined MECC-SOEC system. Reproduced from ref. [169] with permission from Elsevier, 2018.

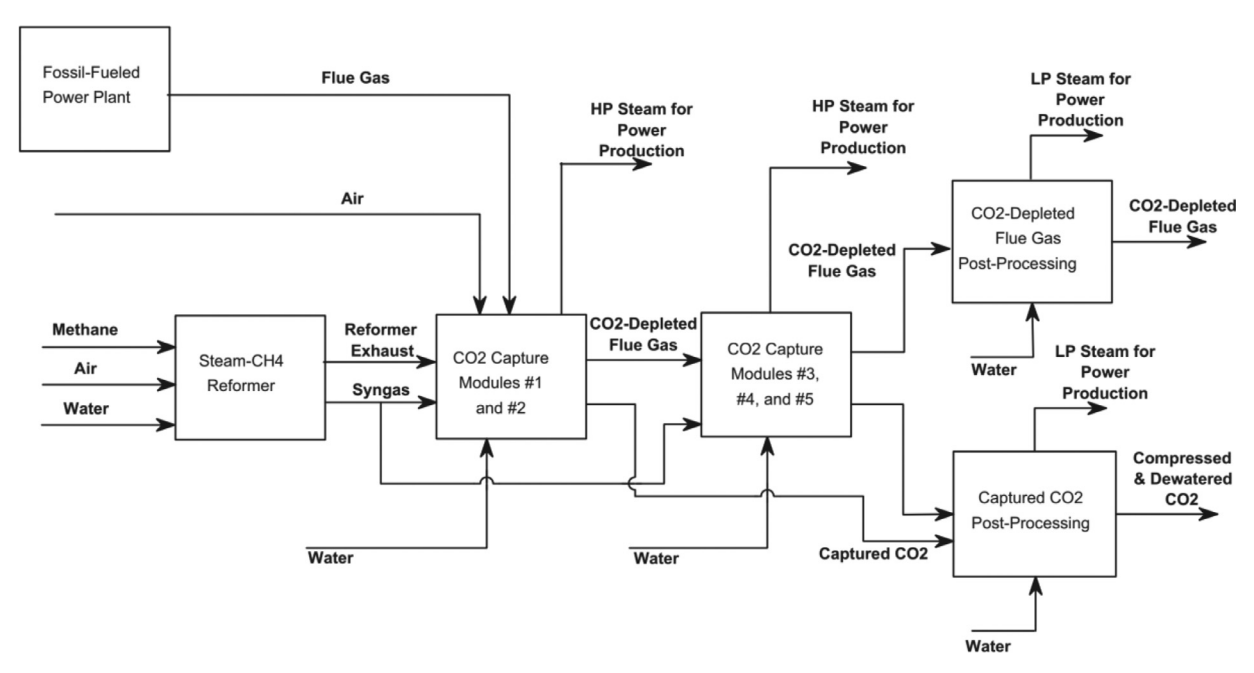


Fig. 23. Block flow diagram of syngas combustion-assisted combined power plant/CO₂ capture facility. Reproduced from ref. [40] with permission from Elsevier, 2012.

6. Conclusions

This comprehensive review summarizes recent progress in high-temperature electrochemical CO₂ transport membranes (CO₂TMs) for direct and combined CO₂ capture and conversion. From materials to mechanisms and performance to problems, this review covers a broad aspect of three types of newly emerged CO₂TMs and their associated reactors based on mixed conducting electrochemistry. The three mixed conducting CO₂TMs are: metal-carbonate, ceramic-carbonate and ceramic-ceramic-carbonate multi-phase composites, conducting electron/carbonate-ion, oxide-ion/carbonate-ion and oxide-ion/electron/carbonate-ion, respectively.

For the MC phase, if membranes are intended to operate at a low temperature range, such as 400-500 °C, the ternary eutectic carbonate system ((Li-Na-K)2CO3) is the best choice for its low eutectic point. However, at a high temperature range (550-900 °C), (Li-Na)₂CO₃ binary carbonate is a better choice due to its higher carbonate-ion conductivity. For matrix materials used in MOCC membranes, doped ceria oxides (SDC, GDC etc.) are the best solid oxide-ion conducting materials. However, their chemical reaction with H2S and SO2 impurities in flue gas hinders their practical applications. For MECC membranes, Ag is a good option for the electron-conducting phase in terms of conductivity and compatibility with MC. However, its sintering problem needs to be addressed before practical demonstrations. A recent noticeable development towards low-cost, high-flux and stable MECC is to use NiO as the solid matrix. The in-situ formed conductive Li_{0.4}Ni_{1.6}O₂ phase can serve as the electron-conducting phase. The sintering and high-cost issues of Ag-based MECCs are subsequently solved.

In many cases, microstructure, surface modification and operating conditions are reviewed in detail with respect to permeation flux and stability. All relevant materials (both MC and solid matrix), membrane thickness, operating temperature, feed and sweep gas compositions, and CO2 flux and stability are summarized in Tables 3-5 for easy reference. Finally, designs and performances of several types of CO₂TM-based CO₂ capture and conversion reactors are provided. As an example, with CH4 as the sweep gas, the captured CO2 can instantly react with CH4 to produce syngas through DMR reaction. For MECC- and MEOCC-based membrane reactors, the co-transported O2 can reduce coking, an intrinsic problem for DMR process. The CO₂TM reactors can also convert ethane into ethylene via oxidative dehydrogenation of ethane (ODHE) route using the captured CO₂ as a soft oxidizer. By combining with WGS process, MOCC membranes can promote the production of highpressure H₂ while separating CO₂ in single step without the need of any catalysts due to the high operating temperature.

Finally, the proof-of-concept of electrochemical CO₂ capture and conversion membranes has been successfully demonstrated at laboratory scale. A further demonstration of this new technology to bench-top, pilot and ultimately commercial levels and its competitiveness to the incumbent benchmark sorption-based technologies would require systematic advancements in materials, reactor design and lifecycle analysis/system modeling in the near future.

Declaration of Competing Interest

The authors declare no conflicts of interest.

Acknowledgements

P. Zhang, X. Zhu and W. Yang appreciate the financial support from National Natural Science Foundation of China (21905270), Dalian National Laboratory for Clean Energy (DNL180203) and the Strategic Priority Research Program of the Chinese Academy of Sciences (CAS) (XDB17000000). K. Huang would like to thank Na-

tional Science Foundation for supporting this research through awards CBET-1247064, -1340269, -1401280, -1924095 and National Energy Technology Laboratory, Department of Energy, through award DE-FE-0031634.

References

- Cox PM, Betts RA, Jones DD, Spall SA, Totterdell IJ. Acceleration of global warming due to carbon-cycle feedbacks in a coupled climate model. *Nature* 2000:408:184-7
- [2] Rochelle GT. Amine scrubbing for CO₂ capture. Science 2009;325:1652-4.
- [3] Sanz-Perez ES, Murdock CR, Didas SA, Jones CW. Direct capture of CO₂ from ambient air. Chem. Rev. 2016;116:11840–76.
- [4] Boot-Handford ME, Abanades JC, Anthony EJ, Blunt MJ, Brandani S, Mac Dowell N, Fernández JR, Ferrari M-C, Gross R, Hallett JP, Haszeldine RS, Heptonstall P, Lyngfelt A, Makuch Z, Mangano E, Porter RTJ, Pourkashanian M, Rochelle GT, Shah N, Yao JG, Fennell PS. Carbon capture and storage update. Energy Environ. Sci. 2014;7:130–89.
- [5] Agarwal AS, Zhai Y, Hill D, Sridhar N. The electrochemical reduction of carbon dioxide to formate/formic acid: engineering and economic feasibility. *Chem-SusChem* 2011;4:1301–10.
- [6] Ganesh I. Conversion of carbon dioxide into methanol a potential liquid fuel: Fundamental challenges and opportunities (a review). Renew. Sustainable Energy Rev. 2014;31:221–57.
- [7] Pan H, Hu Y-S, Chen L. Room-temperature stationary sodium-ion batteries for large-scale electric energy storage. *Energy Environ. Sci.* 2013:6.
- [8] Gu X, Lai C. One dimensional nanostructures contribute better Li-S and Li-Se batteries: Progress, challenges and perspectives. *Energy Storage Mater* 2019:23:190-224.
- [9] Qi S, Xu B, Tiong VT, Hu J, Ma J. Progress on iron oxides and chalcogenides as anodes for sodium-ion batteries. Chem. Eng. J. 2020;379:122261.
- [10] Manthiram A, Fu Y, Chung SH, Zu C, Su YS. Rechargeable lithium-sulfur batteries. Chem. Rev. 2014;114:11751–87.
- [11] Dubois A, Ricote S, Braun RJ. Benchmarking the expected stack manufacturing cost of next generation, intermediate-temperature protonic ceramic fuel cells with solid oxide fuel cell technology. J. Power Sources 2017;369:65-77.
- [12] Xia C, Cai Y, Wang B, Afzal M, Zhang W, Soltaninazarlou A, Zhu B. Strategy towards cost-effective low-temperature solid oxide fuel cells: A mixed-conductive membrane comprised of natural minerals and perovskite oxide. J. Power Sources 2017;342:779–86.
- [13] Rangel-Hernandez VH, Torres C, Zaleta-Aguilar A, Gomez-Martinez MA. The exergy costs of electrical power, cooling, and waste heat from a hybrid system based on a solid oxide fuel cell and an absorption refrigeration system. *Energies* 2019;12:3476.
- [14] Yan L, Cao Y, He B. Energy, exergy and economic analyses of a novel biomass fueled power plant with carbon capture and sequestration. Sci. Total. Environ. 2019;690:812–20.
- [15] Zakaria Z, Abu Hassan SH, Shaari N, Yahaya AZ, Boon Kar Y. A review on recent status and challenges of yttria stabilized zirconia modification to lowering the temperature of solid oxide fuel cells operation. *Int. J. Energy Res.* 2019;44:631–50
- [16] LeVailey TL, Richard AR, Fan M. The progress in water gas shift and steam reforming hydrogen production technologies A review. Int. J. Hydrogen Energy 2014;39:16983–7000.
- [17] Wei Z, Sun J, Li Y, Datye AK, Wang Y. Bimetallic catalysts for hydrogen generation. Chem. Soc. Rev. 2012;41:7994–8008.
- [18] ESRL. Trends in Atmospheric Carbon Dioxide; https://www.esrl.noaa.gov/gmd/ccgg/trends/, 2019.
- [19] OTT JFM. CO₂ capture and storage: are we ready? Energy Environ. Sci 2009;2:449–58.
- [20] Samanta A, Zhao A, Shimizu GKH, Sarkar P, Gupta R. Post-combustion CO₂ capture using solid sorbents: a review. Ind. Eng. Chem. Res. 2012;51:1438-63.
- [21] Wang Q, Luo J, Zhong Z, Borgna A. CO₂ capture by solid adsorbents and their applications: current status and new trends. *Energy Environ. Sci.* 2011;4:42–55.
- [22] Rao AB, Rubin ES. A technical, economic, and environmental assessment of amine-based CO₂ capture technology for power plant greenhouse gas control. Environ. Sci. Technol. 2002;36:4467–75.
- [23] Bates ED, Mayton RD, Ntai I, James H, Davis J. CO₂ Capture by a Task-Specific Ionic Liquid. J. Am. Chem. Soc. 2002;124:926–7.
- [24] Xu X, Song C, Andresen JM, Miller BG, Scaroni AW. Novel polyethylenimine—modified mesoporous molecular sieve of MCM-41 type as high-capacity adsorbent for CO₂ capture. *Energy Fuel* 2002;16:1463-9.
- [25] Furukawa H, Ko N, Go YB, Aratani N, Choi SB, Choi E, AÖ Yazaydin, Snurr RQ, O'Keeffe M, Kim J, Yaghi OM. Ultrahigh porosity in metal-organic frameworks. Science 2010;329:424–8.
- [26] Long JR, Yaghi OM. The pervasive chemistry of metal-organic frameworks. Chem. Soc. Rev. 2009;38:1213–14.
- [27] Reich L, Yue L, Bader R, Lipiński W. Towards solar thermochemical carbon dioxide capture via calcium oxide looping: A review. Aerosol Air Qual. Res. 2014;14:500-14.
- [28] Bader R, Lipiński W. Solar thermal processing. In: Blanco MJ, Santigosa LR, editors. Advances in concentrating solar thermal research and technology. Woodhead Publishing Series in Energy; 2017. p. 403-5.

- [29] Li S, Kreider PB, Wheeler VM, Lipiński W. Thermodynamic Analyses of Fuel Production Via Solar-Driven Ceria-Based Nonstoichiometric Redox Cycling: A Case Study of the Isothermal Membrane Reactor System. J. Sol. Energy Eng. 2019;141:021012.
- [30] Aaron D, Tsouris C. Separation of CO₂ from flue gas: A review. Sep. Sci. Technol. 2005;40:321–48.
- [31] Ramasubramanian K, Verweij H, Winston Ho WS. Membrane processes for carbon capture from coal-fired power plant flue gas: A modeling and cost study. *J. Membr. Sci.* 2012;**421-422**:299–310.
- [32] Belaissaoui B, Le Moullec Y, Willson D, Favre E. Hybrid membrane cryogenic process for post-combustion CO₂ capture. J. Membr. Sci. 2012;415-416:424-34.
- [33] Mannan HA, Mukhtar H, Murugesan T, Nasir R, Mohshim DF, Mushtaq A. Recent applications of polymer blends in gas separation membranes. *Chem. Eng. Technol.* 2013;36:1838-46.
- [34] Liu J, Hou X, Park HB, Lin H. High-performance polymers for membrane CO_2/N_2 separation. *Chem. Eur. J.* 2016;**22**:15980–90.
- [35] Norahim N, Yaisanga P, Faungnawakij K, Charinpanitkul T, Klaysom C. Recent membrane developments for CO₂ separation and capture. *Chem. Eng. Technol.* 2018:41:211–23.
- [36] Yong WF, Chung T-S, Weber M, Maletzko C. New polyethersulfone (PESU) holow fiber membranes for CO₂ capture. *J. Membr. Sci.* 2018;**552**:305–14.
- [37] Wong KK, Jawad ZA. A review and future prospect of polymer blend mixed matrix membrane for CO₂ separation. J. Polym. Res. 2019;26:289.
- [38] Kenarsari SD, Yang D, Jiang G, Zhang S, Wang J, Russell AG, Wei Q, Fan M. Review of recent advances in carbon dioxide separation and capture. RSC Adv 2013;3:22739-73.
- [39] Pera-Titus M. Porous inorganic membranes for CO₂ capture: Present and prospects. *Chem. Rev.* 2014;114:1413–92.
- [40] Sherman SR, Gray JR, Brinkman KS, Huang K. Combustion-assisted CO₂ capture using MECC membranes. *J. Membr. Sci.* 2012;**401-402**:323–32.
- [41] Anantharaman R, Peters T, Xing W, Fontaine M-L, Bredesen R. Dual phase high-temperature membranes for CO₂ separation–performance assessment in post- and pre-combustion processes. Faraday Discuss 2016;192:251–69.
- [42] Fang J. Development of advanced mixed electronic and carbonate ion conducting membranes and reactors for combined CO₂ capture and conversion. University of South Carolina; 2018.
- [43] Daza CE, Gallego J, Moreno JA, Mondragón F, Moreno S, Molina R. CO₂ reforming of methane over Ni/Mg/Al/Ce mixed oxides. Catal. Today 2008:133-135:357-66.
- [44] Fan M-S, Abdullah AZ, Bhatia S. Catalytic technology for carbon dioxide reforming of methane to synthesis gas. ChemCatChem 2009;1:192–208.
- [45] Usman M, Wan Daud WMA, Abbas HF. Dry reforming of methane: Influence of process parameters—A review. Renew. Sustainable Energy Rev. 2015;45:710–44.
- [46] Yang Y, Zhai R, Duan L, Masoud K, Kumar P, John O. Integration and evaluation of a power plant with a CaO-based CO₂ capture system. Int. J. Greenh. Gas Con. 2010;4:603–12.
- [47] Rodriguez N, Alonso M, Grasa G, Carlos Abanades J. Heat requirements in a calciner of CaCO₃ integrated in a CO₂ capture system using CaO. Chem. Eng. J. 2008;138:148–54.
- [48] Mutch GA, Qu L, Triantafyllou G, Xing W, Fontaine M-L, Metcalfe IS. Supported molten-salt membranes for carbon dioxide permeation. J. Mater. Chem. A 2019:7:12951-73.
- [49] Zhang L, Xu N, Li X, Wang S, Huang K, Harris WH, Chiu WKS. High CO₂ permeation flux enabled by highly interconnected three-dimensional ionic channels in selective CO₂ separation membranes. *Energy Environ. Sci.* 2012;5:8310–17.
- [50] Xu N, Li X, Franks MA, Zhao H, Huang K. Silver-molten carbonate composite as a new high-flux membrane for electrochemical separation of CO₂ from flue gas. J. Membr. Sci. 2012;401-402:190-4.
- [51] Zhang P, Tong J, Jee Y, Huang K. Stabilizing a high-temperature electrochemical silver-carbonate CO₂ capture membrane by atomic layer deposition of a ZrO₂ overcoat. Chem. Commun. 2016;52:9817–20.
- [52] Fang J, Xu N, Yang T, Zhang P, Tong J, Huang K. CO₂ capture performance of silver-carbonate membrane with electrochemically dealloyed porous silver matrix. J. Membr. Sci. 2017;523:439–45.
- [53] Anderson M, Lin YS. Carbonate-ceramic dual-phase membrane for carbon dioxide separation. *J. Membr. Sci.* 2010;**357**:122–9.
- [54] Lan R, Abdallah SMM, Amar IA, Tao S. Preparation of dense La_{0.5}Sr_{0.5}Fe_{0.8}Cu_{0.2}O₃₋₈-(Li,Na)₂CO₃-LiAlO₂ composite membrane for CO₂ separation. *J. Membr. Sci.* 2014;**468**:380-8.
- [55] Zhang P, Tong J, Huang K. Self-Formed, Mixed-Conducting, Triple-phase membrane for efficient CO₂/O₂ capture from flue gas and in situ dry-oxy methane reforming. ACS Sustainable Chem. Eng. 2018;6:14162–9.
- [56] Ovalle-Encinia O, Pfeiffer H, Ortiz-Landeros J. Ce_{0.85}Sm_{0.15}O₂-Sm_{0.6}Sr_{0.4}Al_{0.3}Fe_{0.7}O₃ composite for the preparation of dense ceramic-carbonate membranes for CO₂ separation. *J. Membr. Sci.* 2018;547:11–18.
- [57] Fabián-Anguiano JA, Mendoza-Serrato CG, Gómez-Yáñez C, Zeifert B, Ma X, Ortiz-Landeros J. Simultaneous CO₂ and O₂ separation coupled to oxy-dry reforming of CH₄ by means of a ceramic-carbonate membrane reactor for in situ syngas production. *Chem. Eng. Sci.* 2019;210:115250.
- [58] Corradini D, Coudert FX, Vuilleumier R. Carbon dioxide transport in molten calcium carbonate occurs through an oxo-Grotthuss mechanism via a pyrocarbonate anion. *Nat. Chem.* 2016;8:454–60.

- [59] Zhang L, Huang X, Qin C, Brinkman K, Gong Y, Wang S, Huang K. First spectroscopic identification of pyrocarbonate for high CO₂ flux membranes containing highly interconnected three dimensional ionic channels. *Phys. Chem. Chem. Phys.* 2013;15:13147–52.
- [60] Zhang L, Tong J, Gong Y, Han M, Wang S, Huang K. Fast electrochemical CO₂ transport through a dense metal-carbonate membrane: A new mechanistic insight. J. Membr. Sci. 2014;468:373–9.
- [61] Tong J, Zhang L, Han M, Huang K. Electrochemical separation of CO₂ from a simulated flue gas with high-temperature ceramic–carbonate membrane: New observations. *J. Membr. Sci.* 2015;**477**:1–6.
- [62] Norton TT, Ortiz-Landeros J, Lin YS. Stability of La-Sr-Co-Fe oxide-carbonate dual-phase membranes for carbon dioxide separation at high temperatures. *Ind. Eng. Chem. Res.* 2014;53:2432-40.
- [63] Rui Z, Anderson M, Li Y, Lin YS. Ionic conducting ceramic and carbonate dual phase membranes for carbon dioxide separation. J. Membr. Sci. 2012;417-418:174-82.
- [64] Norton TT, Lin YS. Ceramic–carbonate dual-phase membrane with improved chemical stability for carbon dioxide separation at high temperature. *Solid State Ionics* 2014;**263**:172–9.
- [65] Norton TT, Lu B, Lin YS. Carbon dioxide permeation properties and stability of samarium-doped-ceria carbonate dual-phase membranes. J. Membr. Sci. 2014;467:244–52.
- [66] Lu B, Lin YS. Asymmetric thin samarium doped cerium oxide-carbonate dual-phase membrane for carbon dioxide separation. *Ind. Eng. Chem. Res.* 2014:53:13459-66.
- [67] Dong X, Wu H-C, Lin YS. CO₂ permeation through asymmetric thin tubular ceramic-carbonate dual-phase membranes. *J. Membr. Sci.* 2018;564:73–81.
- [68] Chung SJ, Park JH, Li D, Ida J-I, Kumakiri I, Lin JYS. Dual-phase metal-car-bonate membrane for high-temperature carbon dioxide separation. *Ind. Eng. Chem. Res.* 2005;44:7999–8006.
- [69] Zhang L, Gong Y, Brinkman KS, Wei T, Wang S, Huang K. Flux of silver-carbonate membranes for post-combustion CO₂ capture: The effects of membrane thickness, gas concentration and time. J. Membr. Sci. 2014;455:162–7.
- [70] Rui Z, Anderson M, Lin YS, Li Y. Modeling and analysis of carbon dioxide permeation through ceramic-carbonate dual-phase membranes. J. Membr. Sci. 2009;345:110–18.
- [71] Zhuang S, Li Y, Zuo M, Tan X, Meng B, Yang N, Liu S. Dense composite electrolyte hollow fibre membranes for high temperature CO₂ separation. Sep. Purif. Technol. 2014;132:712–18.
- [72] Bouwmeester HJM, Kruidhof H, Burggraaf AJ. Importance of the surface exchange kinetics as rate limiting step in oxygen permeation through mixed-conducting oxides. Solid State Ionics 1994;72:185–94.
- [73] Lin Y, Wang W, Han J. Oxygen permeation through thin mixed conducting solid oxide membranes. *AIChE J* 1994;**40**:786–98.
- [74] Lee TH, Yang YL, Jacobson AJ, Abeles B, Milner S. Oxygen permeation in SrCo_{0.8}Fe_{0.2}O_{3-δ} membranes with porous electrodes. *Solid State Ionics* 1997;100:87-94.
- [75] Zhu X, Liu H, Cong Y, Yang W. Permeation model and experimental investigation of mixed conducting membranes. AIChE J 2012;58:1744–54.
- [76] Zhu Y, Li W, Liu Y, Zhu X, Yang W. Selection of oxygen permeation models for different mixed ionic-electronic conducting membranes. AIChE J 2017;63:4043–53.
- [77] Zhu X, Yang W. Microstructural and interfacial designs of oxygen-permeable membranes for oxygen separation and reaction-separation coupling. Adv. Mater. 2019:1902547.
- [78] Lu B, Lin YS. Synthesis and characterization of thin ceramic-carbonate dual-phase membranes for carbon dioxide separation. J. Membr. Sci. 2013;444:402–11.
- [79] Jiang X, Zhu J, Liu Z, Guo S, Jin W. CO₂-tolerant SrFe_{0.8}Nb_{0.2}O_{3-δ}-carbonate dual-phase multichannel hollow fiber membrane for CO₂ capture. *Ind. Eng. Chem. Res.* 2016;55:3300-7.
- [80] Tong J, Lei X, Fang J, Han M, Huang K. Remarkable O₂ permeation through a mixed conducting carbon capture membrane functionalized by atomic layer deposition. J. Mater. Chem. A 2016;4:1828–37.
- [81] Patrício SG, Papaioannou E, Zhang G, Metcalfe IS, Marques FMB. High performance composite CO₂ separation membranes. J. Membr. Sci. 2014;471:211–18.
- [82] Kojim T, Miyazaki Y, Nomura K, Tanimoto K. Electrical conductivity of molten Li₂CO₃-X₂CO₃ (X: Na, K, Rb, and Cs) and Na₂CO₃-Z₂CO₃ (Z: K, Rb, and Cs). J. Electrochem. Soc. 2007;154:F222-FF30.
- [83] Ward AT, Janz GJ. Molten carbonate electrolytes: electrical conductance, density and surface tension of binary and ternary mixtures. *Electrochim. Acta* 1965;**10**:849–57.
- [84] Janz GJ, Lorenz MR. Molten carbonate electrolytes: physical properties, structure, and mechanism of electrical conductance. J. Electrochem. Soc. 1961;108:1052–8.
- [85] Kojima T, Miyazaki Y, Nomura K, Tanimoto K. Density, surface tension, and electrical conductivity of ternary molten carbonate system Li₂CO₃-Na₂CO₃-K₂CO₃ and methods for their estimation. J. Electrochem. Soc. 2008;155:F150-6.
- [86] Lair V, Albin V, Ringuedé A, Cassir M. Theoretical predictions vs. experimental measurements of the electrical conductivity of molten Li₂CO₃-K₂CO₃ modified by additives. Int. I. Hydrogen Energy 2012;37:19357-64.
- [87] Zhang L, Li X, Wang S, Romito KG, Huang K. High conductivity mixed oxide-ion and carboante-ion conductors supported by a prefabricated porous solid-oxide matrix. Electrochem. Commun. 2011;13:554-7.

- [88] Li X, Xiao G, Huang K. Effective ionic conductivity of a novel intermediate-temperature mixed oxide-ion and carbonate-ion conductor. J. Electrochem. Soc. 2011;158:B225–32.
- [89] Wade JL, Lee C, West AC, Lackner KS. Composite electrolyte membranes for high temperature CO₂ separation. J. Membr. Sci. 2011;369:20–9.
- [90] Ahn H, Kim D, Melgar VMA, Kim J, Othman MR, Nguyen HVP, Han J, Yoon SP. YSZ-carbonate dual-phase membranes for high temperature carbon dioxide separation. J. Ind. Eng. Chem. 2014;20:3703–8.
- [91] Tong J, Zhang L, Fang J, Han M, Huang K. Electrochemical capture of CO₂ from natural gas using a high-temperature ceramic-carbonate membrane. J. Electrochem. Soc. 2015;162:E43-6.
- [92] Zhang P, Tong J, Huang K. Combining electrochemical CO₂ capture with catalytic dry methane reforming in a single reactor for low-cost syngas production. ACS Sustainable Chem. Eng. 2016;4:7056–65.
- [93] Yang Z, Zhu Y, Han M. Synthesis and characterization of gadolinium doped ceria-carbonate dual-phase membranes for carbon dioxide separation. J. Alloy. Compd. 2017;723:70–4.
- [94] Xia C, Liu M. Microstructures, conductivities, and electrochemical properties of Ce_{0.9}Gd_{0.1}O₂ and GDC-Ni anodes for low-temperature SOFCs. Solid State Ionics 2002:152-153:423-30.
- [95] Zeng Y, Lin YS. Synthesis and properties of copper and samarium doped yttria-bismuth oxide powders and membranes. J. Mater. Sci. 2001;36:1271-6.
- [96] Gude U, Baumann S, Meulenberg WA, Müller M. Towards the development of materials for chemically stable carbonate-ceramic membranes to be used for CO₂ separation in water-gas-shift reactors. Sep. Purif. Technol. 2019;215:378-83.
- [97] Dong X, Ortiz Landeros J, Lin YS. An asymmetric tubular ceramic-carbonate dual phase membrane for high temperature CO₂ separation. *Chem. Commun.* 2013:49:9654–6.
- [98] Chen T, Wang Z, Das S, Liu L, Li Y, Kawi S, Lin YS. A novel study of sulfur-resistance for CO₂ separation through asymmetric ceramic-carbonate dual-phase membrane at high temperature. J. Membr. Sci. 2019;581:72–81.
- [99] Chen T, Wu H-C, Li Y, Lin YS. Poisoning effect of H₂S on CO₂ permeation of samarium-doped-ceria/carbonate dual-phase membrane. *Ind. Eng. Chem. Res.* 2017:56:14662–9.
- [100] Chen T, Yu B, Zhao Y, Li Y, Lin YS. Carbon dioxide permeation through ceramic-carbonate dual-phase membrane-effects of sulfur dioxide. J. Membr. Sci. 2017;540:477–84.
- [101] Dong X, Lin YS. Catalyst-free ceramic-carbonate dual phase membrane reactor for hydrogen production from gasifier syngas. J. Membr. Sci. 2016;520:907–13.
- [102] Ovalle-Encinia O, Sánchez-Camacho P, González-Varela D, Pfeiffer H. Development of new bifunctional dense ceramic-carbonate bembrane reactors for gas mixtures separation, through CO oxidation and subsequent CO₂ permeation. ACS Appl. Energy Mater. 2019;2:1380-7.
- [103] Xing W, Peters T, Fontaine M-L, Evans A, Henriksen PP, Norby T, Bredesen R. Steam-promoted CO₂ flux in dual-phase CO₂ separation membranes. J. Membr. Sci. 2015;482:115–19.
- [104] Zuo M, Zhuang S, Tan X, Meng B, Yang N, Liu S. Ionic conducting ceramic—carbonate dual phase hollow fibre membranes for high temperature carbon dioxide separation. J. Membr. Sci. 2014;458:58–65.
- [105] Li Y, Rui Z, Xia C, Anderson M, Lin YS. Performance of ionic-conducting ceramic/carbonate composite material as solid oxide fuel cell electrolyte and CO₂ permeation membrane. Catal. Today 2009;148:303–9.
- [106] Zhang P, Tong J, Huang K. A self-forming dual-phase membrane for high-temperature electrochemical CO₂ capture. J. Mater. Chem. A 2017;5:12769–73.
- [107] Zhang L, Gong Y, Yaggie J, Wang S, Romito K, Huang K. Surface modified silver-carbonate mixed conducting membranes for high flux CO₂ separation with enhanced stability. J. Membr. Sci. 2014;453:36–41.
- [108] Tong J, Si F, Zhang L, Fang J, Han M, Huang K. Stabilizing electrochemical carbon capture membrane with Al₂O₃ thin-film overcoating synthesized by chemical vapor deposition. *Chem. Commun.* 2015;51:2936–8.
- [109] Fang J, Tong J, Huang K. A superior mixed electron and carbonate-ion conducting metal-carbonate composite membrane for advanced flue-gas carbon capture. *J. Membr. Sci.* 2016;**505**:225–30.
- [110] Zhang J, Zhang Z, Chen Y, Xu X, Zhou C, Yang G, Zhou W, Shao Z. Materials design for ceramic oxygen permeation membranes: Single perovskite vs. single/double perovskite composite, a case study of tungsten-doped barium strontium cobalt ferrite. J. Membr. Sci. 2018;566:278–87.
- [111] Gao J, Lun Y, Han N, Tan X, Fan C, Liu S. Influence of nitric oxide on the oxygen permeation behavior of La_{0.6}Sr_{0.4}Co_{0.2}Fe_{0.8}O_{3-δ} perovskite membranes. Sep. Purif. Technol. 2019;210:900-6.
- [112] Li T, Kamhangdatepon T, Wang B, Hartley UW, Li K. New bio-inspired design for high-performance and highly robust La_{0.6}Sr_{0.4}Co_{0.2}Fe_{0.8}O_{3.δ} membranes for oxygen permeation. *J. Membr. Sci.* 2019;**578**:203–8.
- [113] Chae JW, Park YK, Magnone E, Park JH. Oxygen permeation properties of Sm/Sr co-doped ceria decorated Ba_{0.5}Sr_{0.5}Co_{0.8}Fe_{0.2}O_{3-δ} hollow fiber membrane. J. Ind. Eng. Chem. 2019;**76**:508–14.
- [114] Liu S, Tan X, Li K, Hughes R. Synthesis of strotium cerates-based perovskite ceramics via water-soluble complex precursor routes. *Ceram. Int.* 2002;**28**:327–35.
- [115] Tan X, Liu N, Meng B, Sunarso J, Zhang K, Liu S. Oxygen permeation behavior of La_{0.6}Sr_{0.4}Co_{0.8}Fe_{0.2}O₃ hollow fibre membranes with highly concentrated CO₂ exposure. J. Membr. Sci. 2012;389:216–22.
- [116] Yang Q. Lin YS, Bülow M. High temperature sorption separation of air for producing oxygen-enriched CO₂ stream. AIChE J 2006;52:574–81.

- [117] Yi J, Feng S, Zuo Y, Liu W, Chen C. Oxygen permeability and stability of $Sr_{0.95}Co_{0.8}Fe_{0.2}O_{3-\delta}$ in a CO_2 and H_2O -containing atmosphere. *Chem. Mater.* 2005:17:5856–61.
- [118] Zhu X, Liu Y, Cong Y, Yang W. Ce_{0.85}Sm_{0.15}O_{1.925}-Sm_{0.6}Sr_{0.4}Al_{0.3}Fe_{0.7}O₃ dual-phase membranes: One-pot synthesis and stability in a CO₂ atmosphere. Solid State Ionics 2013;253:57-63.
- [119] Zhang P, Tong J, Huang K. Dry-oxy methane reforming with mixed e⁻/CO₃²⁻ conducting membranes. ACS Sustainable Chem. Eng. 2017;5:5432-9.
- [120] Zhang P, Tong J, Huang K. Role of CO₂ in catalytic ethane-to-ethylene conversion using a high-temperature CO₂ transport membrane reactor. ACS Sustainable Chem. Eng. 2019;7:6889–97.
- [121] Ortiz-Landeros J, Norton T, Lin YS. Effects of support pore structure on carbon dioxide permeation of ceramic-carbonate dual-phase membranes. Chem. Eng. Sci. 2013;104:891–8.
- [122] Ovalle-Encinia O, Pfeiffer H, Ortiz-Landeros J. CO₂ separation improvement produced on a ceramic-carbonate dense membrane superficially modified with Au-Pd. *Ind. Eng. Chem. Res.* 2018;57:9261-8.
- [123] Zhu X, Yang W. *Mixed conducting ceramic membranes*. Berlin: Springer-Verlag GmbH Germany; 2017.
- [124] Erlebacher J, Aziz MJ, Karma A, Dimitrov N, Sieradzki K. Evolution of nanoporosity in dealloying. Lett. Nat. 2001;410:450-3.
- [125] Lin YS, De Vries KJ, Brinkman HW, Burggraaf AJ. Oxygen semipermeable solid oxide membrane composites prepared by electrochemical vapor deposition. J. Membr. Sci. 1992;66:211–26.
- [126] Chen LJ, Lin CJ, Zuo J, Song LC, Huang CM. First spectroscopic observation of peroxocarbonate/peroxodicarbonate in molten carbonate. J. Phys. Chem. B 2004:108:7553-6.
- [127] Chen T, Wang Z, Hu J, Wai MH, Kawi S, Lin YS. High CO₂ permeability of ceramic-carbonate dual-phase hollow fiber membrane at medium-high temperature. J. Membr. Sci. 2020;597:117770.
- [128] Chen T, Wang Z, Liu L, Pati S, Wai MH, Kawi S. Coupling CO₂ separation with catalytic reverse water-gas shift reaction via ceramic-carbonate dual-phase membrane reactor. Chem. Eng. J. 2020;379:122182.
- [129] Fernandez-Naveira A, Abubackar HN, Veiga MC, Kennes C. Carbon monoxide bioconversion to butanol-ethanol by Clostridium carboxidivorans: kinetics and toxicity of alcohols. Appl. Microbiol. Biotechnol. 2016; 100:4231–40.
- [130] Kim TW, Bae SS, Lee JW, Lee SM, Lee JH, Lee HS, Kang SG. A biological process effective for the conversion of CO-containing industrial waste gas to acetate. *Bioresour. Technol.* 2016;211:792–6.
- [131] Fernández-Naveira Á, Veiga MC, Kennes C. H-B-E (hexanol-butanol-ethanol) fermentation for the production of higher alcohols from syngas/waste gas. *J. Chem. Technol. Biotechnol.* 2017;92:712–31.
- [132] Chakraborty S, Rene ER, Lens PNL, Veiga MC, Kennes C. Enrichment of a solventogenic anaerobic sludge converting carbon monoxide and syngas into acids and alcohols. *Bioresour. Technol.* 2019;272:130–6.
- [133] Millet J, Buvet R. Molten carboante fuel cell with water injection, in: Proceedings of the Hydrocarbon Air Fuel Cells Symposium. Altantic City 1965:242–50.
- [134] Laosiripojana N, Charojrochkul S, Kim-Lohsoontorn P, Assabumrungrat S. Role and advantages of H₂S in catalytic steam reforming over nanoscale CeO₂-based catalysts. *J. Catal.* 2010;**276**:6–15.
- [135] Kaddouri A, Béguin B. Methane steam reforming in the absence and presence of H₂S over Ce_{0.8}Pr_{0.2}O_{2-δ}, Ce_{0.85}Sm_{0.15}O_{2-δ} and Ce_{0.9}Gd_{0.1}O_{2-δ} SOFCs anode materials. Catal. Commun. 2014;46:22-7.
- [136] Vakharia V, Ramasubramanian K, Winston Ho WS. An experimental and modeling study of CO₂-selective membranes for IGCC syngas purification. *J. Membr. Sci.* 2015;488:56–66.
- [137] Baron R, Wejrzanowski T, Ł Szabłowski, Szczęśniak A, Milewski J, Fung K-Z. Dual ionic conductive membrane for molten carbonate fuel cell. Int. J. Hydrogen Energy 2018;43:8100-4.
- [138] Kawase M. Manufacturing method for tubular molten carbonate fuel cells and basic cell performance. *J. Power Sources* 2015;**285**:260–5.
- [139] Morita H, Komoda M, Mugikura Y, Izaki Y, Watanabe T, Masuda Y, Matsuyama T. Performance analysis of molten carbonate fuel cell using a Li/Na electrolyte. J. Power Sources 2002;112:509–18.
- [140] Steele BCH, Heinzel A. Materials for fuel-cell technologies. *Nature* 2001;414:345–52.
- [141] Liu R-S, Zhang L, Sun X, Liu H, Zhang J. Electrochemical technologies for energy storage and conversion. Wiley-VCH; 2012.
- [142] Sulaiman M, Rahman AA, Mohamed NS. Sol-gel synthesis and characterization of Li₂CO₃-Al₂O₃ composite solid electrolytes. *Ionics* 2015;22:327–32.
- [143] Buelens LC, Galvita VV, Poelman H, Detavernier C, Marin GB. Super-dry reforming of methane intensifies CO₂ utilization via Le Chatelier's principle. *Science* 2016;**354**:449–52.
- [144] Li K, Chang X, Pei C, Li X, Chen S, Zhang X, Assabumrungrat S, Zhao Z-J, Zeng L, Gong J. Ordered mesoporous Ni/La₂O₃ catalysts with interfacial synergism towards CO₂ activation in dry reforming of methane. Appl. Catal. B 2019:259.
- [145] Akri M, Zhao S, Li X, Zang K, Lee AF, Isaacs MA, Xi W, Gangarajula Y, Luo J, Ren Y, Cui YT, Li L, Su Y, Pan X, Wen W, Pan Y, Wilson K, Li L, Qiao B, Ishii H, Liao YF, Wang A, Wang X, Zhang T. Atomically dispersed nickel as coke-resistant active sites for methane dry reforming. *Nat. Commun.* 2019;10:5181.
- [146] Olsbye U, Wurzel T, Mleczko L. Kinetic and Reaction Engineering Studies of Dry Reforming of Methane over a Ni/La/Al₂O₃ Catalyst. *Ind. Eng. Chem. Res.* 1997;**36**:5180–8.
- [147] Pakhare D, Spivey J. A review of dry (CO₂) reforming of methane over noble metal catalysts. *Chem. Soc. Rev.* 2014;43:7813–37.

- [148] Rui Z, Ji H, Lin YS. Modeling and analysis of ceramic-carbonate dual-phase membrane reactor for carbon dioxide reforming with methane. Int. J. Hydrogen Energy 2011;36:8292-300.
- [149] Anderson M, Lin YS. Carbon dioxide separation and dry reforming of methane for synthesis of syngas by a dual-phase membrane reactor. AIChE 1 2013;59:2207–18.
- [150] Zhang L, Wang F, Zhu J, Han B, Fan W, Zhao L, Cai W, Li Z, Xu L, Yu H, Shi W. CO₂ reforming with methane reaction over Ni@SiO₂ catalysts coupled by size effect and metal-support interaction. *Fuel* 2019:256.
- [151] Pizzolitto C, Pupulin E, Menegazzo F, Ghedini E, Di Michele A, Mattarelli M, Cruciani G, Signoretto M. Nickel based catalysts for methane dry reforming: Effect of supports on catalytic activity and stability. Int. J. Hydrogen Energy 2019:44:28065-76.
- [152] Gavrilova NN, Sapunov VN, Skudin VV. Intensification of dry reforming of methane on membrane catalyst. Chem. Eng. J. 2019;374:983–91.
- [153] Dou J, Zhang R, Hao X, Bao Z, Wu T, Wang B, Yu F. Sandwiched SiO₂@Ni@ZrO₂ as a coke resistant nanocatalyst for dry reforming of methane. *Appl. Catal. B* 2019;**254**:612–23.
- [154] Torres Galvis HM, de Jong KP. Catalysts for production of lower olefins from synthesis gas: A review. ACS Catal 2013;3:2130–49.
- [155] Zimmermann H, Walzl R. in Ullmann's Encyclopedia of Industrial Chemistry. Weinheim: Wiley-VCH; 2000.
- [156] DeRosa SE, Allen DT. Impact of natural gas and natural gas liquids supplies on the United States chemical manufacturing industry: Production cost effects and identification of bottleneck intermediates. ACS Sustainable Chem. Eng. 2015;3:451–9.
- [157] Wang S, Zhu ZH. Catalytic conversion of alkanes to olefins by carbon dioxide oxidative dehydrogenations: A review. Energy Fuel 2004;18:1126–39.
- [158] Gärtner CA, van Veen AC, Lercher JA. Oxidative dehydrogenation of ethane: Common principles and mechanistic aspects. ChemCatChem 2013;5:3196–217.
- [159] Akin FT, Lin YS. Selective oxidation of ethane to ethylene in a dense tubular membrane reactor. J. Membr. Sci. 2002;209:457-67.
- [160] Wang H, Cong Y, Yang W. Continuous oxygen ion transfer medium as a catalyst for high selective oxidative dehydrogenation of ethane. *Catal. Lett.* 2002;84:101–6.
- [161] Cavani F, Ballarini N, Cericola A. Oxidative dehydrogenation of ethane and propane: How far from commercial implementation? Catal. *Today* 2007;127:113-31.
- [162] Wang S, Murata K, Hayakawa T, Hamakawa S, Suzuki K. Oxidative dehydrogenation of ethane by carbon dioxide over sulfate-modified Cr₂O₃/SiO₂ catalysts. *Catal. Lett.* 1999;**63**:59–64.
- [163] Wang Shaobin, Murata K, Hayakawa T, Hamakawa S, Suzuki K. Dehydrogenation of ethane with carbon dioxide over supported chromium oxide catalysts. Appl. Catal. A 2000;196:1–8.
- [164] Deng S, Li H, Li S, Zhang Y. Activity and characterization of modified Cr₂O₃/ZrO₂ nano-composite catalysts for oxidative dehydrogenation of ethane to ethylene with CO₂. *J. Mol. Catal. A: Chem.* 2007;**268**:169–75.
- [165] Wang H, Cong Y, Yang W. High selectivity of oxidative dehydrogenation of ethane to ethylene in an oxygen permeable membrane reactor. *Chem. Commun.* 2002:1468–9.
- [166] Jiang H, Cao Z, Schirrmeister S, Schiestel T, Caro J. A coupling strategy to produce hydrogen and ethylene in a membrane reactor. *Angew. Chem. Int. Ed.* 2010;49:5656–60.
- [167] Iyoha O, Enick R, Killmeyer R, Howard B, Ciocco M, Morreale B. H₂ production from simulated coal syngas containing H₂S in multi-tubular Pd and 80wt% Pd-20wt% Cu membrane reactors at 1173K. J. Membr. Sci. 2007;306:103-15.
- [168] Wu H-C, Rui Z, Lin JYS. Hydrogen production with carbon dioxide capture by dual-phase ceramic-carbonate membrane reactor via steam reforming of methane. J. Membr. Sci. 2020;598:117780.
- [169] Fang J, Jin X, Xu N, Huang K. Life cycle analysis of a combined CO₂ capture and conversion membrane reactor. J. Membr. Sci. 2018;549:142–50.
- [170] Merkel TC, Lin H, Wei X, Baker R. Power plant post-combustion carbon dioxide capture: an opportunity for membranes. J. Membr. Sci. 2010;359:126–39.
- [171] Lively RP, Chance RR, Koros WJ. Enabling low-cost CO₂ capture via heat integration. Ind. Eng. Chem. Res. 2010;49:7550-62.



Peng Zhang is an associate professor of Dalian Institute of Chemical Physics (DICP), Chinese Academy of Sciences (CAS), China. He received his Ph.D. degree from Hirosaki University, Japan, in 2015, and then worked in University of South Carolina, USA, as a postdoctoral researcher from 2015. His research interests involved mixed conductor membrane, catalytic membrane reactor and solid oxide fuel cells.



Jingjing Tong received her Ph.D degree in China University of Mining and Technology-Beijing in 2015. As a visiting student and scholar, she worked at University of South Carolina and Benedict College from 2015 to 2019. Now she is an assistant professor of Dalian Maritime University, China. She works on CO₂ capture and catalytic membrane reactor.



Kevin Huang is currently a SmartState endowed chair and director of solid oxide fuel cell center at University of South Carolina. He received his Ph.D. in 1992 from University of Science and Technology Beijing and continued his postdoctoral research at the University of Texas at Austin. He joined in the faculty of University of South Carolina after spending ten years as an engineer in Siemens Energy. His current research covers rechargeable batteries, fuel cells, gas separation membranes and multiscale computational modeling. He has published 210+ peerreviewed journal papers, 2 books, 3 book chapters and been granted 15 US patents. He is also the recipient of numerous awards.



Xuefeng Zhu is a professor of Dalian Institute of Chemical Physics (DICP), Chinese Academy of Sciences (CAS), China. He received his Ph.D. degree from DICP, CAS in 2007, and then worked in Arizona Sate University (USA) as a post-doctoral researcher in 2008. His research interests involve mixed conducting ceramic membranes for gas separation, catalytic membrane reactors for process intensification, solid oxide cells, and electrocatalysis for energy conversion and storage.



Weishen Yang is a chair professor of Dalian Institute of Chemical Physics (DICP), Chinese Academy of Sciences (CAS), China. He received his Ph.D. from CAS in 1990. As a visiting scholar, he worked at Birmingham University (UK) in 1989, and the University of Southern California (USA) in 2001. He works on the rational design and molecular-level engineering of functional nanomaterials for applications in catalysis and separation (e.g., inorganic membranes).